Freie Universität Berlin

Potential-energy curves of small molecular dications determined with Auger spectroscopy

Vladimir Sekushin

im Fachbereich Physik
der Freien Universität Berlin
eingereichte Dissertation

December 2012

1. Gutachter: Prof. Dr. Dr. *h.c.* G. Kaindl
2. Gutachter: Prof. Dr. U. Becker

Tag der Einreichung: 21.12.2012
Tag der Disputation: 13.02.2013

Abstract

In the present work high-resolution normal Auger-electron spectra of the NO molecule subsequent to O $1s^{-1}$ and N $1s^{-1}$ photoionizations, the CO_2 molecule subsequent to C $1s^{-1}$ photoionization, and the OCS molecule subsequent to S $2p^{-1}$ photoionization are reported. In addition, corresponding photoelectron spectra were studied. All spectra exhibit vibrational structures indicating stable or metastable electronic states. The main goal of the present study was to derive from the vibrational progressions in the Auger spectra information on the potential-energy curves of metastable dicationic states of the respective molecules. To this end, Franck-Condon analyses of the vibrational progressions were performed assuming Morse potentials along the normal coordinate of each observed vibrational mode.

For the NO molecule, transitions to five metastable dicationic states were observed, with two of them previously unobservable. The present experimental results agree well with calculations of the potential-energy curves of NO^{2+} that allows to assign two hitherto unresolved Auger transitions to N $1s^{-1} \rightarrow C^2\Sigma^+$ and N $1s^{-1} \rightarrow c^4\Pi$. The photoelectron spectra were analyzed by considering not only the interaction of the spin moments of the $1s$ electrons and the 2π electron of the core-ionized states but also a spin-orbit splitting of the ground state $X^2\Pi$ of 15.015 meV; this resulted in more reliable values for the lifetime broadening. In the Auger spectrum of the CO_2 molecule, transitions to seven metastable states were observed. They all show contributions of the symmetric stretching vibrational mode and are assigned on the basis of theoretical results in combination with the assumption that the Auger spectrum is dominated by transitions to singlet states. For the OCS molecule, Auger transitions to eight metastable states were observed and assigned mainly by relating the fit results to calculations. For seven of the observed metastable dicationic states, assuming Morse potentials along the normal coordinates corresponding to the C−O and the C−S stretching vibrational modes, information on the potential-energy surfaces was derived. The photoelectron spectra of the OCS molecule were analyzed by taking into account spin-orbit and molecular-field splittings of the core-ionized state; this allowed to derive for the first time the geometry of the S $2p^{-1}$ core-ionized state.

Kurzfassung

Die vorliegende Arbeit beschäftigt sich mit hochaufgelösten O $1s^{-1}$ und N $1s^{-1}$ Augerspektren von NO, dem C $1s^{-1}$ Augerspektrum von CO_2 sowie dem S $2p^{-1}$ Augerspektrum von OCS. Die dazugehörigen Photoelektronenspektren wurden ebenfalls untersucht. Alle untersuchten Spektren besitzen eine Vibrationsstruktur und zeigen damit, dass die an den Übergängen beteiligten elektronischen Zustände stabil oder metastabil sind. Das Hauptziel der Untersuchungen bestand darin, aus den in den Augerspektren ersichtlichen Vibrationsprogressionen Informationen über die Potenzialflächen der metastabilen dikationischen Zustände abzuleiten. Zu diesem Zweck wurden Franck-Condon-Analysen durchgeführt, wobei entlang der Normalkoordinaten der Moleküle Morsepotenziale angenommen wurden.

Für das Molekül NO wurden Augerübergänge zu fünf metastabilen dikationischen Endzuständen beobachtet, von denen zwei bisher unbekannt waren. Die vorliegenden experimentellen Ergebnisse stimmen gut mit Berechnungen der Potenzialkurven von NO^{2+} überein. Dadurch konnten die beiden erstmalig beobachteten Augerübergänge als N $1s^{-1} \rightarrow C^2\Sigma^+$ und N $1s^{-1} \rightarrow c^4\Pi$ identifiziert werden. Bei der Analyse der Photoelektronenspektren wurde nicht nur die Spin-Spin-Wechselwirkung des $1s$-Elektrons und des 2π-Elektrons im rumpfionisierten Zustand sondern auch die Spin-Bahn-Aufspaltung des Grundzustandes $X^2\Pi$ von 15.015 meV berücksichtig. Durch diese Form der Datenanalyse konnten verlässlichere Werte für die Lebensdauerverbreiterung erzielt werden. In dem Augerspektrum von CO_2 wurden Übergänge zu sieben metastabilen dikationischen Endzuständen beobachtet. Alle Übergänge zeigen die symmetrische Streckschwingungsmode und wurden auf der Basis von Rechnungen sowie der Annahme, dass im Augerspektrum die Übergänge zu den Singulettzuständen dominieren, zugeordnet. Für das Molekül OCS wurden Übergänge zu acht metastabilen Endzuständen beobachtet und hauptsächlich auf der Basis des Fitergebnisses und von Rechnungen zugeordnet. Für sieben der Endzustände konnte unter der Annahme von Morsepotenzialen entlang der Normalkoordinaten der C−O- und der C−S- Streckschwingungsmode Informationen über die Potenzialflächen erzielt werden. Die Photoelektronenspektren des Moleküls OCS wurde unter Berücksichtigung der Spin-Bahn- und der Molekülfeldaufspaltung des Rumpfniveaus analysiert. Hierbei konnte erstmalig die Geometrie des S $2p^{-1}$ rumpfionisierten Zustands bestimmt werden.

Contents

Introduction

When two electrons are removed from the valence shell of a molecule, it normally leads to a considerable weakening of the chemical bonds. The Coulomb repulsion of the nuclei can no longer be compensated for and dissociation of the molecule results. However, in some cases, namely when both electrons are removed from non-bonding orbitals or when the molecule has a multiple-bond structure, the obtained molecular dications are still stable or metastable with respect to dissociation. Such dicationic states possess vibrational levels and are therefore of high experimental and theoretical interest.

Molecular dications play, for example, an important role in interstellar clouds and in the ionosphere of the Earth or of other planets where they are part of a plasma. In the higher atmosphere, neutral molecules can interact with X-rays or with charged particles coming mainly from the Sun and resulting in valence or core ionizations. The dominant decay mechanism of core-ionized molecules is the Auger process leading to the production of doubly ionized molecules that are partly metastable with respect to dissociation [1]. In the ionospheric environment, the doubly ionized molecules can dissociate with formation of products with large enough kinetic energies to escape from the atmosphere into outer space. This escape mechanism of particles from the atmosphere of a planet has been suggested recently in a review work by Thissen *et al.* [2].

With the availability of free-electron lasers such as FLASH at DESY (Hamburg, Germany) or SCSS at Spring-8 (Hyogo, Japan), few-photon multiple ionization of molecules using photons in the extreme ultraviolet energy range became a new research area. Very recently Jiang *et al.* [3, 4], Fukuzawa *et al.* [5], and Yamada *et al.* [6] demonstrated for the molecules D_2, N_2, and O_2 that sequential ionization is the dominating process for multiple ionization of molecules in the extreme ultraviolet region. To understand such sequential ionization processes in detail, it is necessary to know the exact potential-energy curves of the different charge states of the studied molecules. This holds, in particular, for future experiments, where not only the ionic fragments of the sequential ionization process but also the photoelectrons are detected. In this context, studies on molecular dications are an important part of understanding of the sequential ionization process of molecules in detail.

One possible method for obtaining information on the electronic and geometrical structure is to perform experiments directly with the molecular dications.

Such experiments are, however, limited by the very low target densities that can be achieved under laboratory conditions [7]. A second approach that has been widely used in recent years is provided by double ionization with one photon, with both electrons being detected using a coincidence technique that requires a sophisticated experimental setup, namely a time-of-flight photoelectron-photoelectron-coincidence setup as well as an instrument for threshold-photoelectron-coincidence spectroscopy [8, 9]. Since with this technique the long-lived dicationic states are populated directly, the total linewidth is only limited by the experimental resolution, which is of the order of 100 meV. As a result, the energy positions of the vibrational substates can be derived with high accuracy. However, double ionization with one photon can only be explained on the basis of electron correlation, so that the electronic matrix elements of the transitions depend strongly on bond distances. This makes the Franck-Condon approximation inadequate. As a consequence, a simple analysis of vibrational profiles based on the Franck-Condon principle is hardly possible. Nevertheless, this technique allows to derive such spectroscopic quantities as vibrational energies and anharmonicities. A third approach is double-charge-transfer spectroscopy [10, 11]. Spectra obtained using this technique can be well described by Franck-Condon profiles, *i.e.* the adiabatic approximation is valid. In addition, an experimental resolution of better than 150 meV can be obtained; this is sufficient to resolve vibrational structures.

In our approach we utilize the fact that molecular dications can be created by photoionization of a shallow core level with subsequent Auger decay. In this way, high count rates can be obtained with standard electron spectroscopic techniques, and the electronic matrix element varies in most decay processes only insignificantly with the internuclear distance so that it can be considered to be constant. This allows us to perform a Franck-Condon analysis that provides detailed information on the equilibrium geometry of the states involved in the process. Such a Franck-Condon analysis is technically quite simple, however, the successive photoionization and Auger processes lead to a number of complications: due to the change in the equilibrium distance upon photoionization, different vibrational sublevels of the core-ionized state are populated. These different substates represent different initial states for the Auger process, and the corresponding transitions may overlap strongly in the spectrum. In addition, the energy splitting between the different vibrational substates of the core ionized state is of the same order of magnitude as the broadening caused by the lifetime of the created core hole. As a consequence, the excitation and deexcitation pathways are not exactly known, and vibrational lifetime interference has to be taken into account by describing the entire process in a one-step model.

In comparison to the other methods, the Auger spectroscopy has the advantage that spectra that allow a Franck-Condon analysis are experimentally easy to

obtain. The present method has, however, the disadvantage that the resolution is limited by lifetime broadening. Finally, the various methods are based on different processes described by different matrix elements. As a consequence, the relative intensities of transitions to the various dicationic states can be rather different in the spectra of the methods mentioned, *i.e.* not all states are detectable with all methods.

In recent years, it has been shown that vibrationally resolved Auger spectra are very well suited to probe the potential-energy curves of dicationic states by using a Franck-Condon analysis, as performed for spectra of the molecules HBr/DBr [12], HCl/DCl [13], H_2S [14], CO [15], and N_2 [16]. The results of such an analysis represent a critical test for the calculations; see, for example, studies of Matila *et al.* [17], Ellingsen *et al.* [18], and Mondal *et al.* [19].

In contrast to the molecules studied up to now, which are all closed-shell molecules and mainly diatomic, we apply in the present study this analysis to high-resolution Auger spectra of more complicated molecules, namely the open-shell molecule NO (nitric oxide) and the triatomic molecules CO_2 (carbon dioxide) and OCS (carbonyl sulfide). A Franck-Condon analysis is performed on the Auger spectra subsequent to O $1s^{-1}$ and N $1s^{-1}$ photoionizations of the NO molecule, on the Auger spectrum subsequent to C $1s^{-1}$ photoionization of the CO_2 molecule, and on the Auger spectrum subsequent to S $2p^{-1}$ photoionization of the OCS molecule. All molecules were selected for two reasons. First, vibrational progressions were expected in the Auger spectra prior to the measurements. This required a knowledge of the expected metastable dicationic states with vibrational splittings that are larger than the lifetime broadenings of the core-ionized states. Second, the molecules should be of high interest.

Open-shell molecules are rather reactive due to their electronic structure. The most stable ones, which are manageable with the present experimental setup, are NO and O_2. Since it was expected and later shown by Arion *et al.* [20] that the O_2 molecule does not show clear vibrational progressions in the Auger spectrum, the present work focused on the NO molecule.

CO_2 is formed by combustion of fuel, and its percentage in the atmosphere increased significantly since the beginning of the industrial revolution. It is a well-known greenhouse gas that, consequently, plays an important role in global warming, a phenomenon that threatens the climate on our planet. However, it is not only present in the atmosphere of the Earth, but makes also dominant contributions to the atmospheres on the Mars and the Venus; it is therefore of considerable interest in atmospheric research in general. The importance of CO_2^{2+} for ionospheres of different planets, for example, was discussed by Thissen *et al.* [2]. These authors concluded – partially on the present results – that no CO_2^{2+} metastable on a timescale relevant for atmospheric processes can be formed by Auger decay.

OCS, which is emitted from the oceans or by volcanos, is the major sulfur com-

pound naturally present in the Earth's atmosphere. It plays a role in the formation of aerosols in the atmosphere and has, therefore, influence on the Earth's climate. In addition, Leman *et al.* [21] demonstrated that in prebiotic chemistry OCS plays a role in the formation of peptides from amino acids, *i.e.* it may be an important molecule in the formation of proteins and hence for the development of life. The OCS molecule and its ions are known to be very stable, and even the lifetime of the triply charged cation OCS^{3+} had been shown by mass-spectrometry studies to be of the order of a few microseconds [22]. Very recently, Eland *et al.* [23] had calculated the potential-energy surfaces of a large number of states of the latter species confirming the observation of metastable OCS^{3+}. In the 1980s, Ridard *et al.* [24] had calculated a lifetime of 10^{160} s for the ground state of OCS^{2+}. Thirty years later, a large number of metastable states were theoretically predicted for OCS^{2+} by Brites *et al.* [25].

As expected, all Auger spectra revealed vibrational structures and were subjected to a Franck-Condon analysis. In this way for all observed dicationic states equilibrium distances, vibrational energies, and anharmonicities were derived. The Franck-Condon analysis of the corresponding photoelectron spectra was performed as well in order to obtain information on the potential-energy curves of the core-ionized states. This information was used for the subsequent analyses of the Auger spectra. While the vibrational progressions in the photoelectron spectra of the studied molecules are known from previous work, the vibrational progressions in the Auger spectra were all for the first time clearly resolved.

Chapter 1

Theoretical basis

The main goal of the present work is to obtain detailed information on the electronic structure and, in particular, on the potential-energy curves of metastable molecular dications. For this purpose, core-level photoelectron and Auger spectra of the respective molecules were measured. Since the core-ionized and the dicationic states of the studied molecules are either stable or metastable, vibrational progressions are observed in the photoelectron and Auger spectra. The information of interest is obtained by analysing these vibrational progressions. The present approach is strongly based on a curve-fitting procedure in combination with a Franck-Condon analysis, *i.e.* by calculating the overlap of the vibrational wave functions of the different electronic states involved in the process. Contrary to most of the analyses presented in the literature, the fit parameters of the present analysis are not restricted to peak positions, intensities, or widths of the spectral lines. Instead, we describe complete vibrational progressions of electronic transitions on the basis of molecular parameters such as internuclear distances, vibrational energies, and anharmonicities, *i.e.* the fitting curves are based on primary physical quantities. The aim of the present chapter is to describe the physical laws used to specify the fitting curves, *i.e.* the curves fitted to the data. In other words, the aim of this chapter is to show how the photoelectron and Auger spectra are related to the molecular properties and how this information can be derived from the spectra.

The heart of the present data analysis is the validity of the Born-Oppenheimer approximation described in Section 1.1. Using this approximation, the electronic and the nuclear motions in a molecule are considered to be independent, which is the prerequisite for performing the Franck-Condon analysis.

To describe the vibrational progressions in the Franck-Condon analysis quantitatively, Morse potentials are assumed for all electronic states. The Morse potential is chosen to model the potential-energy curves, since it can be fully described by only four parameters. This fact is of great importance because it allows to perform the fit analysis also in case of complex spectra with strongly overlapping vibrational progressions. The Morse potential is discussed in Section 1.2.

In Section 1.3, the photoionization process and the Auger decay are discussed. In this section we specify electronic states involved in these processes and present a quantum-mechanical description of the photoionization process and the Auger decay. Moreover, we introduce in this section some basic notations used throughout

the entire thesis.

The mentioned Franck-Condon analysis, which is used to derive information on the potential-energy curves, is described in Section 1.4.

The Franck-Condon analysis can only be applied along one normal coordinate. In a diatomic molecule, the normal coordinate is – beside some constants – identical with the internuclear distance. However, for a polyatomic molecule, the normal coordinates are normally not identical with the internuclear distances or the interbond angles. In Section 1.5 we describe how a relation of the internuclear distances and the interbond angles to the normal coordinates can be established. In this section we also describe the principles of a multidimensional Franck-Condon analysis, which may be required to study the spectra of polyatomic molecules.

The symbolic notations for the configurations of the electronic states are explained in Section 1.6.

In the present photoelectron spectra, the lifetime broadening caused by finite lifetimes on the core-ionized states is comparable to the vibrational splittings with the consequence that the different vibrational substates visible in the spectra partially overlap. Due to this fact, we cannot describe the photoionization process and the Auger decay independently. Instead, the lifetime interference discussed in Section 1.7 has to be taken into account.

In Section 1.8, we introduce the post-collision-interaction effect, which originates from an interaction of the photoelectron and Auger electron subsequent to their ejections from the molecule. Although this effect is in most cases rather small, it shows still a significant influence on the fit results.

1.1 Born-Oppenheimer approximation

The Schrödinger equation for a molecule (or a molecular ion) consisting of n electrons and N nuclei is defined as

$$\mathcal{H}\Phi_{\varepsilon v}(\boldsymbol{x},\boldsymbol{X}) = \mathcal{E}_{\varepsilon v}\cdot\Phi_{\varepsilon v}(\boldsymbol{x},\boldsymbol{X}). \tag{1.1}$$

The indices ε and v are used to distinguish different solutions of the Schrödinger equation; their physical meaning is discussed at the end of this section for didactic reasons. The argument $\boldsymbol{x} = (x_1^i, x_1^j, x_1^k, x_2^i, x_2^j, x_2^k, \ldots, x_n^i, x_n^j, x_n^k)$ describes the locations of the electrons, and the argument $\boldsymbol{X} = (X_1^i, X_1^j, X_1^k, X_2^i, X_2^j, X_2^k, \ldots, X_N^i, X_N^j, X_N^k)$ the locations of the nuclei. The full non-relativistic Hamiltonian $\mathcal{H}$ has the form

$$\mathcal{H} = -\frac{\hbar^2}{2}\cdot\sum_{i=1}^{n}\frac{1}{m}\cdot\Delta_i - \frac{\hbar^2}{2}\cdot\sum_{I=1}^{N}\frac{1}{M_I}\cdot\Delta_I + \mathcal{V}(\boldsymbol{x},\boldsymbol{X}). \tag{1.2}$$

Here $\hbar$ is the reduced Planck constant, m the electronic mass, M_I the mass of the I^{th} nucleus, and $\Delta_i = \nabla_i^2$ $\{\Delta_I = \nabla_I^2\}$ the Laplace operator for the i^{th} electron {the I^{th} nucleus}, where ∇_i $\{\nabla_I\}$ is the nabla operator. The first and second terms in eqn. 1.2 represent the kinetic-energy operators of the electrons and the nuclei, respectively, and the third term $\mathcal{V}(\boldsymbol{x}, \boldsymbol{X})$ is the full Coulomb-like potential energy of the molecule. The last represents a sum of three components, namely

$$\mathcal{V}(\boldsymbol{x}, \boldsymbol{X}) = \mathcal{V}^{ee}(\boldsymbol{x}) + \mathcal{V}^{en}(\boldsymbol{x}, \boldsymbol{X}) + \mathcal{V}^{nn}(\boldsymbol{X}), \tag{1.3}$$

where $\mathcal{V}^{ee}(\boldsymbol{x})$ describes the repulsive interaction between the electrons, $\mathcal{V}^{nn}(\boldsymbol{X})$ the repulsive interaction between the nuclei, and $\mathcal{V}^{en}(\boldsymbol{x}, \boldsymbol{X})$ the attractive interaction between the electrons and the nuclei.

Due to the large differences in the masses of electrons and nuclei, the motion of electrons is much faster than the motion of nuclei. As a consequence, the electrons can respond immediately to changes in the nuclear positions so that they can be considered to move in an electrostatic field arising from the nuclei. In other words, the motions of the electrons and the nuclei can be considered separately, and the total wave function $\Phi_{\varepsilon v}(\boldsymbol{x}, \boldsymbol{X})$ can be presented as a product of the electronic $\psi_\varepsilon(\boldsymbol{x}; \boldsymbol{X})$ and the nuclear $\Psi_{\varepsilon v}(\boldsymbol{X})$ components, *i.e.*

$$\Phi_{\varepsilon v}(\boldsymbol{x}, \boldsymbol{X}) = \psi_\varepsilon(\boldsymbol{x}; \boldsymbol{X}) \cdot \Psi_{\varepsilon v}(\boldsymbol{X}). \tag{1.4}$$

The sign ";" in the designation of the wave function $\psi_\varepsilon(\boldsymbol{x}; \boldsymbol{X})$ indicates that this function depends on the argument $\boldsymbol{X}$ just parametrically in the sense that for each arrangement of the nuclei $\boldsymbol{X}$ there is a different wave function $\psi_\varepsilon(\boldsymbol{x})$. The representation of a molecular wave function in the form of eqn. 1.4 is also known as the *adiabatic approximation*.

Generally speaking, the nuclear wave function $\Psi_{\varepsilon v}(\boldsymbol{X})$ in eqn. 1.4 has to describe the vibrational as well as the rotational motions of the nuclei. Since in this study only electronic and vibrational but no rotational states are observed, the rotational motion is not taken into account. Consequently, in the present case, the wave function $\Psi_{\varepsilon v}(\boldsymbol{X})$ is considered to describe only the vibrational motion and it is called the *vibrational wave function*, while the wave function $\psi_\varepsilon(\boldsymbol{x}; \boldsymbol{X})$ describes the electronic motion and it is called the *electronic wave function*.

After substitution of the wave function from eqn. 1.4 and the Hamilton operator from eqn. 1.2 into the Schrödinger equation 1.1 and by assuming that the term

$$-\frac{\hbar^2}{2} \cdot \sum_{I=1}^{N} \frac{1}{M_I} \cdot (2 \cdot \nabla_I \psi_v(\boldsymbol{x}; \boldsymbol{X}) \cdot \nabla_I \Psi_{\varepsilon v}(\boldsymbol{X}) + \Psi_{\varepsilon v}(\boldsymbol{X}) \cdot \Delta_I \psi_v(\boldsymbol{x}; \boldsymbol{X})) \tag{1.5}$$

can be neglected, the initial wave equation can be split into two equations: one for

the electrons and another for the nuclei, *i.e.*

$$\left(-\frac{\hbar^2}{2m}\cdot\sum_{i=1}^{n}\Delta_i+\mathcal{V}(\boldsymbol{x},\boldsymbol{X})\right)\psi_\varepsilon(\boldsymbol{x};\boldsymbol{X})=V_\varepsilon(\boldsymbol{X})\cdot\psi_\varepsilon(\boldsymbol{x};\boldsymbol{X}) \tag{1.6}$$

and

$$\left(-\frac{\hbar^2}{2}\cdot\sum_{I=1}^{N}\frac{1}{M_I}\cdot\Delta_I+V_\varepsilon(\boldsymbol{X})\right)\Psi_{\varepsilon v}(\boldsymbol{X})=E_{\varepsilon v}\cdot\Psi_{\varepsilon v}(\boldsymbol{X}), \tag{1.7}$$

respectively (for details of the derivation of these formulas for the case of the simplest molecule H_2^+ see the book of Atkins and Friedman [26]). The conditions when the term given in eqn. 1.5 can be neglected are the essence of the *Born-Oppenheimer approximation* [27]. They are fulfilled when the electronic wave function $\psi_\varepsilon(\boldsymbol{x};\boldsymbol{X})$ varies so quickly with the nuclear coordinates $\boldsymbol{X}$ that its first and second derivatives with respect to $\boldsymbol{X}$ can be neglected. Assuming the Born-Oppenheimer approximation to be valid, the total energy of the molecule $\mathcal{E}_{\varepsilon v}$ presented in eqn. 1.1 becomes the total energy of the molecule $E_{\varepsilon v}$ presented in the nuclear equation 1.7. The total energy in the electronic equation $V_\varepsilon(\boldsymbol{X})$ represents the potential energy for the nuclear motion. The graph of this function is called the *potential-energy curve* or, more generally – in the case of a polyatomic molecule, – the *potential-energy surface* of the electronic state; the determination of the functions $V_\varepsilon(\boldsymbol{X})$ from experimental results is a main goal of the present study.

From the Schrödinger equations 1.6 and 1.7, the meaning of the quantum numbers ε and v used in eqns. 1.1 and 1.4 becomes obvious – the former marks all possible electronic states and is called the *electronic-state quantum number*, and the latter all possible vibrational states and is called the *vibrational quantum number*.

1.2 Morse potential

In Section 1.1 the wave equation for the nuclei is derived, see eqn. 1.7. Let us now apply this equation to the case of a molecule (or a molecular ion) consisting of two nuclei ($N=2$) having the masses M_1 and M_2, and, moreover, turn from the problem of two nuclei to the problem of one bond between them. In other words, let us replace the coordinates $\boldsymbol{X}=(X_1^i,X_1^j,X_1^k,X_2^i,X_2^j,X_2^k)$ by the *internuclear distance* R. In this case, eqn. 1.7 can be rewritten as

$$\left(-\frac{\hbar^2}{2\mu}\cdot\frac{d^2}{dR^2}+V(R)\right)\Psi_v(R)=E_v\cdot\Psi_v(R), \tag{1.8}$$

where

$$\mu=\frac{M_1\cdot M_2}{M_1+M_2}$$

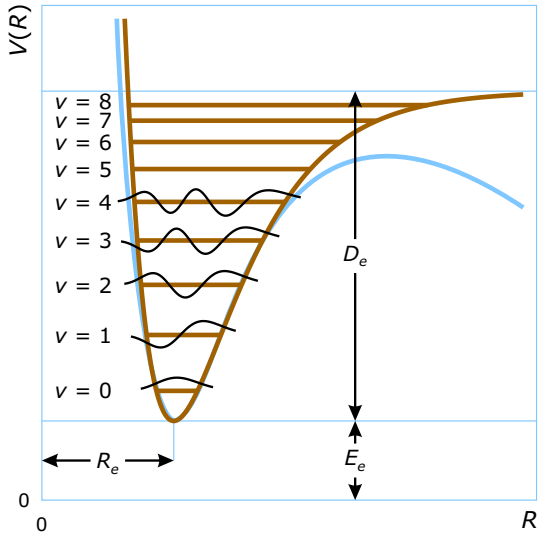

Figure 1.1: Morse potential (brown curved line) with the vibrational sublevels (brown horizontal lines) and the wave functions (black lines) as well as a more realistic potential-energy curve for a state being metastable with respect to dissociation (blue line).

is the *reduced mass*. In the present section we consider only one electronic state and, therefore, omit the electronic-state quantum number ε in the notations of all parameters.

The wave equation 1.8 can be solved by assuming a potential-energy function $V(R)$. In the present study we use the *Morse potential* [28], which is defined as

$$V(R) = E_e + D_e \cdot \left(1 - e^{-a\cdot(R-R_e)}\right)^2 \tag{1.9}$$

(for details on the Morse potential see the book of Atkins and Friedman [29]); the graph of such a function is shown in Figure 1.1. The Morse potential is actually empirical and describes the potentials of many molecules very well. In the present work it is used for all electronic states being stable or metastable with respect to dissociation, in spite of the fact that real potential energies of such states can considerably differ from the Morse potential; a more realistic potential-energy curve is shown in the figure as well (blue line). The fact that we can, nevertheless, use Morse potentials in the data analysis is discussed further below, see page 18. Contrary to this, dissociative electronic states are in the present work not described on the basis of potential-energy curves. Instead, we describe the corresponding transitions with an empirical lineshape, see Appendix A.

As mentioned above, one advantage of the Morse potential as compared to other models is that it is defined by a small number of parameters. This plays a crucial role in the fit analysis of complex spectra. In the following, we summarize these parameters, which are called in this thesis the *Morse parameters*.

The Morse-potential curve has a minimum at the internuclear distance R_e – the so-called *equilibrium distance* – and the potential energy E_e. In contrast to the

potential-energy curve of the harmonic oscillator, the Morse-potential curve has an asymmetrical form. The shape of the curve is defined by the parameters D_e and a. The former giving the depth of the curve minimum is called the *dissociation energy* and has the following meaning: the vibrational states are bound at energies less than $(E_e + D_e)$ and are in the continuum at energies above this value. The magnitude a is

$$a = \sqrt{\frac{F}{2D_e}}, \tag{1.10}$$

where F is the *force constant* of the oscillator well known from Hook's law.

Solving the Schrödinger equation 1.8 using a Morse potential, we obtain the eigenvalues

$$E_v = E_e + \hbar\omega \cdot \left(v + \frac{1}{2}\right) - x\hbar\omega \cdot \left(v + \frac{1}{2}\right)^2 \tag{1.11}$$

and the eigenvectors $\Psi_v(R)$; the corresponding vibrational sublevels and wave functions are also shown in Figure 1.1. The parameter ω is the *angular frequency* defined as

$$\omega = \sqrt{\frac{F}{\mu}}. \tag{1.12}$$

The dimensionless quantity x from eqn. 1.11 is called the *anharmonicity constant* and can be expressed as

$$x = \frac{a^2 \cdot \hbar}{2\mu \cdot \omega} \ll 1. \tag{1.13}$$

Using eqns. 1.10, 1.12, and 1.13, we can present the depth of the minimum of the curve as

$$D_e = \frac{(\hbar\omega)^2}{4 \cdot x\hbar\omega}. \tag{1.14}$$

If we divide eqns. 1.10 and 1.12 by each other and replace in the obtained result the parameter D_e by its expression in the from of eqn. 1.14, we find

$$a = \frac{\sqrt{2\mu \cdot x\hbar\omega}}{\hbar}. \tag{1.15}$$

As can be seen from the last two formulas, the shape of the Morse-potential-energy curve can be fully described not only by the two parameters D_e and a, but also by the two parameters $\hbar\omega$ and $x\hbar\omega$; in the present study, the latter set of parameters is used. We call these parameters the *vibrational energy* $\hbar\omega$ and the *anharmonicity* $x\hbar\omega$. Thus, for a full description of each Morse potential, we use the following Morse parameters:

- ▷ equilibrium distance R_e,

- ▷ vibrational energy $\hbar\omega$,
- ▷ anharmonicity $x\hbar\omega$,
- ▷ energy position of the minimum E_e.

Equations 1.14 and 1.15 can be used to construct the potential-energy curves based on the obtained vibrational energies and anharmonicities in order to compare them with theoretical results, see Figures 3.6 and 3.7.

Some additional properties of the Morse potential should also be mentioned. The first one is that the number of vibrational sublevels of the anharmonic oscillator, in contrast to the harmonic one, is not infinite; *i.e.* the vibrational number can possess the values $v = 0, 1, \ldots, v^{max}$. Here the number v^{max} is the maximum possible integer being less than

$$\frac{1}{2x} - \frac{1}{2}$$

that can be readily found using eqns. 1.11 and 1.14. From eqn. 1.11 the energy difference between two neighboring vibrational levels v and $(v + 1)$ can also be found; it amounts to

$$\Delta E_v = \hbar\omega - 2 \cdot x\hbar\omega \cdot (v + 1)\,. \tag{1.16}$$

Using this formula, values of the parameters $\hbar\omega$ and $x\hbar\omega$ can be estimated on the basis of the relative positions ΔE_v of at least three vibrational peaks observed in the spectrum. The formula is applied repeatedly in this study in order to convert peak position reported in the literature to vibrational energies and anharmonicities used in the present work; see, for example, Table 3.2.

1.3 Photoionization and Auger decay

A schematic picture of the photoionization process and the subsequent Auger decay studied in the present work as well as of the electronic states involved in these processes is represented in Figure 1.2. For reasons of simplicity, only one core level and two valence levels are indicated. In the first step, the neutral molecule (frame A) absorbs a photon and emits an electron, which originates in the present work from the uppermost core level (frame B, transition 1) that is also called the *shallow core level*. Molecules with a vacancy in the shallow core level (frame C) have a longer lifetime than molecules with vacancies in deeper core levels. This results in narrower spectral lines and the possibility to observe vibrational progressions (a necessary prerequisite for the analysis of a spectrum, see page 18). Since the singly ionized molecule with a vacancy in a core level is unstable, the system tries to minimize the energy (frame D). As a result of this, an electron from an upper level fills the formed vacancy (transition 2). The energy released by such a transition is

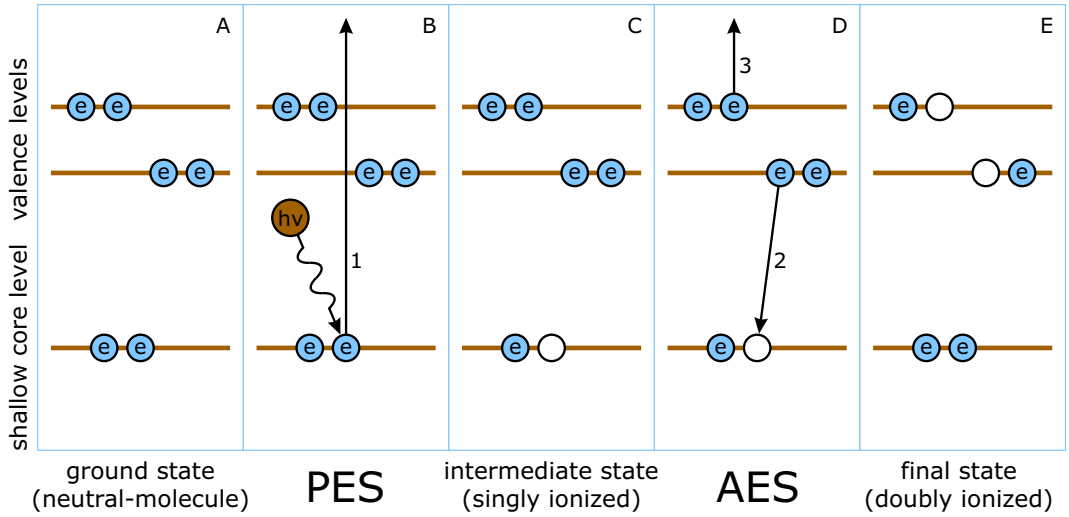

Figure 1.2: Scheme of the photoionization process and the subsequent Auger decay used in the present work. For a description of the frames see text.

transferred by the Coulomb interaction to a third electron, which also leaves the ion taking away the excess energy (transition 3). The excess energy, in principle, can be taken away also by X-ray emission. However, this process is strong only for core levels with binding energies well above 1 keV. Thus, finally, a doubly ionized molecule with two vacancies in valence levels (frame E) is obtained.

The process of emitting the first electron is called *photoionization* and the corresponding ejected electron (transition 1) the *photoelectron*, while the subsequent process of energy minimization is called the *Auger effect* [30, 31] or the *Auger decay*, and the corresponding ejected electron (transition 3) the *Auger electron*. The corresponding transition is called the *Auger transition*. Here it should be mentioned that the Auger process presented in the figure is also known as a *normal Auger decay* contrary to a *resonant Auger decay*, *i.e.* to the case when the first electron is not ejected but excited to an upper level. Since only the normal Auger decay is studied in this work, we omit the word "normal" throughout the text.

The processes shown in the figure can be briefly presented by the following schemes: the photoionization process can be presented as

$$\mathrm{M} + \mathrm{h}\nu \rightarrow \mathrm{M}^{+*} + \mathrm{e}^{ph},$$

and the subsequent Auger decay as

$$\mathrm{M}^{+*} \rightarrow \mathrm{M}^{2+} + \mathrm{e}^{A}.$$

Here M, M^{+*}, and M^{2+} denote the neutral-molecule, the singly ionized, and the doubly ionized states, respectively, $\mathrm{h}\nu$ the incident photon, and e^{ph} and e^{A} the out-

going photoelectron and Auger electron. In order to underline that the singly ionized state is always excited (due to core ionization), this state is marked with the sign "$*$". The doubly ionized molecules can also be in an electronically excited state. However, the lifetimes of the excited states are very long as compared to the timescale of the photoionization process and the Auger decay. As a consequence, in the present Auger spectra no differences in the linewidths can be found for transitions to the ground state or to the excited states of the doubly ionized molecule.

It is already mentioned that for the molecules studied in this work the vibrational splitting is comparable to the lifetime broadening so that the vibrational substates overlap in the spectra. As a consequence, lifetime interference has to be taken into account, and the photoionization process and the Auger decay have to be described as one process, see page 32. Therefore, we refer to the neutral-molecule state as the *ground state* g, to the core-ionized state as the *intermediate state* i, and to the doubly ionized state as the *final state* f of the entire process, see Figure 1.2. In this thesis, it is sometimes necessary to specify the ground, the intermediate, and the final states with the quantum numbers ε and v. In these cases, the quantum numbers are indicated with double prime (the ground state), with single prime (the intermediate state), or without primes (the final state); see, for example, Figure 1.5.

Let us present the kinetic energies of the photoelectrons and the Auger electrons using the total energies of the neutral-molecule state E_g, the singly ionized state E_i, and the doubly ionized state E_f. In accordance with the energy conservation law, the kinetic energy of the photoelectron ejected by the transition $g \to i$ can be expressed as

$$T_{gi}^{ph} = h\nu - B_{gi}, \tag{1.17}$$

where $h\nu$ is the energy of the photon, and $B_{gi} = E_i - E_g$ is the *binding energy* of the respective core level. In an analogous way, the kinetic energy of the Auger electron ejected by the transition $i \to f$ can be expressed as

$$T_{if}^{A} = E_i - E_f. \tag{1.18}$$

The kinetic-energy distribution of the photoelectrons is called the *photoelectron spectrum* (PES); in the present work the photoelectron spectra are displayed as a function of binding energy. When the kinetic energies of the Auger electrons are registered, the corresponding spectrum is called the *Auger-electron spectrum* (AES) or the *Auger spectrum*.

Quantum-mechanical description

The probabilities for the transitions in the photoionization process and the Auger decay can be found with the corresponding matrix elements. So, the probability

of the photoionization process, *i.e.* the probability of a transition leading to the intermediate state i, is given by the square modulus of the *electric-dipole-transition moment*

$$\boldsymbol{D}_{gi} = \langle i|\boldsymbol{\mathcal{D}}|g\rangle. \tag{1.19}$$

Here the magnitude $\boldsymbol{\mathcal{D}}$ is the *electric-dipole moment operator* defined as

$$\boldsymbol{\mathcal{D}} = -e \cdot \sum_{a=1}^{n} \boldsymbol{r}_a + e \cdot \sum_{A=1}^{N} Z_A \cdot \boldsymbol{R}_A = \boldsymbol{\mathcal{D}}^e + \boldsymbol{\mathcal{D}}^n, \tag{1.20}$$

where the first part of the sum $\boldsymbol{\mathcal{D}}^e$ affects the electronic coordinates $\boldsymbol{r}_a = (x_a^i, x_a^j, x_a^k)$, while the second part $\boldsymbol{\mathcal{D}}^n$ the nuclear coordinates $\boldsymbol{R}_A = (X_A^i, X_A^j, X_A^k)$; e is the elementary charge, and Z_A is the atomic number of the A^{th} nucleus. The second part is suited to describe the vibrational transition in infrared spectroscopy; consequently, it can be neglected in the present work.

The square modulus of the *Coulomb matrix element*

$$C_{if} = \langle f|\mathcal{C}|i\rangle \tag{1.21}$$

gives the probability of the Auger decay, *i.e.* the probability of the transition from the intermediate state i to the final state f. The magnitude $\mathcal{C}$ presented here is the *Coulomb operator*, which can be written in the form

$$\mathcal{C} = e^2 \cdot \sum_{a=1}^{n-1} \sum_{b=a+1}^{n} \frac{1}{|\boldsymbol{r}_a - \boldsymbol{r}_b|}. \tag{1.22}$$

The ground state g, the intermediate state i, and the final state f in eqns. 1.19 and 1.21 are described by the total wave functions, *i.e.* by wave functions consisting of an electronic and a vibrational part.

As mentioned above, the core-ionized state is unstable and decays through the emission of an Auger electron, *i.e.* it exists only for a finite *lifetime*. Contrary to this, the studied doubly ionized states have their vacancies in valence levels and have lifetimes which can be considered to be infinite as compared to the lifetimes of the core-ionized states. In the present context, we consider only dicationic states which are metastable; the long lifetimes of such states of the studied molecules are reported in the literature [24, 32, 33, 34].

Due to the infinite lifetime of the ground state and the extremely long lifetimes of the final states, the linewidths ΔT_i of the present spectra are determined by the finite lifetimes Δt_i of the core-ionized states i using the *energy-time uncertainty relation* [35]

$$\Delta T_i \cdot \Delta t_i \approx \hbar. \tag{1.23}$$

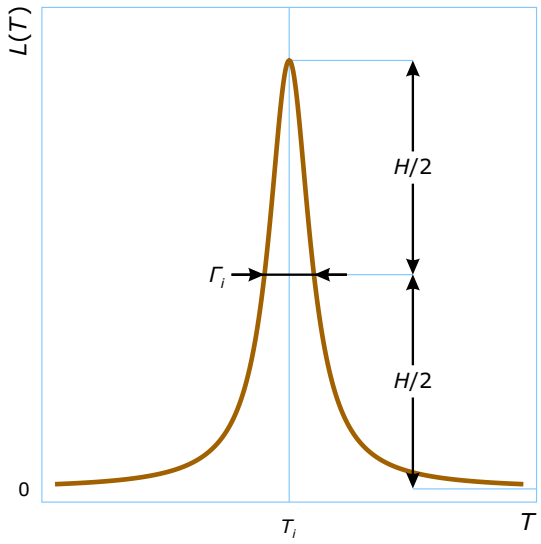

Figure 1.3: Lorentzian function describing the distribution over the kinetic energies in the photoelectron and Auger spectra.

The exact lineshape is given by the *Lorentzian function*

$$L_i(T) = \frac{\Gamma_i}{2\pi} \cdot \frac{1}{(T - T_i)^2 + \left(\frac{\Gamma_i}{2}\right)^2} \tag{1.24}$$

shown in Figure 1.3 (for details of the derivation of this function see the book of Atkins and Friedman [36]). The parameter Γ_i describing the *lifetime broadening* is called the *lifetime width* and is defined as the *full width at half maximum* (FWHM) of the function. The peak of the function is located at the kinetic energy T_i defined by eqn. 1.17 or 1.18. The function is normalized to unit area under the curve. Hence, the lifetime of the intermediate state Δt_i can be derived from the uncertainty relation 1.23 as

$$\Delta t_i = \frac{\hbar}{\Gamma_i}. \tag{1.25}$$

The Auger decay can be considered in terms of *Auger-transition rates* that are theoretically described by Wentzel [37]. The rate of the Auger transition from the intermediate state i (to any final state) – or the probability of the transition per unit time – is defined, in accordance with eqn. 1.25, as

$$W_i = \frac{1}{\Delta t_i} = \frac{\Gamma_i}{\hbar}. \tag{1.26}$$

The Auger-transition rate can be also presented in the form

$$W_i \propto \sum_f |\langle f|\mathcal{C}|i\rangle|^2,$$

where the matrix element $\langle f|\mathcal{C}|i\rangle$ is given by eqn. 1.21. The summation here is performed over all possible channels f of the total wave functions $\Phi_f(\boldsymbol{x}, \boldsymbol{X})$ (including the continuum wave functions). From the last two expressions, we can conclude that a higher probability of the Auger transition leads to a more rapid rate, to a shorter lifetime, and to a larger lifetime width.

1.4 Franck-Condon analysis

In Section 1.1, the adiabatic approximation is presented. It says that electrons respond immediately to any changes of the nuclear positions due to their negligible masses as compared to those of the nuclei. Contrary to this, nuclei cannot immediately change their positions if, due to processes like photoionization or Auger decay, the electronic configuration is changed. In other words, all electronic transitions occur at fixed positions of the nuclei. This statement is known as the *Franck-Condon principle* [38, 39, 40].

In the following, we discuss the Franck-Condon principle in the general case, *i.e.* independently of the photoionization process or the Auger decay studied in this work. For this purpose we designate the electronic-state quantum numbers of the initial and the final states of the considered process by ε' and ε, respectively, and the vibrational quantum numbers of these states by v' and v. The couple of the quantum numbers labeling the initial state, namely $\varepsilon' v'$, is designated as i, and this labeling the final state, namely εv, as f.

The essence of the Franck-Condon principle is illustrated in Figure 1.4, where the electronic initial and the electronic final states are represented by the potential-energy curves. In order to simplify the complete picture, only one vibrational level of the electronic initial state, namely $v' = 0$, is shown. According to the Franck-Condon principle, all transitions from one electronic state to another one occur at a constant internuclear distance; as a consequence, the transitions can be shown in the figure by a vertical arrow. One of these transitions, namely $v' = 0 \rightarrow v = 2$, is indicated in the figure.

The probability of the transition $i \rightarrow f$ is given by the square modulus of the appropriate matrix element

$$A_{if} = \langle f|\mathcal{A}|i\rangle,$$

where the initial state i and the final state f are described using the total wave functions, and $\mathcal{A}$ is the operator describing this process. In the adiabatic approximation, the total wave function for the initial state $|i\rangle$ {the final state $|f\rangle$} is a product of the electronic wave function $|\varepsilon'\rangle$ {$|\varepsilon\rangle$} and the vibrational wave function $|v'\rangle$ {$|v\rangle$}, see eqn. 1.4. In the present study, the operator $\mathcal{A}$ can be the electric-dipole moment operator $\boldsymbol{\mathcal{D}}^e$ or the Coulomb operator $\mathcal{C}$, and it acts only on the electronic part of the

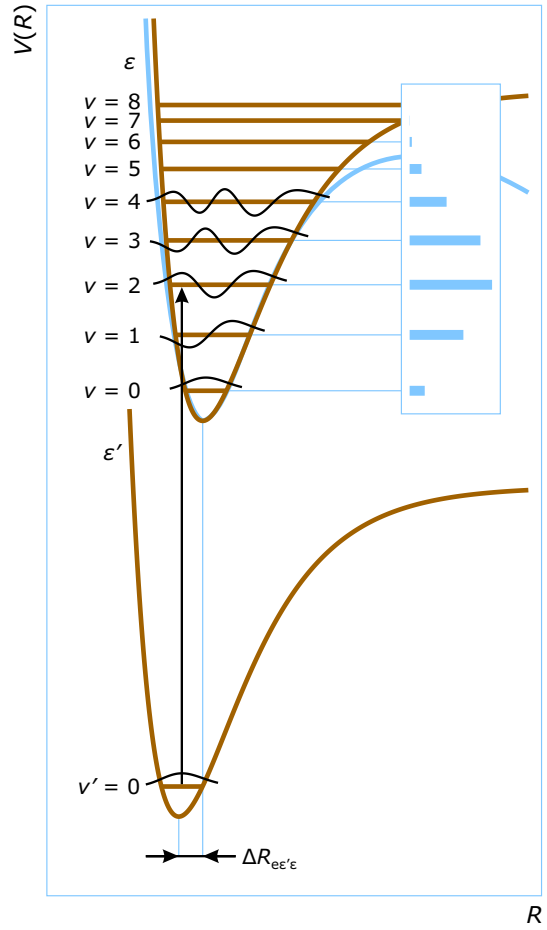

Figure 1.4: Forming of the vibrational progression (blue bars) based on the Franck-Condon analysis, assuming a Morse potential. For a description of the lines see Figure 1.1.

wave function; see eqns. 1.20 and 1.22, respectively. As a result, the matrix element A_{if} can be represented as the product of two factors, namely

$$A_{if} = A_{\varepsilon'\varepsilon} \cdot F_{v'v}. \tag{1.27}$$

Here $A_{\varepsilon'\varepsilon}$ is the matrix element of the electronic transition $\varepsilon' \rightarrow \varepsilon$ defined as

$$A_{\varepsilon'\varepsilon} = \langle \varepsilon | \mathcal{A} | \varepsilon' \rangle,$$

while $F_{v'v}$ is the matrix element of the vibrational transition $v' \rightarrow v$ within the electronic transition, defined as

$$F_{v'v} = \langle v | v' \rangle. \tag{1.28}$$

The intensity of the transition $i \rightarrow f$ is proportional to the square modulus of the matrix element A_{if}. Therefore, from eqn. 1.27 this intensity can be obtained as

$$I_{if} \propto |A_{\varepsilon'\varepsilon}|^2 \cdot |F_{v'v}|^2.$$

Since for a given electronic transition $\varepsilon' \rightarrow \varepsilon$ the factor $|A_{\varepsilon'\varepsilon}|^2$ is a constant, the intensity of the vibrational transition $v' \rightarrow v$ is given by

$$I_{v'v} \propto |F_{v'v}|^2.$$

The last expression can be used in the following way. If we know the potential-energy curves for both the electronic initial and the electronic final states, we can calculate for these states the total energies and the vibrational wave functions. From this the overlap integral $F_{v'v}$ for each vibrational transition $v' \rightarrow v$ can be found, see eqn. 1.28, and the *vibrational progression* for the electronic transition $\varepsilon' \rightarrow \varepsilon$ can be constructed. Such a vibrational progression is shown in the upper right corner of Figure 1.4. The overlap integral $F_{v'v}$ is called the *Franck-Condon factor*. As can be seen from eqn. 1.28, the most intense line of a vibrational progression corresponds to a transition for which the overlap integral has the maximum value; in Figure 1.4 this transition is $v' = 0 \rightarrow v = 2$.

As a matter of fact, most often, the vibrational progression as well as the potential-energy curve for the electronic initial state is known: the former from an experiment, and the latter from literature. In such a case, the potential-energy curve for the electronic final state can be constructed by assuming a model potential. Values of the parameters defining this potential can be obtained by matching the calculated curve to the data points in an iterative way. Such a kind of calculations is called a *Franck-Condon analysis* and can be performed within the *fit analysis* as done in the present work.

In the present case of assuming Morse potentials, the vibrational progression is fully defined by the vibrational energies $\hbar\omega_{\varepsilon'}$ and $\hbar\omega_{\varepsilon}$, the anharmonicities $x_{\varepsilon'}\hbar\omega_{\varepsilon'}$ and $x_{\varepsilon}\hbar\omega_{\varepsilon}$ as well as the difference between the equilibrium distances of the two electronic states $\Delta R_{e\varepsilon'\varepsilon} = R_{e\varepsilon} - R_{e\varepsilon'}$, see Figure 1.4. Thus, the present Franck-Condon analysis allows to obtain values of the parameters $\hbar\omega_{\varepsilon}$, $x_{\varepsilon}\hbar\omega_{\varepsilon}$, and $\Delta R_{e\varepsilon'\varepsilon}$, once values of the parameters $\hbar\omega_{\varepsilon'}$ and $x_{\varepsilon'}\hbar\omega_{\varepsilon'}$ are known. An example of a vibrational structure observed in the present spectra and used in a Franck-Condon analysis is displayed in Figure 3.10; examples of complex vibrational progressions, constructed on the basis of the fit results, are shown in Figures 3.15 and 3.17.

The Morse potential used in the present work is only an approximation that is not strictly valid for all electronic states. This is, in particular, valid for the states which have typically a potential-energy curve as indicated in Figure 1.4 (blue line). Nevertheless, the Morse potential can be applied when the differences between the real potentials and the Morse potential are small within the Franck-Condon region. In this case, a good description of the data points by the fitting curve is obtained. If the differences between the assumed potential and the real potentials become large, the fitting curve does not fit well to the data points; see, for example, the Auger transition to the state $d^1\Sigma^+$ of CO^{2+} [15] as well as the Auger transition to the

state $^1\Sigma_g^+$ of CO_2^{2+} shown in Figure 3.9. In conclusion, we can check the validity of the assumed Morse potential by the quality of the fit result.

Let us now specify eqn. 1.27 for the photoionization process and the Auger decay. For the photoionization process, namely for the transition $g \to i$, the matrix element A_{gi} has to be identified with the matrix element $\boldsymbol{D}_{gi}$, see eqn. 1.19, while the operator $\mathcal{A}$ is identical with the operator $\boldsymbol{\mathcal{D}}^e$, see eqn. 1.20. By indicating the ground state g with double prime and the intermediate state i with prime, see page 13, we get

$$\boldsymbol{D}_{gi} = \boldsymbol{D}_{\varepsilon''\varepsilon'} \cdot F^{ph}_{v''v'}, \tag{1.29}$$

with $\boldsymbol{D}_{\varepsilon''\varepsilon'}$ being the electric-dipole-transition moment defined as

$$\boldsymbol{D}_{\varepsilon''\varepsilon'} = \langle \varepsilon' | \boldsymbol{\mathcal{D}}^e | \varepsilon'' \rangle, \tag{1.30}$$

and $F^{ph}_{v''v'}$ being the Franck-Condon factor for the photoionization process (for details of the derivation of eqn. 1.29 see the book of Atkins and Friedman [41]).

In the case of the Auger decay, we have to consider the probability of the Auger transition $i \to f$ defined in the previous section as the square modulus of the matrix element C_{if} given by eqn. 1.21 with the operator $\mathcal{C}$ given by eqn. 1.22. Analogous to the arguments presented above, the matrix element C_{if} can be rewritten as

$$C_{if} = C_{\varepsilon'\varepsilon} \cdot F^{A}_{v'v}, \tag{1.31}$$

where $C_{\varepsilon'\varepsilon}$ is the Coulomb matrix element defined as

$$C_{\varepsilon'\varepsilon} = \langle \varepsilon | \mathcal{C} | \varepsilon' \rangle, \tag{1.32}$$

and $F^{A}_{v'v}$ is the Franck-Condon factor for the Auger decay. Note that the quantities without primes refer to the final state f.

1.5 Normal coordinates

In the previous section, we discussed for a diatomic molecule ($N = 2$) how vibrational progressions visible in the photoelectron and Auger spectra are formed; in this case, the vibrational motion occurs along only one coordinate, namely the internuclear distance R. However, in a polyatomic molecule ($N > 2$) there exist several coordinates subject to the vibrational motions; these are the different internuclear distances R_i and the different *interbond angles* α_j. Since these coordinates depend on each other, the potential energy of the molecule cannot be presented as a sum of terms each of which depends on one coordinate; the same situation takes place when almost all other kinds of coordinates are used. As a result, the Franck-Condon analysis cannot be performed. However, there are the so-called *normal*

coordinates $\boldsymbol{Q} = (Q_1, Q_2, \ldots, Q_K)$, which allow to describe the nuclear motion in a molecule by independent vibrational motions, which are called the *normal modes of vibrations* or, simply, the *normal vibrations* (each normal coordinate participates in only one normal vibration and each normal vibration is defined by only one normal coordinate). As a consequence, the Franck-Condon analysis for a polyatomic molecule can be performed in the space of the normal coordinates.

In case of a diatomic molecule (or a diatomic ion), there exist only one normal vibration and only one normal coordinate. On the other hand, in a polyatomic molecule (or a polyatomic ion) there exist $K = 3N - 6$ normal vibrations and normal coordinates for a non-linear molecule and $K = 3N - 5$ if the molecule is linear. The additional normal vibration in a linear molecule (as compared to a non-linear one) defines a rotation around the internuclear axis. We can exclude this vibration from our consideration because it does not change the nuclear locations; the normal coordinate related with this vibration can be excluded as well. Thus, for both kinds of molecule, we consider $K = 3N - 6$ normal vibrations and normal coordinates.

Definition

Let us consider how the normal coordinates are being introduced. In Section 1.1, the locations of the N nuclei of a molecule are defined by the *Cartesian coordinates* $\boldsymbol{X} = (X_1^i, X_1^j, X_1^k, X_2^i, X_2^j, X_2^k, \ldots, X_N^i, X_N^j, X_N^k)$, which represent the positions relative to a common origin. Instead of this, let us consider the positions of the nuclei with the *Cartesian displacement coordinates* $\boldsymbol{P} = (P_1, P_2, \ldots, P_{3N}) = (\Delta X_1^i, \Delta X_1^j, \Delta X_1^k, \Delta X_2^i, \Delta X_2^j, \Delta X_2^k, \ldots, \Delta X_N^i, \Delta X_N^j, \Delta X_N^k)$; from this moment on, a molecular fixed frame is used so that the motions of the molecule as a whole, like translations and rotations, become excluded and only vibrational motions are remained. These coordinates give the displacements of the nuclei from their equilibrium positions. Consequently, a full description of the molecule with the Cartesian displacement coordinates requires $3N$ values and when all these values are zero, the system is in the equilibrium configuration.

In case of small displacements of the nuclei from their equilibrium positions, the potential-energy function expressed through the Cartesian displacement coordinates can be expand in a Taylor series, namely

$$V(\boldsymbol{P}) = V(0) + \sum_{i=1}^{3N} \left(\frac{\partial V(\boldsymbol{P})}{\partial P_i} \right)_0 \cdot P_i + \frac{1}{2} \cdot \sum_{i=1}^{3N} \sum_{j=1}^{3N} \left(\frac{\partial^2 V(\boldsymbol{P})}{\partial P_i \partial P_j} \right)_0 \cdot P_i \cdot P_j + \ldots$$

(for details see the book of Atkins and Friedman [42]). The first term from the right-hand member of this equation being the value of the potential energy at the minimum can be set to zero. The second term disappears as well because the slope of the potential-energy curve at the minimum along each coordinate P_i is zero. Neglect-

ing all terms of the third and higher orders (which are not shown in the equation), just the second-order term remains. Thus, the potential energy takes the form

$$V(\boldsymbol{P}) = \sum_{i=1}^{3N} \sum_{j=1}^{3N} \frac{f_{ij} \cdot P_i \cdot P_j}{2}, \tag{1.33}$$

where

$$f_{ij} = \left(\frac{\partial^2 V(\boldsymbol{P})}{\partial P_i \partial P_j} \right)_0$$

is the *generalized force constant*; eqn. 1.33 is known as the *harmonic approximation* to the potential energy. The kinetic energy can be expressed as

$$T_v(\boldsymbol{P}) = \sum_{i=1}^{3N} \frac{M_i \cdot \dot{P}_i^{\,2}}{2}, \tag{1.34}$$

where M_i is a function of the nuclear masses, and the dot indicates a derivative with respect to time. Consequently, the total energy is

$$E_v = \sum_{i=1}^{3N} \frac{M_i \cdot \dot{P}_i^{\,2}}{2} + \sum_{i=1}^{3N} \sum_{j=1}^{3N} \frac{f_{ij} \cdot P_i \cdot P_j}{2}.$$

As we can see, this expression contains cross terms caused by the function of the potential energy; this fact reflects the statement that by using the Cartesian displacement coordinates the vibrations cannot be considered independently.

However, when the normal coordinates are used, the harmonic approximation to the potential energy can be written in form of a sum of partial potential energies, namely

$$V(\boldsymbol{Q}) = \sum_{k=1}^{K} \frac{f_k \cdot Q_k^2}{2} = \sum_{k=1}^{K} V(Q_k). \tag{1.35}$$

If we present the kinetic energy in the analogous form

$$T_v(\boldsymbol{Q}) = \sum_{k=1}^{K} \frac{M_k \cdot \dot{Q}_k^{\,2}}{2} = \sum_{k=1}^{K} T_{v_k}(Q_k), \tag{1.36}$$

the total-energy function can be written as

$$E_v = \sum_{k=1}^{K} E_{v_k}, \tag{1.37}$$

with

$$E_{v_k} = \frac{M_k \cdot \dot{Q}_k^{\,2}}{2} + \frac{f_k \cdot Q_k^2}{2} = T_{v_k}(Q_k) + V(Q_k).$$

Thus, the potential-energy as well as the total-energy functions expressed through the normal coordinates do not contain any cross terms. Note that the quantities f_k and M_k used in eqns. 1.35 and 1.36 are not identical to the quantities f_{ij} and M_i from eqns. 1.33 and 1.34.

The vibrational quantum number v_k used here labels the vibrational states in the corresponding normal mode of vibrations. The vibrational number v included as a subscript in the designation of such magnitudes as $T_v(\boldsymbol{Q})$ and E_v (as well as $\Psi_v(\boldsymbol{Q})$, see below) has to be interpreted as containing all vibrational numbers v_k simultaneously, *i.e.* $v = (v_1 v_2 \dots v_K)$; the same rule is also valid in this thesis for other quantities marked with v.

The Hamiltonian for the nuclear motion corresponding to the total energy expressed in the form of eqn. 1.37 can be written as the sum

$$\mathcal{H}^n = \sum_{k=1}^{K} \mathcal{H}_k^n,$$

where the Hamiltonian $\mathcal{H}_k^n$ describes one normal mode of vibrations. As a consequence, the vibrational wave function can be presented as a product of the partial vibrational wave functions, *i.e.*

$$\Psi_v(\boldsymbol{Q}) = \prod_{k=1}^{K} \Psi_{v_k}(Q_k).$$

In this case, the overlap integral given by eqn. 1.28 and defining the Franck-Condon factor can also be expressed as a product of the overlap integrals taken for each normal mode of vibrations separately. Thus, the Franck-Condon factor for a multidimensional analysis is

$$F_{v'v} = \prod_{k=1}^{K} \langle v_k | v_k' \rangle. \tag{1.38}$$

Morse potential applied to polyatomic molecule

In spite of the fact that the normal coordinates are introduced by the assumption of the harmonic approximation, in the present study we approach every partial potential energy $V(Q_k)$ by a Morse potential, see eqn. 1.9, which describes the anharmonic oscillator. Thus, in accordance with eqn. 1.35, the potential energy of a molecule (or an ion, $N \geqslant 2$) is used in the form

$$V(\boldsymbol{Q}) = E_e + \sum_{k=1}^{K} D_{ek} \cdot \left(1 - e^{-a_k \cdot (Q_k - Q_{ek})}\right)^2. \tag{1.39}$$

The corresponding total energy, see eqn. 1.11, is expressed in this case as

$$E_v = E_e + \sum_{k=1}^{K} \left(\hbar\omega_k \cdot \left(v_k + \frac{1}{2} \right) - x_k \hbar\omega_k \cdot \left(v_k + \frac{1}{2} \right)^2 \right). \tag{1.40}$$

The quantities in these equations were already discussed in Section 1.2; the subscript k included in their designations indicates the corresponding normal mode of vibrations. The values Q_{ek} presented here are equilibrium values of the corresponding normal coordinates; the full set of these values $\boldsymbol{Q}_e = (Q_{e1}, Q_{e2}, \ldots, Q_{eK})$ gives the equilibrium geometry of the molecule, *i.e.* $V(\boldsymbol{Q}_e) = E_e$. Thus, a full description of the potential energy of the molecule is given by the following Morse parameters:

- ▷ equilibrium values of the normal coordinates $Q_{e1}, Q_{e2}, \ldots, Q_{eK}$;
- ▷ vibrational energies $\hbar\omega_1, \hbar\omega_2, \ldots, \hbar\omega_K$;
- ▷ anharmonicities $x_1\hbar\omega_1, x_2\hbar\omega_2, \ldots, x_K\hbar\omega_K$;
- ▷ energy position of the minimum E_e.

Multidimensional Franck-Condon analysis

In the previous section, the Franck-Condon analysis for the case of a diatomic molecule was discussed: it was shown that the potential-energy curve for the electronic final state can be derived using the potential-energy curve for the electronic initial state by matching the calculated curve to the data points, see page 18. In case of a polyatomic molecule, the potential-energy surface for the electronic final state can be found, namely the potential-energy curves along different normal coordinates (since the normal vibrations are observed in the spectra). Thus, assuming a Morse potential and calculating the Franck-Condon factor in accordance with eqn. 1.38, the changes of the equilibrium values of the normal coordinates upon an electronic transition $\Delta Q_{ek\varepsilon'\varepsilon} = Q_{ek\varepsilon} - Q_{ek\varepsilon'}$ as well as the vibrational energies $\hbar\omega_{k\varepsilon}$ and the anharmonicities $x_{k\varepsilon}\hbar\omega_{k\varepsilon}$ for the electronic final state can be obtained.

Transformation of coordinates

The equilibrium geometry of an electronic state is usually expressed in the space of the real coordinates, namely by the *equilibrium distances* R_{ei} and the *equilibrium angles* α_{ej}. From the Franck-Condon analysis, however, we obtain the differences in the equilibrium geometries of both electronic states expressed in the space of the normal coordinates, namely by the values $\Delta Q_{ek\varepsilon'\varepsilon}$. Therefore, the equilibrium geometry of the electronic final state can be expressed in the equilibrium distances $R_{ei\varepsilon}$ and the equilibrium angles $\alpha_{ej\varepsilon}$ only if we know the corresponding values for

the electronic initial state as well as the transformation of the normal coordinates to the real ones. To derive the equation for such a transformation, let us describe the vibrations in a molecule as the normal vibrations (for details on the algorithm presented here and on the used definitions, see the book of Colthup *et al.* [43] as well as the book of Wilson *et al.* [44]).

At the beginning, let us present the Cartesian displacement coordinates in the matrix form

$$\mathbf{P} = \begin{bmatrix} P_1 \\ P_2 \\ \dots \\ P_{3N} \end{bmatrix}$$

and introduce new coordinates $\boldsymbol{S} = (S_1, S_2, \dots, S_K)$ describing the internuclear distances and the interbond angles. In order to consider the vibrations in a more convenient way, we describe the internuclear distances and the interbond angles in a relative scale, *i.e.* the coordinates S_k represent deflections of the distances and the angles from their equilibrium values. Such coordinates are called the *internal coordinates* and we use them in the matrix form

$$\mathbf{S} = \begin{bmatrix} S_1 \\ S_2 \\ \dots \\ S_K \end{bmatrix}.$$

The number of independent internal coordinates is identical to the number of normal coordinates (for linear molecules as studied in this work), *i.e.* $K = 3N - 6$. So, for instance, a triatomic molecule A−B−C, linear as well as non-linear, have three internal coordinates: two *bond stretching* coordinates $S_1 = R(\mathrm{A{-}B}) - R_e(\mathrm{A{-}B})$ and $S_2 = R(\mathrm{B{-}C}) - R_e(\mathrm{B{-}C})$, and one *bond angle bending* coordinate $S_3 = \alpha(\angle\mathrm{ABC}) - \alpha_e(\angle\mathrm{ABC})$. As in case of the Cartesian displacement coordinates, all internal coordinates possess zero values in the equilibrium configuration.

The internal coordinates can be expressed through the Cartesian displacement coordinates by the equations

$$\begin{aligned} S_1 &= B_{11} \cdot P_1 + B_{12} \cdot P_2 + \ldots + B_{1\,3N} \cdot P_{3N}, \\ S_2 &= B_{21} \cdot P_1 + B_{22} \cdot P_2 + \ldots + B_{2\,3N} \cdot P_{3N}, \\ &\dots, \\ S_K &= B_{K1} \cdot P_1 + B_{K2} \cdot P_2 + \ldots + B_{K\,3N} \cdot P_{3N}. \end{aligned} \tag{1.41}$$

This set of equations can be presented in a matrix description as

$$\mathbf{S} = \mathbf{B} \cdot \mathbf{P}, \tag{1.42}$$

where

$$\mathbf{B} = \begin{bmatrix} B_{11} & B_{12} & \cdots & B_{1\,3N} \\ B_{21} & B_{22} & \cdots & B_{2\,3N} \\ \cdots & \cdots & \cdots & \cdots \\ B_{K1} & B_{K2} & \cdots & B_{K\,3N} \end{bmatrix}$$

is a K-by-$3N$ matrix of the coefficients.

Let us now define two matrices describing properties of the considered molecule: the **M** matrix, which describes the nuclei, and the **F** matrix, which describes the bonds interacting between the nuclei. The **M** matrix is defined as a $3N$-by-$3N$ diagonal matrix with the nuclear masses M_1, M_2, ..., M_N arranged on the diagonal in the following way:

$$\mathbf{M} = \begin{bmatrix} M_1 & 0 & 0 & 0 & 0 & 0 & \cdots & 0 & 0 & 0 \\ 0 & M_1 & 0 & 0 & 0 & 0 & \cdots & 0 & 0 & 0 \\ 0 & 0 & M_1 & 0 & 0 & 0 & \cdots & 0 & 0 & 0 \\ 0 & 0 & 0 & M_2 & 0 & 0 & \cdots & 0 & 0 & 0 \\ 0 & 0 & 0 & 0 & M_2 & 0 & \cdots & 0 & 0 & 0 \\ 0 & 0 & 0 & 0 & 0 & M_2 & \cdots & 0 & 0 & 0 \\ \cdots & \cdots & \cdots & \cdots & \cdots & \cdots & \cdots & \cdots & \cdots & \cdots \\ 0 & 0 & 0 & 0 & 0 & 0 & \cdots & M_N & 0 & 0 \\ 0 & 0 & 0 & 0 & 0 & 0 & \cdots & 0 & M_N & 0 \\ 0 & 0 & 0 & 0 & 0 & 0 & \cdots & 0 & 0 & M_N \end{bmatrix}. \tag{1.43}$$

The **F** matrix is a symmetric K-by-K matrix containing the force constants F_{ij}, namely

$$\mathbf{F} = \begin{bmatrix} F_{11} & F_{12} & \cdots & F_{1K} \\ F_{12} & F_{22} & \cdots & F_{2K} \\ \cdots & \cdots & \cdots & \cdots \\ F_{1K} & F_{2K} & \cdots & F_{KK} \end{bmatrix}. \tag{1.44}$$

Assuming harmonic vibrations, see eqn. 1.33, the potential and the kinetic energies of the molecule caused by the nuclear motion can be presented through the internal coordinates S as

$$V(S) = \frac{1}{2} \cdot \mathbf{S}^{\mathrm{T}} \cdot \mathbf{F} \cdot \mathbf{S} \tag{1.45}$$

and

$$T_v(S) = \frac{1}{2} \cdot \dot{\mathbf{S}}^{\mathrm{T}} \cdot \mathbf{G}^{-1} \cdot \dot{\mathbf{S}}, \tag{1.46}$$

respectively, see the works of Wilson [45, 46]. Here the signs "T" and "-1" designate the transposed and the inverse matrices, respectively, $\dot{\mathbf{S}}$ is the **S** matrix, with all

elements being derivatives with respect to time, and **G** is a K-by-K matrix defined as

$$\mathbf{G} = \mathbf{B} \cdot \mathbf{M}^{-1} \cdot \mathbf{B}^{\mathrm{T}}. \tag{1.47}$$

Therefore, Newton's equation of motion in the Lagrange form can be written for the i^{th} internal coordinate ($i = 1, 2, \ldots, K$) as

$$\frac{d}{dt}\left(\frac{\partial}{\partial \dot{S}_i} T_v(\boldsymbol{S})\right) + \frac{\partial}{\partial S_i} V(\boldsymbol{S}) = 0. \tag{1.48}$$

The general solution of eqn. 1.48 with the energies given by eqns. 1.45 and 1.46 represents the internal coordinate

$$S_i(t) = \sum_{k=1}^{K} L_{ik} \cdot Q_k(t), \tag{1.49}$$

where

$$Q_k(t) = A_k \cdot \sin\left(\sqrt{\lambda_k} \cdot t + \varphi_k\right).$$

The last expression describes the k^{th} normal vibration, namely a harmonic motion of the k^{th} normal coordinate with the amplitude A_k, the frequency $\sqrt{\lambda_k}$, and the initial phase φ_k. As we can see from the first expression, a vibration of each internal coordinate is influenced by all normal vibrations. So, when only one normal vibration is excited, all internal coordinates oscillate about their equilibrium positions at the same frequency, in the same phase, but with different amplitudes: the amplitude of oscillation of the internal coordinate S_i by the k^{th} normal vibration is designated in eqn. 1.49 as L_{ik}.

After substitution of the internal coordinate given by eqn. 1.49 into eqn. 1.48, we can unite all Lagrange equations and present them in the matrix form

$$\mathbf{H} \cdot \mathbf{L}_k = \lambda_k \cdot \mathbf{L}_k, \tag{1.50}$$

where **H** is a K-by-K matrix defined as

$$\mathbf{H} = \mathbf{G} \cdot \mathbf{F}, \tag{1.51}$$

and $\mathbf{L}_k$ is a column matrix of amplitudes corresponding to the k^{th} normal vibration, *i.e.*

$$\mathbf{L}_k = \begin{bmatrix} L_{1k} \\ L_{2k} \\ \cdots \\ L_{Kk} \end{bmatrix}.$$

Equation 1.50 is called the *secular equation* and can be solved in terms of eigenvalues and eigenvectors. This means that this equation has K solutions ($k = 1, 2, \ldots,$

K) consisting of the eigenvalue λ_k and the eigenvector $\mathbf{L}_k$ each. Moreover, while each λ_k is determined as an exact number, each $\mathbf{L}_k$ matrix is not normalized. Thus, the vibrational motions of the molecule are fully described by K normal vibrations, each having the frequency $\sqrt{\lambda_k}$ and the form defined by the $\mathbf{L}_k$ matrix. To obtain the matrices $\mathbf{L}_k$ in the form required for establishing the relation between the normal and the internal coordinates, each of the matrices has to be multiplied by the normalization factor

$$N_k = \sqrt{\frac{\lambda_k}{\sum_{i=1}^{K}\sum_{j=1}^{K} F_{ij} \cdot L_{ik} \cdot L_{jk}}}. \tag{1.52}$$

In the following each $\mathbf{L}_k$ matrix is used only in its normalized form.

The masses in the $\mathbf{M}$ matrix are usually expressed in unified atomic mass units, u, while the force constants in the $\mathbf{F}$ matrix, which are associated with the bond stretching internal coordinates, are expressed in millidynes per angstrom, $\frac{\text{mdyn}}{\text{Å}}$. As a consequence, the parameter λ_k becomes expressed in millidynes per angstrom times unified atomic mass unit, $\frac{\text{mdyn}}{\text{Å}\cdot\text{u}}$. Therefore, in order to convert the frequency $\sqrt{\lambda_k}$ with λ_k expressed in $\frac{\text{mdyn}}{\text{Å}\cdot\text{u}}$ into the frequency expressed in meV, the following relation has to be applied:

$$\hbar\omega_k\,[\text{meV}] = 161.4 \cdot \sqrt{\lambda_k \left[\frac{\text{mdyn}}{\text{Å}\cdot\text{u}}\right]}. \tag{1.53}$$

Using this expression, we can compare the calculated frequency $\sqrt{\lambda_k}$ with the experimental vibrational energy $\hbar\omega_k$. The normal coordinates Q_k are expressed in angstroms times square root of unified atomic mass unit, $\text{Å}\cdot\text{u}^{1/2}$, and the amplitudes L_{ik} in reciprocals of square root of unified atomic mass unit, $\text{u}^{-1/2}$. For internal coordinates consisting of bond angles, the treatment is different. Since such internal coordinates are not applied in the present work, we do not discuss the quantities associated with these coordinates; for details, see the literature [43, 44].

Let us now unite all K matrices $\mathbf{L}_k$ in the total K-by-K $\mathbf{L}$ matrix, *i.e.*

$$\mathbf{L} = \begin{bmatrix} L_{11} & L_{12} & \cdots & L_{1K} \\ L_{21} & L_{22} & \cdots & L_{2K} \\ \cdots & \cdots & \cdots & \cdots \\ L_{K1} & L_{K2} & \cdots & L_{KK} \end{bmatrix}$$

and represent the normal coordinates $\boldsymbol{Q} = (Q_1, Q_2, \ldots, Q_K)$ as the column matrix

$$\mathbf{Q} = \begin{bmatrix} Q_1 \\ Q_2 \\ \cdots \\ Q_K \end{bmatrix}.$$

Thus, the set of relations given by eqn. 1.49 can be presented in matrix form as

$$\mathbf{S} = \mathbf{L} \cdot \mathbf{Q}.$$

This equation can be rewritten in the relative form applied to the equilibrium values of the normal and the internal coordinates, *i.e.* we can relate the changes of the equilibrium values of the normal coordinates upon electronic transitions $\Delta Q_{e k \varepsilon' \varepsilon}$ with the changes of the equilibrium distances $\Delta R_{e i \varepsilon' \varepsilon}$. This formula is

$$\begin{bmatrix} \Delta R_{e1\varepsilon'\varepsilon} \\ \Delta R_{e2\varepsilon'\varepsilon} \\ \cdots \\ \Delta R_{eK\varepsilon'\varepsilon} \end{bmatrix} = \begin{bmatrix} L_{11} & L_{12} & \cdots & L_{1K} \\ L_{21} & L_{22} & \cdots & L_{2K} \\ \cdots & \cdots & \cdots & \cdots \\ L_{K1} & L_{K2} & \cdots & L_{KK} \end{bmatrix} \cdot \begin{bmatrix} \Delta Q_{e1\varepsilon'\varepsilon} \\ \Delta Q_{e2\varepsilon'\varepsilon} \\ \cdots \\ \Delta Q_{eK\varepsilon'\varepsilon} \end{bmatrix}. \tag{1.54}$$

This relation is used in the present work for the transformation of the values $\Delta Q_{e k \varepsilon' \varepsilon}$ derived from Franck-Condon analysis to changes of the equilibrium distances $\Delta R_{e i \varepsilon' \varepsilon}$.

By the construction of the transformation relation 1.54 it is assumed that the **L** matrix is the same for both the electronic initial state ε' and the electronic final state ε. However, in a case of more than one normal mode of vibrations with the same symmetry, different force constants in the electronic states result in different **L** matrices. This is relevant, for example, for the OCS molecule studied in this work. To overcome this difficulty, we calculate the **L** matrix for different electronic states (using different force constants) and derive from these results an average **L** matrix with error bars based on the variations, see page 73. For the molecules NO and CO_2, the calculated **L** matrix for the considered normal modes of vibrations is identical for all electronic states, see Appendix B.

Thus, one can see that the problem of transformation of the coordinates comes to a calculation of the **L** matrix. Examples of the calculation of the **L** matrices for the neutral OCS as well as NO and CO_2 molecules, in accordance with the algorithm presented in this section, are presented in Appendix B.

1.6 Designations of electronic states

In order to designate the electronic states of the molecules discussed in Chapter 3, two different notations are used. These notations are specified in the present section.

The first notation is appropriate to designate all electronic states of a molecule (or an ion) having the *cylindrical symmetry*, *i.e.* of a linear molecule such as those studied in this work, and is defined by the scheme

$$^{2S+1}\Lambda_{\Omega}.$$

Here Λ is the *magnetic orbital quantum number* of the electronic state, S is the *spin quantum number*, and Ω is the *magnetic total-angular-momentum quantum number*. The last describes states split by *spin-orbit interaction* and is defined as

$$\Omega = \Lambda + \Sigma,$$

where Σ is the *magnetic spin quantum number* of the state (for details of these quantum numbers see the book of Atkins and Friedman [47]).

The magnetic orbital quantum number is being written through its letter designation in accordance with the rule

Λ	0	1	2	3	...
designation	Σ	Π	Δ	Φ	...

.

For a molecule with the *inversion symmetry*, like CO_2, these letters are used with the subscript "g" or "u" denoting the even ("gerade") or the odd ("ungerade") character of the electronic wave function. The letter "Σ" is always written with the sign "+" or "–" as a superscript indicating a behavior of the wave function by its reflection relative to a plane passing through the intermolecular axis. Since for singlet states ($S = 0$) the quantum number Ω can have only one value, and for most of non-singlet states ($S > 0$) a degeneracy of electronic states with different numbers Ω is observed, this quantum number is omitted in notations of the majority of electronic states. In order to distinguish electronic states of a molecule having the same notation, in front of the notation an additional number or letter can be put. As examples the following electronic states can be presented: the states $X^2\Pi_{1/2}$ and $X^2\Pi_{3/2}$ of the ground-state configuration of the NO molecule, the states $a^1\Delta_g$ and $c^1\Sigma_u^-$ of CO_2^{2+}, the states $X^2\Sigma^+$ and $c^4\Pi$ of NO^{2+}, and the states $\tilde{X}^3\Sigma^-$ and $2^3\Pi_2$ of OCS^{2+}.

The second notation is applicable to designate just the core-ionized states and corresponds to the scheme

$$nl^{-1}_{J,\,\Omega}.$$

In this scheme n and l are the *principal quantum number* and the *orbital quantum number*, respectively, describing the almost perfectly atomic-like shell and subshell from which ionization has occurred, and J is the *angular momentum quantum number* of the electronic state. The quantum numbers J and Ω describe states split by spin-orbit interaction and *molecular-field interaction*, respectively.

To present orbital quantum number, its letter designation given by the rule

l	0	1	2	3	...
designation	s	p	d	f	...

is used. The quantum number Ω can be omitted in the presented notation if $J = 1/2$, since in this case Ω can have only one value, namely $1/2$; the quantum number J, in one's turn, can be omitted as well if $l = 0$, since in this case J also can have only the value $1/2$. In front of the notation, a letter specifying the ionized atom within the molecule is usually shown. The latter notation can be used in combination with the former one, for example, to designate the core-ionized states N $1s^{-1}$ $^1\Pi$ and N $1s^{-1}$ $^3\Pi$ of the NO molecule, which are originated from the interaction of the spin moments of the $1s$ and the 2π electrons. As other examples of an application of the latter notation the following states can be presented: the C $1s^{-1}$ core-ionized state of the CO_2 molecule as well as the S $2p_{1/2}^{-1}$ and the S $2p_{3/2,1/2}^{-1}$ core-ionized states of the OCS molecule.

1.7 Lifetime interference

From Section 1.4 we know how the vibrational progression of an electronic transition can be described with a fit analysis using Franck-Condon factors. The vibrational progression constructed in such an analysis is presented in the upper right corner of Figure 1.4. As we can see, the widths of lines forming this vibrational progression are neglected. In the following, we present the formulas for the fitting curves that take into account the linewidths caused by lifetime broadening of the intermediate states, see Figure 1.3, and which describe all electronic transitions between stable or metastable electronic states of a spectrum.

The photoelectron spectrum can be described with a sum of Lorentzian functions, see eqn. 1.24, namely

$$I_g^{ph}(T) \propto \sum_i \frac{\Gamma_i}{2\pi} \cdot \frac{|\langle i|\boldsymbol{\mathcal{D}}|g\rangle|^2}{\left(T - T_{gi}^{ph}\right)^2 + \left(\frac{\Gamma_i}{2}\right)^2}, \tag{1.55}$$

while for the Auger spectrum the situation is different. The reason is that a splitting between the intermediate states can be comparable to the lifetime broadening. In this case, the different lines in the photoelectron spectrum overlap so that the exact intermediate state through which the Auger decay occurs cannot be determined. This leads to a situation where the Auger spectrum cannot be described by Lorentzian profiles only. By analogy with Young's double-slit experiment, where an interference pattern is observed when the exact path of an individual photon is not known, one can conclude that some interference effect has to be present in the Auger spectrum; this effect is called the *lifetime interference* (LTI). The corresponding formula for the Auger spectrum is reported by Correia *et al.* [48] and can be

presented as

$$I_g^A(T) \propto \sum_f \left| \sum_i \sqrt{\frac{\Gamma_i}{2\pi}} \cdot \frac{\langle i|\boldsymbol{\mathcal{D}}|g\rangle \cdot \langle f|\mathcal{C}|i\rangle}{T - T_{if}^A + \iota \cdot \frac{\Gamma_i}{2}} \right|^2, \tag{1.56}$$

where ι is the imaginary unit. The square moduli of the matrix elements $\langle i|\boldsymbol{\mathcal{D}}|g\rangle$ and $\langle f|\mathcal{C}|i\rangle$ represent the probabilities of the transitions $g \to i$ and $i \to f$, respectively, see Section 1.4. The product of the matrix elements included in the last equation is used to calculate the probability of the transition from the ground state g to the final state f through the intermediate state i. The photoelectron kinetic energy T_{gi}^{ph} and the Auger-electron kinetic energy T_{if}^A are defined by eqns. 1.17 and 1.18, respectively; the lifetime width Γ_i is defined by eqn. 1.25.

In the present study, we assume that the lifetime width Γ_i dominated by the Auger decay is identical for all vibrational substates v' of one electronic intermediate state ε'. This assumption is reasonable, since no evidence for the opposite is reported in the literature. Moreover, the lifetimes of the final states are assumed to be long as compared to those of the intermediate states. Therefore, in the following we use $\Gamma_{\varepsilon'}$ instead of Γ_i.

Let us consider eqn. 1.56 in detail. Using the matrix elements $\langle i|\boldsymbol{\mathcal{D}}|g\rangle$ and $\langle f|\mathcal{C}|i\rangle$ in the form of eqns. 1.29 and 1.31, respectively, $I_g^A(T)$ splits into the four components, *i.e.*

$$I_g^A(T) \propto I_g^{A1}(T) + I_g^{A2}(T) + I_g^{A3}(T) + I_g^{A4}(T), \tag{1.57}$$

where

$$I_g^{A1}(T) = \sum_\varepsilon \sum_v \sum_{\varepsilon'} \sum_{v'} |\boldsymbol{D}_{\varepsilon''\varepsilon'}|^2 \cdot |C_{\varepsilon'\varepsilon}|^2 \cdot |F_{v''v'}^{ph}|^2 \cdot |F_{v'v}^A|^2 \times \frac{\Gamma_{\varepsilon'}}{2\pi} \cdot \frac{1}{\left(T - T_{\varepsilon' v' \varepsilon v}^A\right)^2 + \left(\frac{\Gamma_{\varepsilon'}}{2}\right)^2},$$

$$I_g^{A2}(T) = \sum_\varepsilon \sum_v \sum_{\varepsilon'} \sum_{b' \neq v'} |\boldsymbol{D}_{\varepsilon''\varepsilon'}|^2 \cdot |C_{\varepsilon'\varepsilon}|^2 \cdot F_{v''v'}^{ph} \cdot F_{v'v}^A \cdot F_{b'v''}^{ph} \cdot F_{vb'}^A \times \frac{\Gamma_{\varepsilon'}}{2\pi} \cdot \frac{\left(T - T_{\varepsilon' v' \varepsilon v}^A\right) \cdot \left(T - T_{\varepsilon' b' \varepsilon v}^A\right) + \left(\frac{\Gamma_{\varepsilon'}}{2}\right)^2}{\left(\left(T - T_{\varepsilon' v' \varepsilon v}^A\right) \cdot \left(T - T_{\varepsilon' b' \varepsilon v}^A\right) + \left(\frac{\Gamma_{\varepsilon'}}{2}\right)^2\right)^2 + (E_{\varepsilon' v'} - E_{\varepsilon' b'})^2 \cdot \left(\frac{\Gamma_{\varepsilon'}}{2}\right)^2},$$

$$I_g^{A3}(T) = \sum_\varepsilon \sum_v \sum_{a' \neq \varepsilon'} \sum_{v'} \boldsymbol{D}_{\varepsilon''\varepsilon'} \cdot \boldsymbol{D}_{\varepsilon''a'}^* \cdot C_{\varepsilon'\varepsilon} \cdot C_{a'\varepsilon}^* \cdot |F_{v''v'}^{ph}|^2 \cdot |F_{v'v}^A|^2 \times \frac{\sqrt{\Gamma_{\varepsilon'} \cdot \Gamma_{a'}}}{2\pi} \cdot \frac{\left(T - T_{\varepsilon' v' \varepsilon v}^A\right) \cdot \left(T - T_{a' v' \varepsilon v}^A\right) + \frac{\Gamma_{\varepsilon'}}{2} \cdot \frac{\Gamma_{a'}}{2}}{\left(\left(T - T_{\varepsilon' v' \varepsilon v}^A\right) \cdot \left(T - T_{a' v' \varepsilon v}^A\right) + \frac{\Gamma_{\varepsilon'}}{2} \cdot \frac{\Gamma_{a'}}{2}\right)^2 + (E_{\varepsilon' v'} - E_{a' v'})^2 \cdot \frac{\Gamma_{\varepsilon'}}{2} \cdot \frac{\Gamma_{a'}}{2}},$$

and

$$I_g^{A4}(T) = \sum_{\varepsilon}\sum_{v}\sum_{a'\neq\varepsilon'}\sum_{b'\neq v'} \boldsymbol{D}_{\varepsilon''\varepsilon'}\cdot\boldsymbol{D}^{*}_{\varepsilon''a'}\cdot C_{\varepsilon'\varepsilon}\cdot C^{*}_{a'\varepsilon}\cdot F^{ph}_{v''v'}\cdot F^{A}_{v'v}\cdot F^{ph}_{b'v''}\cdot F^{A}_{vb'} \times \frac{\sqrt{\Gamma_{\varepsilon'}\cdot\Gamma_{a'}}}{2\pi}\cdot \frac{\left(T-T^{A}_{\varepsilon'v'\varepsilon v}\right)\cdot\left(T-T^{A}_{a'b'\varepsilon v}\right)+\frac{\Gamma_{\varepsilon'}}{2}\cdot\frac{\Gamma_{a'}}{2}}{\left(\left(T-T^{A}_{\varepsilon'v'\varepsilon v}\right)\cdot\left(T-T^{A}_{a'b'\varepsilon v}\right)+\frac{\Gamma_{\varepsilon'}}{2}\cdot\frac{\Gamma_{a'}}{2}\right)^{2}+\left(E_{\varepsilon'v'}-E_{a'b'}\right)^{2}\cdot\frac{\Gamma_{\varepsilon'}}{2}\cdot\frac{\Gamma_{a'}}{2}}.$$

The component $I_g^{A1}(T)$ describes the direct terms, which are sufficient when the photoionization process and the Auger decay are considered independently, *i.e.* within a *two-step model*. In this case, the overlap of the different lines in the photoelectron spectrum and, as a consequence, the lifetime interference, are neglected. If we compare the expressions for these terms with eqn. 1.24, we can see that the lines have Lorentzian profiles (like the lines of the terms in eqn. 1.55 describing the photoelectron spectrum). The components $I_g^{A2}(T)$, $I_g^{A3}(T)$, and $I_g^{A4}(T)$ describe the indirect terms, which are relevant when the photoionization process and the Auger decay are considered as subsequent steps of one process, *i.e.* within a *one-step model*. They result from the fact that the overlapping lines in the photoelectron spectrum do not allow to determine the intermediate state exactly and, therefore, the lifetime interference is present. So, the terms of the component $I_g^{A2}(T)$ are caused by the different vibrational levels b' and v' belonging to the same electronic state ε'. The component $I_g^{A3}(T)$ describes the terms caused by the vibrational substates with the same vibrational quantum number v' of the different electronic states a' and ε'. And, finally, the terms forming the component $I_g^{A4}(T)$ are caused by the vibrational levels with the different vibrational quantum numbers b' and v' belonging to the different electronic states a' and ε'. Such a description in accordance with the one-step model is used in the present analysis.

Thus, we can see that the lifetime interference is formed by the *vibrational lifetime interference*, the *electronic-state lifetime interference*, and the *mixed lifetime interference*, which are described with the terms of the components $I_g^{A2}(T)$, $I_g^{A3}(T)$, and $I_g^{A4}(T)$, respectively. From the formulas of these terms it can be shown that their contribution to the total intensity $I_g^{A}(T)$ strongly depends on the overlap of the Lorentzian profiles in the photoelectron spectrum. So, the larger lifetime widths $\Gamma_{\varepsilon'}$ and the closer the levels of the intermediate states, the larger contribution of the indirect terms.

Püttner *et al.* [13, 14, 16] have shown that the contributions of the components $I_g^{A3}(T)$ and $I_g^{A4}(T)$ to the total intensity $I_g^{A}(T)$, given by eqn. 1.57, are normally very small. In the following, we give the main ideas of their argumentations. For this it is important that an *Auger final state* consists of the final state $e\Lambda$, the photoelectron $\epsilon\lambda'$, and the Auger electron $\epsilon\lambda''$, *i.e.* $|e\Lambda\epsilon\lambda'\epsilon\lambda''\rangle$. Here Λ, λ', and λ'' describe the symmetries of the final state, the photoelectron, and the Auger electron, respectively. In the present cases of linear molecules, these values are equivalent to the

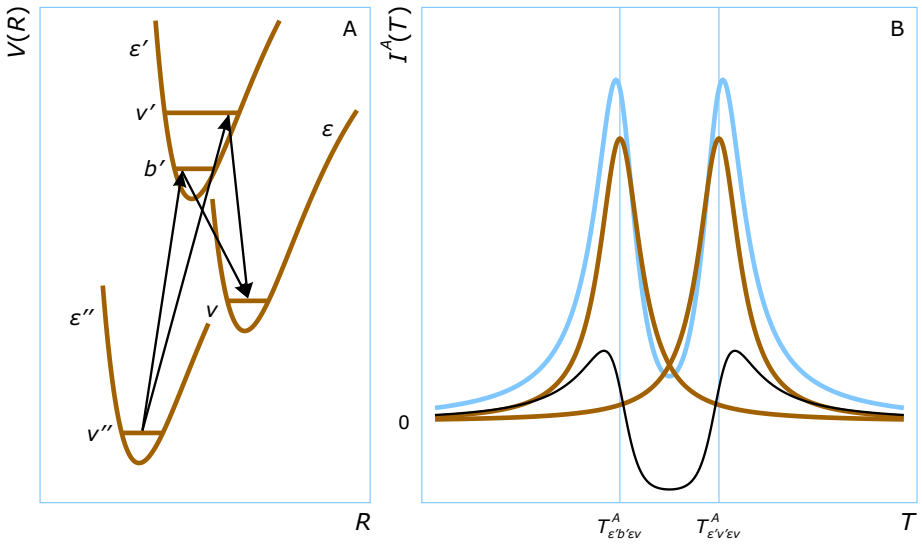

Figure 1.5: Scheme of the entire process in the simplest case (frame A) and the respective Auger spectrum (frame B). In the spectrum (frame B) the total Auger intensity (blue line) represents a sum of the direct terms (brown lines) and the vibrational lifetime-interference term (black line). For a description of the lines in the scheme of the process (frame A) see Figure 1.1.

angular momentum along the molecular axis. The electronic-state lifetime interference as well as the mixed lifetime interference can only occur when a given final state $|e''\Lambda''\epsilon'\lambda'\epsilon''\lambda''\rangle$ is populated through two different intermediate states, which consist of core hole $e'\Lambda'$ and the photoelectron $\epsilon'\lambda'$, *i.e.* $|e'\Lambda'\epsilon'\lambda'\rangle$. Now the selection rules for the photoionization process lead to different symmetries λ' for the photoelectron if Λ' of the core-ionized state is different so that no electronic-state lifetime interferences and no mixed lifetime interferences can occur.

The present argumentation is based on the assumption that Λ' is a good quantum number for the core-ionized state. This is, however, not the case for $2p^{-1}$ core holes, *i.e.* they have to be described as a linear combination of different states $|e'\Lambda'\epsilon'\lambda'\rangle$. However, in all cases, the $2p^{-1}$ core-ionized states are dominated by one state $|e'\Lambda\epsilon'\lambda'\rangle$ so that only the parts of two intermediate states $2p^{-1}$ with the same state $|e'\Lambda'\epsilon'\lambda'\rangle$ can interfere.

As a result of these facts, the components $I_g^{A3}(T)$ and $I_g^{A4}(T)$ are neglected in the present fit analysis and only the direct terms and the vibrational lifetime-interference terms are taken into account. Thus, the formula for the fitting curve of the Auger spectrum is used in the form

$$I_g^A(T) \propto I_g^{A1}(T) + I_g^{A2}(T). \tag{1.58}$$

A graphical expression of the discussed lifetime-interference effect is presented

in Figure 1.5. In this figure, the simplest case is presented (frame A), when only two ways from the ground state $\varepsilon''v''$ to the final state εv are taken into account, namely through the intermediate states $\varepsilon'b'$ and $\varepsilon'v'$. As a result of these transitions, the total Auger spectrum (frame B) represents a sum of three curves: two of them correspond to the direct terms forming the component $I_g^{A1}(T)$, and the remaining one to the vibrational lifetime-interference term forming the component $I_g^{A2}(T)$. As seen from the figure, the graphs of the direct terms have a Lorentzian profile, see Figure 1.3, and are shifted from each other by the value of $(T^A_{\varepsilon'v'\varepsilon v} - T^A_{\varepsilon'b'\varepsilon v})$ equal to $(E'_{\varepsilon'v'} - E'_{\varepsilon'b'})$, see eqn. 1.18. In the considered case, the probabilities of the transitions through both intermediate states are assumed to be equal, which is reflected in equal intensities of the Lorentzian lines. The lineshape of the vibrational lifetime-interference term shows its maximal amplitude at an energy position between the maxima of the direct terms.

1.8 Post-collision interaction

As we can see from eqns. 1.17 and 1.18, at a given ionization energy B_{gi}, the photoelectron kinetic energy can vary at the expense of the choice of the photon energy $h\nu$, while the Auger-electron kinetic energy remains unchangeable. In the present work, the choice of the photon energy is caused by the existence of a variety of factors and represents the search for a compromise between them. For example, in order to avoid an influence of a *shape resonance* [49] on the vibrational structure, the photon energy should not be too low. On the other hand, it should not be too high because the experimental resolution of the photoelectron spectrum decreases with increasing photon energy, see Section 2.3, which would masks the vibrational structure rendering a Franck-Condon analysis more complicated, see page 18. Moreover, with increasing photon energy, the *photoionization cross section* [50] decreases. This leads to an increase of the data-acquisition time, which is often not possible under the conditions of limited beamtime at synchrotron-radiation facilities. At high photon energies, the *recoil effect* [51], which influences the vibrational progressions, can be also appreciable. As a result, the photon energies chosen in our experiment were such that the photoelectron is always slower than the Auger electron ejected in the subsequent Auger decay. This leads to *post-collision interaction* (PCI) and changes the lineshape.

In order to understand the post-collision interaction effect, let us consider a classical picture of the motion of the slow photoelectron and the fast Auger electron in the vacuum after their ejections from the molecule, see Figure 1.6. After the absorption of the photon by the neutral molecule (frame A), the photoelectron emission occurs. In the beginning, the photoelectron moves in the electric field of a singly

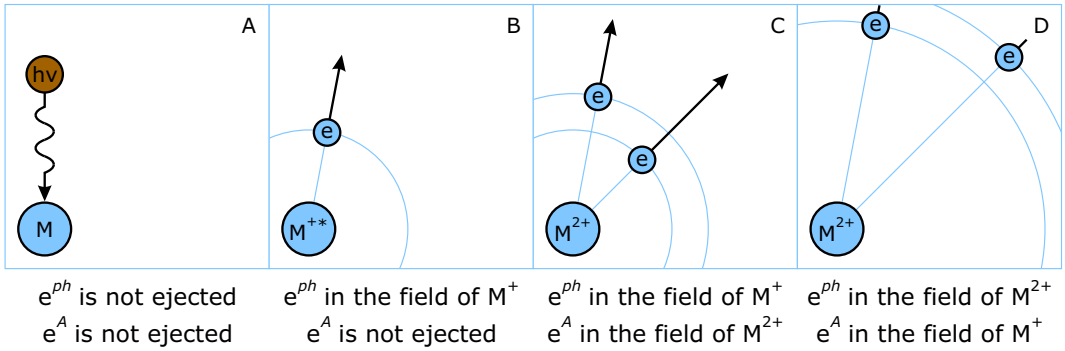

Figure 1.6: Motion in the space of both the photoelectron and the Auger electron ejected from the same molecule. For a description of the frames see text.

charged ion (frame B). With some time delay the Auger electron is emitted creating a doubly charged ion. However, as long as the Auger electron is closer to the ion than the photoelectron, the photoelectron still sees a singly charged ion (frame C). In this time period, the Auger electron moves in the field of the doubly charged ion. However, due to its higher kinetic energy, the Auger electron overtakes the photoelectron at some time. From this moment on it moves in the total field of the singly charged ion, while the photoelectron moves in the total field arising from the doubly charged ion (frame D). Consequently, the electric field seen by the photoelectron and the Auger electron changes not only due to the increasing distance from the field source but also due to the change of the total charge of the source itself. The latter mechanism can be considered as an interaction of the photoelectron and the Auger electron in the space out of the molecule; this interaction is called post-collision interaction.

Equations 1.55 and 1.58 provide the functions describing the spectra without post-collision interaction. However, post-collision interaction leads to a change of the lineshape; we call such a change as the *PCI effect*. In order to take this effect into account, all components defining the intensities $I_g^{ph}(T)$ and $I_g^{A}(T)$ have to be corrected appropriately.

By taking the PCI effect into account, the profiles of the lines corresponding to the direct terms – *i.e.* to the terms forming the intensities $I_g^{ph}(T)$ and $I_g^{A1}(T)$ in eqns. 1.55 and 1.58, respectively – can be described by the function given by Kuchiev and Sheinerman [52]. This function is called the *PCI function*, and we use it in its simplified form given by Armen *et al.* [53]. How the PCI function can be inserted into the terms composing the intensities $I_g^{ph}(T)$ and $I_g^{A1}(T)$ is demonstrated in Appendix A.

Let us present the PCI function and its graph. For the photoelectron spectrum,

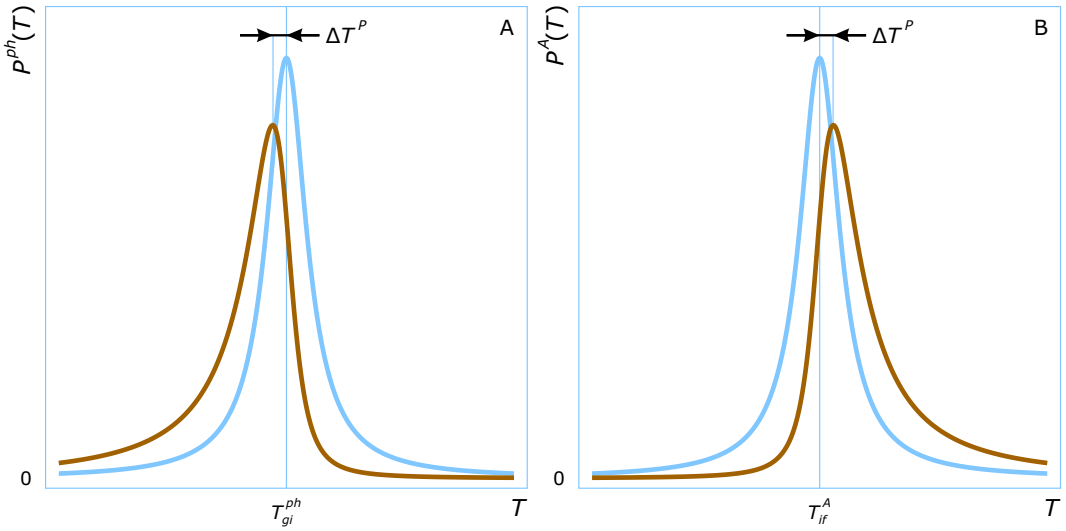

Figure 1.7: Graphs of the PCI functions (brown lines) for both the photoelectron spectrum (frame A) and the Auger spectrum (frame B) presented on kinetic-energy scales. The lines are constructed with the same lifetime width $\Gamma_{\varepsilon'} = 100$ meV and the same kinetic energies $T^{ph}_{gi} = 20$ eV and $T^{A}_{if} = 200$ eV. The corresponding Lorentzian lineshapes, which do not take the PCI effect into account, are also presented for comparison (blue lines).

namely for the transition $g \to i$, the PCI function is defined as

$$P^{ph}_{gif}(T) = \frac{\Gamma_{\varepsilon'}}{2} \cdot \frac{e^{2\xi \cdot \arctan\left(\frac{T - T^{ph}_{gi}}{\frac{\Gamma_{\varepsilon'}}{2}}\right)}}{\left(T - T^{ph}_{gi}\right)^2 - \left(\frac{\Gamma_{\varepsilon'}}{2}\right)^2} \cdot \frac{\xi}{\sinh\left(\pi \cdot \xi\right)}. \tag{1.59}$$

The parameter ξ used here is given by the formula

$$\xi = \frac{\sqrt{\frac{T^{ph}_{gi}}{T^{A}_{if}} - 1}}{\sqrt{2k \cdot T^{ph}_{gi}}}, \tag{1.60}$$

where k is a constant equal to 0.03675 eV^{-1}. The quantities T^{ph}_{gi} and T^{A}_{if} are the kinetic energies of the photoelectron and the Auger electron, respectively. The parameter $\Gamma_{\varepsilon'}$ is the lifetime width of the intermediate state i. The presented function is normalized to unit area under the curve. From eqn. 1.60 it can be seen that the shape of the function depends on the subsequent Auger transition $i \to f$. This fact reflects the influence of the Auger electron on the photoelectron and *vice versa* during their motion in vacuum. The graph of the function is plotted in Figure 1.7

(frame A). The PCI function for the corresponding Auger spectrum $P^A_{gif}(T)$ is defined by the analogous formula and is plotted in the same figure (frame B). The corresponding Lorentzian profiles, which would be expected when the PCI effect is absent, are also shown in the figure for comparison. As we can see, due to the PCI effect, the spectral lines undergo two changes: first, a distortion of the lineshape and second, a shift of the peak ΔT^P, which is called the *PCI shift*, see Figure 1.7. For the photoelectron, this shift leads to lower kinetic energies due to the increasing charge seen by the electron, while it goes to higher kinetic energies for the Auger electron due to a decreasing charge.

The same changes occur with the profiles of the indirect terms, *i.e.* of the terms forming the component $I^{A2}_g(T)$ in eqn. 1.58. However, no functions are available from the literature allowing to describe these profiles by post-collision interaction. Therefore, we describe them with the same function $I^{A2}_g(T)$, but with one correction: we include in this function the PCI shift ΔT^P, which can be obtained by simulations based on eqn. 1.59.

Chapter 2

Experimental technique

In this chapter the experimental techniques that were used to measure the photoelectron and Auger spectra analyzed in the present work are briefly described.

All spectra were measured at synchrotron-radiation facilities that provide intense, polarized, and monochromatic soft X-rays with tunable energy and high resolution for the photoionization process. Such light sources are obtained when synchrotron radiation produced by an undulator passes through the monochromator of a beamline. In Section 2.1, we briefly discuss the radiation employed in our experiments; the monochromators used are described in Section 2.2.

After passing the beamline, the light enters a vacuum chamber where photons interact with the molecules under study. The kinetic energies of the electrons emitted due to the photoionization process and the Auger decay are registered with an electron-energy analyzer. The analyzer possesses high resolution that, together with a high photon-energy resolution, is necessary for a successful fit analysis. The vacuum chamber and the electron-energy analyzer forming an experimental end station are described in Section 2.3.

2.1 Synchrotron radiation

As known from classical electrodynamics, when a moving charged particle enters an electromagnetic field, the field begins to act on the particle with a force called the Lorentz force. As a result, the field bends the trajectory of the particle giving it an acceleration (the centripetal acceleration). From classical electrodynamics we also know that accelerated charged particles, *i.e.* the particles in the electromagnetic field, emit an electromagnetic radiation. The electromagnetic radiation emitted by particles moving at relativistic velocities is called *synchrotron radiation*.

Synchrotron radiation has a number of important properties. At first, it is highly collimated, *i.e.* it radiates in a very narrow cone oriented in the travel direction of the particles. Secondly, synchrotron radiation has a wide range of energies of the emitted photons. Another important property is the polarization of the light: synchrotron radiation is linearly polarized in the plane of the trajectory of the radiating particle and left {right} elliptically polarized below {above} this plane (for details on synchrotron radiation see the book of Jackson [54]).

For research using synchrotron radiation, it is usually provided by facilities

based on *storage rings*. A storage ring is a particle accelerator designed to keep relativistic charged particles in a closed orbit. It consists of a closed vacuum tube oriented in the horizontal plane with a typical circumference nowadays of several hundreds of meters. The tube consists of several straight sections; the particles moving within the tube are redirected from section to section by means of *bending magnets*. In the straight sections of the storage ring *insertion devices* can be placed. The bending magnets and the insertion devices produce synchrotron radiation. The light from a bending magnet or an insertion device enters a vacuum tube connected to the storage ring and equipped with *focusing mirrors* and a *monochromator*. The tube leads to an *end station*, in which the light is used for measurements. The entire system starting from the source of synchrotron radiation and ending at the end station is called a *beamline*. The energies of the charged particles (usually electrons) in the storage ring are maintained at a constant level by the electric field of a *radio-frequency cavity*; the stored particles have usually energies of several gigaelectronvolts. The filling of the storage ring by the particles is performed by an *injection system*, which fills the ring when the total current of the stored particles has decayed to a minimal acceptable level.

An insertion device consists of magnetic arrays producing a periodically changing magnetic field and mounted around the vacuum tube of the storage ring. The magnetic field of the insertion device forces the charged particles circulating within the tube to move in a curved (sinusoidal, helical, or more complicated) trajectory. In the simplest case of a sinusoidal trajectory, the particles passing through the magnetic field are accelerated at the turning points of the trajectory and, as a result, emit radiation. Depending on the exact trajectory, the radiation emitted at the different turning points can add incoherently or coherently. In case of an incoherent superposition, the insertion device is called the *wiggler*, and the spectrum is continuous, while in case of a coherent superposition, the insertion device is called the *undulator*, and the spectrum consists of narrow high-intensity peaks called *harmonics*. By changing the size of the *gap* between the magnetic arrays, the magnetic field in the coherent points is changed as well. As a result, waves with other wavelengths begin to interfere. In this way the positions of the harmonics in the spectrum can be changed in order to obtain a maximum possible intensity for a desired photon energy. This possibility makes the undulator an irreplaceable instrument for our study, since it allows to produce the radiation containing high-intensity soft X-rays of an energy suitable for ionization of any molecular core level. The high intensity of the light plays also an important role because it substantially increases the count rates of the photoelectrons and/or Auger electrons, reducing in this way the time required to measure a spectrum.

The spectra of the NO molecule as well as of the CO_2 molecule studied in the present work were measured at the c-branch of beamline 27SU at the synchrotron-

radiation facility SPring-8 (Hyogo, Japan), which is based on an 8-GeV electron storage ring [55]. The figure-8 undulator installed in this beamline produces linearly polarized soft X-rays [56]. When integer order (*i.e.* 1^{st}, 2^{nd}, ...) harmonics of the undulator radiation are chosen, the light is horizontally polarized, whereas the half-integer (*i.e.* 0.5^{th}, 1.5^{th}, ...) harmonics provide vertically polarized light. The measurements of the OCS molecule were performed at beamline I411 at Max II, a synchrotron-radiation facility with an 1.5-GeV electron storage ring (Lund, Sweden) [57]. The undulator used at this beamline produces a light linearly polarized in the horizontal plane [58]. Linear polarization of the light is important in our measurements because in this case a certain angle between the electric-field vector and the entrance point of an electron-energy analyzer can be used that allows to avoid angular-distribution effects, see Section 2.3.

2.2 Monochromator

For synchrotron radiation in the soft X-ray region, the most important optical element of a monochromator is the *grating*, which is located between an *entrance slit* and an *exit slit* (in case of a well-focused undulator beam, the entrance slit can be absent). Depending on the grating, the monochromator can cover different photon-energy ranges. By rotating the disperser, the energy range of the photons passing through the exit slit can be changed. In this way a narrow band located at a photon energy required for the measurements can be chosen from the initial spectrum of synchrotron radiation. The possibility to chose the photon energy for the photoionization process is important in our measurements, since it allows to select an optimal energy with respect to the different factors that influence a certain core-level spectrum of the molecule under study, see page 34.

If we change the width of the exit slit, the *photon bandwidth*, *i.e.* the *photon-energy resolution*, can be changed as well; this property depends also on the energy of photons passing through the slit (the lower the photon energy, the smaller the photon bandwidth and the higher the photon-energy resolution). A high photon-energy resolution, in combination with a high resolution of the electron-energy analyzer, see Section 2.3, is required to resolve the vibrational structure in a photoelectron spectrum, which is needed for a Franck-Condon analysis, see page 18. In order to increase the count rate, the Auger spectrum is usually measured at a much lower photon-energy resolution than the corresponding photoelectron spectrum; this is possible, since the photon bandwidth in the excitation process does not contribute to the experimental resolution of an Auger spectrum, see Section 2.3.

For a fit analysis of the Auger spectrum, some parameters of the respective photoelectron spectrum, like the intensities of the different electronic and vibrational

transitions, are required. Since these parameters can depend on the photon energy, see page 34, the photoelectron spectrum and the subsequent Auger spectrum are always measured at the same photon energy; the larger photon bandwidth used in a measurement of the Auger spectrum does not change the values of the mentioned parameters.

High-resolution monochromators installed in the c-branch of beamline 27SU at SPring-8 and in beamline I411 at Max II – a Hettrick-type monochromator [59] and a modified monochromator Zeiss SX-700 [60], respectively – are both equipped with plane gratings. The former provides three different gratings covering in this way the photon-energy range from 170 eV to 2300 eV. The O $1s^{-1}$ {N $1s^{-1}$} photoelectron and Auger spectra of the NO molecule were measured at this beamline using a photon energy of 650 eV {500 eV}. The C $1s^{-1}$ photoelectron and Auger spectra of the CO_2 molecule were also studied at this beamline using a photon energy of 400 eV. The flux of the monochromatic light corresponding to these energies amounts to approximately 10^{10} $\frac{\text{photons}}{\text{s}\cdot 100\text{mA}}$. The photon bandwidth for the O $1s^{-1}$ {N $1s^{-1}$} photoelectron spectrum of the NO molecule was estimated to be 50 meV {35 meV}, and for the C $1s^{-1}$ photoelectron spectrum of the CO_2 molecule as 35 meV. The usable photon-energy range at beamline I411 is from 50 eV to 1500 eV. The S $2p^{-1}$ photoelectron spectra and the subsequent Auger spectra of the OCS molecule were measured at this beamline with photon energies of 200 eV, 220 eV, and 240 eV at photon fluxes of approximately 10^{12} $\frac{\text{photons}}{\text{s}\cdot 100\text{mA}}$. The photon bandwidth for the S $2p^{-1}$ photoelectron spectra was estimated to be 15 meV.

2.3 Experimental end station

The end stations used in the present measurements consist of an *ultra-high vacuum chamber* equipped with an *electron spectrometer*. To increase the pressure of the studied molecules in the interaction area of the molecules with the monochromatic light (and, as a consequence, to increase the number of ejected electrons and the count rate), the vacuum chamber was equipped with a *gas cell* with a constant gas stream.

Hemispherical electron-energy analyzers were used as spectrometers. A typical hemispherical analyzer consists of two electrodes in form of concentric hemispheres with the inner one charged positively and the outer one charged negatively. Electrons enter the space between the hemispheres through an *entrance slit* and move by the action of the deflection potential towards the opposite side of the analyzer. On the opposite side an *imaging screen* representing a *micro-channel plate* (MCP) is situated for detecting the electrons. The electric field of the hemispheres is maintained at a constant value during a spectrum measurement. Thus, only electrons with the same kinetic energy at the entrance can reach the screen; this energy

is called the *pass energy* E_p. Before entering the entrance slit of the analyzer, the electrons pass the retarding voltage of the *retarding system*. This system reduces the kinetic energy of all electrons by a definite value ΔE_r. In this case, for an electron reaching the imaging screen, the kinetic energy at the moment before entering the retarding system can be calculated as $(E_p + \Delta E_r)$. A spectrum measurement process consists in changing the retarding voltage, *i.e.* the value ΔE_r, by a constant step, and collecting the electrons for each value ΔE_r during the same time; after the measurement, the spectrum requires a calibration of the kinetic-energy scale.

The width of the entrance slit and the pass energy influence the *analyzer resolution* (the narrower the slit or the lower the pass energy, the higher the resolution). The analyser resolution as well as the *Doppler broadening* defines the so-called *experimental resolution* or the *experimental broadening*; the Doppler broadening is caused by the movements of the molecules which emit the electrons with respect to the analyzer and, to a considerably less degree, by the relative movements of the molecule and the incident photons. In case of a photoelectron spectrum, the photon bandwidth contributes directly to the experimental broadening as well, while it has no influence on the Auger spectrum because the Auger-electron kinetic energies are not depending on the photon bandwidth. In addition, the recoil effect [51] makes some contribution to the experimental broadening for both types of spectra. Thus, the experimental resolution differs for the photoelectron spectrum and the Auger spectrum. In the present study, we estimate the experimental broadenings of the photoelectron and Auger spectra from our fit analyses, see page 105.

The hemispherical analyzers used in the present experiments provide high resolutions. As a result, the present photoelectron and Auger spectra reveal the vibrational structure that is necessary to perform a Franck-Condon analysis, see page 18.

The present measurements were performed using permanent end stations at the c-branch of beamline 27SU at SPring-8 and at beamline I411 at Max II. The former is equipped with an electron-energy analyzer SES-2002 [61], the latter with an analyzer SES-200 [62, 63]; both are manufactured by Gammadata-Scienta Ab. All spectra were measured with entrance slits of the analyzers of 200 µm. The spectra of the NO molecule as well as of the CO_2 molecule were measured using pass energies of 50 eV and 100 eV for the photoelectron and Auger spectra, respectively; these values correspond to analyzer resolutions of approximately 36 meV and 66 meV, respectively. The spectra of the OCS molecule were measured at a pass energy of 10 eV corresponding to an analyzer resolution of approximately 20 meV. The experimental resolutions for the O $1s^{-1}$ {N $1s^{-1}$} photoelectron spectrum and the subsequent Auger spectrum of the NO molecule are estimated to be 66 meV {63 meV} and 136 meV {120 meV}, respectively; for the photoelectron and Auger spectra of the CO_2 molecule as 50 meV and 70 meV, respectively; and for the photoelectron and Auger spectra of the OCS molecule as 30 meV and 40 meV, respectively.

The electron-energy analyzer SES-200 at beamline I411 can be rotated in the plane perpendicular to the light beam. In order to avoid angular-distribution effects [64, 65], all spectra of the OCS molecule were collected with the analyzer set to a position where the angle θ between the electric-field vector and the entrance point of the analyser amounts to approximately 54.7°; at this angle the angular-distribution parameter β_{nl} has no influence on the spectrum. This angle, also known as the *magic angle*, can be used because synchrotron radiation is linearly polarized in the horizontal plane, see Section 2.1. The analyzer SES-2002 at beamline 27SU is mounted in the horizontal direction. The undulator at this beamline produces light linearly polarized either in the horizontal plane or in the vertical plane leading to the angles $\theta = 0°$ and $\theta = 90°$, respectively. In this case, a spectrum analogous to that measured at the magic angle can be obtained by a summation of the spectra measured at 0° and at 90° taken with intensity factors of 1 and 2, respectively.

All photoelectron and Auger spectra were measured at room temperature. The gases NO and CO_2 used in the experiments had a purity of better than 99.5%, while the OCS gas a purity of 97.5%.

Chapter 3

Results and discussions

In the present chapter the results of the analyses of the photoelectron and Auger spectra of the molecules NO, CO_2, and OCS are presented; the results are discussed in detail in Sections 3.1, 3.2, and 3.3, respectively.

At the beginning of each section some details about the analysis of the corresponding spectra, like the relation between the normal coordinates and the internal coordinates and energy calibration, are given. The assignment of the transitions in the Auger spectra of the NO and the OCS molecules is partially based on calculations of our colleagues. Therefore, we also present in Sections 3.1 and 3.3 the corresponding theoretical results used in this work. After this, we directly present the results of the fit analyses of the photoelectron and Auger spectra: here we describe additional details of the data analysis, compare our results with results of other authors, and lead further discussion.

3.1 O $1s^{-1}$ and N $1s^{-1}$ photoelectron and Auger spectra of NO

Up to now several studies were performed to obtain information on the potential-energy curves of dicationic states of NO. In 1987 and 1991, Cossart *et al.* [66, 67] studied the rotationally resolved optical $B^2\Sigma^+$ ($v = 0$) $\rightarrow$ $X^2\Sigma^+$ ($v = 0$) transitions of $^{14}NO^{2+}$ and $^{15}NO^{2+}$, and in this way obtained the equilibrium distances R_0 of the two states involved in the transition. Later, Pettersson *et al.* [68] measured an Auger spectrum of the NO molecule, which showed a structure that was assigned to vibrational transitions; however, these medium-resolution spectra did not allow to extract information about the potential-energy curves. In the mid-1990s, Dawber *et al.* [69] derived from *threshold-photoelectron-coincidence* (TPEsCO) spectra the energy positions, the vibrational energies, and the anharmonicities for the three lowest states $X^2\Sigma^+$, $A^2\Pi$, and $B^2\Sigma^+$ of NO^{2+}. Finally, in 2003, Eland *et al.* [70] employed *time-of-flight photoelectron-photoelectron-coincidence* (TOF-PEPECO) spectroscopy to derive the energy positions for the lowest vibrational levels of the three lowest states; these values also allow to derive the vibrational energies and the anharmonicities. In the same year, Furuhashi *et al.* [11] published equilibrium distances for the dicationic states $X^2\Sigma^+$ and $A^2\Pi$ derived from vibrationally resolved *double-charge-transfer* (DCT) spectra. Theoretical studies of a larger number of dicationic states in the NO molecule have been performed by Cooper [71], Wetmore and

Boyd [72], and Pettersson *et al.* [73]. The calculations of Wetmore and Boyd [72] predict only the two lowest states to be metastable, namely $X^2\Sigma^+$ and $A^2\Pi$, while the other calculations result in metastable potential-energy curves for the three lowest states – $X^2\Sigma^+$, $A^2\Pi$, and $B^2\Sigma^+$.

From the results of previous studies, we expected vibrational progressions in the Auger spectra of the NO molecule. Because of this, high-resolution photoelectron and Auger spectra with a good signal-to-noise ratio were measured at beamline 27SU at SPring-8 in Japan. As expected, all spectra exhibit vibrational progressions. The Auger spectrum of the NO molecule subsequent to O $1s^{-1}$ {N $1s^{-1}$} photoionization is shown in Figure 3.3 {Figure 3.4}, the corresponding photoelectron spectrum in Figure 3.1 {Figure 3.2}.

Details of data analysis

The **L** matrix for the electronic ground state of the NO molecule is calculated in Appendix B, see eqn. B.3. For diatomic molecules, the **L** matrix is identical for all electronic states. Therefore, the transformation equation 1.54 can be rewritten for the NO molecule as

$$\Delta R_e(\mathrm{N{-}O}) = 0.366 \cdot \Delta Q_e,$$

where Q_e is the equilibrium value of the normal coordinate corresponding to the only vibration present.

Since transitions to three dicationic states are visible in both Auger spectra, we fitted these spectra simultaneously by using the same set of parameters for the potential-energy curves of these three states in order to increase the reliability of the fit parameters. In this way, we obtained a consistent description of all four spectra by using only approximately 60 fit parameters. This includes about 30 parameters for describing the backgrounds of the Auger spectra.

In order to calibrate the binding-energy scales of the photoelectron spectra, values of 543.75(1) eV for the O $1s$ $^1\Pi$ binding energy reported by Püttner *et al.* [74] and 411.81(2) eV for the N $1s$ $^1\Pi$ binding energy reported by Remmers *et al.* [75] are used. The calibration of the kinetic-energy scales of the Auger spectra is performed on the basis of these binding energies as well as the double-ionization energy of 38.46(1) eV for the dicationic state $X^2\Sigma^+$ reported by Eland *et al.* [70]. In this way, an accuracy of 20 meV {30 meV} is obtained for the kinetic-energy scale of the Auger spectrum subsequent to O $1s^{-1}$ {N $1s^{-1}$} photoionization.

In the fit analysis of the Auger spectrum subsequent to O $1s^{-1}$ {N $1s^{-1}$} photoionization, the PCI shift ΔT^p for the vibrational lifetime-interference terms, see Section 1.8, amounts to approximately 14 meV {11 meV}.

Calculations of our colleagues

The present Auger spectrum of the NO molecule subsequent to N $1s^{-1}$ photoionization reveals the hitherto unobserved transitions to metastable dicationic states at approximately 9 eV and 10.5 eV above the ground state of NO^{2+}, see Figure 3.4. These two states are not reproduced by any of the above mentioned theoretical studies. The only theoretical results predicting metastable states in this energy region were presented by Baková *et al.* [32]. In that work, however, the focus was on the lifetimes of the four lowest dicationic states; the potential-energy curves of the higher states were shown only in an overview figure that does not allow to extract detailed information. Because of this, we established a collaboration with two of the authors of the mentioned publication, namely with Dr. Vladimir Špirko and Dr. Tereza Šedivcová-Uhlíková from Prague, Czech Republic. They extracted from their calculations more detailed information about the potential-energy curves of the higher diatomic states that were not in the focus of the work of Baková *et al.* [32]. In addition, they calculated the spin-orbit splitting of one of the dicationic states, namely the state $A^2\Pi$. We combined these theoretical results with the present experimental results obtained from the data analysis and found good agreement. In particular, these calculations predict five metastable states, which are expected to cause vibrational progressions in the Auger spectra and, as a result, allowed us to assign the two previously not observed dicationic states to $C^2\Sigma^+$ and $c^4\Pi$. These more detailed calculations were published together with our experimental result, which are being discussed in the present section. Therefore, in the following, when we refer to these calculations, we give a reference to our joint paper [76]. The results of the calculations are also presented in Tables 3.3 and 3.4 and Figures 3.6 and 3.7. More details about these calculations can be found in Refs. [32, 76].

Ground state

The electronic configuration of the NO molecule in the ground state is

$$1\sigma^2\ 2\sigma^2 \mid 3\sigma^2\ 4\sigma^2\ 1\pi^4\ 5\sigma^2\ 2\pi^1,$$

where the 1σ and the 2σ orbitals represent the O $1s$ and the N $1s$ core levels, respectively, and the remaining five orbitals describe the valence shell of the molecule. Due to spin-orbit coupling of the 2π electron, the ground-state configuration of the NO molecule is split into the two states $X^2\Pi_{1/2}$ and $X^2\Pi_{3/2}$ that differ energetically by $\Delta E_0 = 15.015$ meV [77]. In the fit analysis, we take into account different populations of the two states according to Boltzmann statistics

$$N(E) = N(0) \cdot e^{-\frac{E}{k \cdot T}},$$

where $T = 300$ K is the temperature of the gas and k is the Boltzmann constant.

For both states of the ground-state configuration of the NO molecule we assume in the Franck-Condon analysis an equilibrium distance $R_e = 1.1508$ Å, a vibrational energy $\hbar\omega = 235.9$ meV, and an anharmonicity $x\hbar\omega = 1.7309$ meV [77].

Photoelectron spectra

The photoelectron spectra of the NO molecule above the O 1s and the N 1s ionization thresholds are shown in Figures 3.1 and 3.2, respectively. Due to the interaction of the spin moments of the 1s and the 2π electrons, we observe in each photoelectron spectrum the core-ionized states $^1\Pi$ and $^3\Pi$, *i.e.* we observe – with decreasing binding energies – the core-ionized states O $1s^{-1}$ $^1\Pi$, O $1s^{-1}$ $^3\Pi$, N $1s^{-1}$ $^1\Pi$, and N $1s^{-1}$ $^3\Pi$. In the fit analysis, these states are described by individual potential-energy curves. Transitions to all of these states are allowed from the two thermally occupied states of the neutral molecule $X^2\Pi_{1/2}$ and $X^2\Pi_{3/2}$. In order to obtain accurate values of lifetime broadening, all four electronic transitions were included in the fit analysis. We also assume that the spin of the 2π electron has no influence on the photoionization cross section, *i.e.* the intensity ratio of the subspectra, given by the solid and the dash-dotted lines in the figures, is fully described by the different thermal population of the spin-orbit split states $X^2\Pi_{1/2}$ and $X^2\Pi_{3/2}$ of the ground-state configuration, see page 51.

The determination of realistic error bars is not straightforward in the present data analysis, since systematic errors are much larger than statistical errors. These systematic errors are caused by small spectral contributions that are not resolved or known and hence not considered in the fit analysis like, for example, small variations in gas pressure or unknown values for the anharmonicities. In the present case, the anharmonicities of the core-ionized states cannot be obtained in the fit analysis, since vibrational substates higher than $v' = 1$ are not well enough observed in the spectra, see eqn. 1.16. Since anharmonicities are expected to influence the fit results, we consider them as the main source of systematic errors. As a consequence, we estimated the anharmonicities of the core-ionized states according to a procedure described below and have varied the anharmonicities in our analysis around these values to obtain the realistic error bars presented.

Since the vibrational substate $v' = 2$ is very weak for all core-ionized states, it is not surprising that a fit approach with equilibrium distances, vibrational energies, and anharmonicities of the core-ionized states as free parameters resulted in unreasonable values for the anharmonicities of the core-ionized states. Since these anharmonicities are expected to have a significant influence on the other fit parameters and are not available in the literature, we estimated them by using the anharmonicities of analogous ions in the $(Z+1)$-*core analogy model* [78], *i.e.* the anharmonicities of NF^+ and O_2^+, namely $x\hbar\omega(NF^+) = 1.2(7)$ meV [79] and $x\hbar\omega(O_2^+) =$

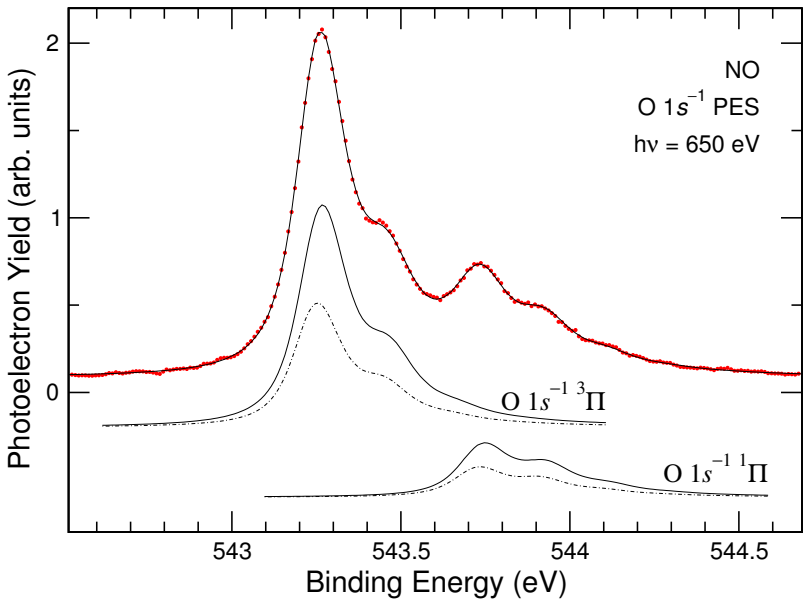

Figure 3.1: O $1s^{-1}$ photoelectron spectrum of the NO molecule measured at a photon energy of 650 eV. The solid line through the data points represents the fit result. The four subspectra result from transitions from the states $X^2\Pi_{1/2}$ (solid lines) and $X^2\Pi_{3/2}$ (dash-dotted lines) of the neutral molecule to the core-ionized states $^1\Pi$ and $^3\Pi$.

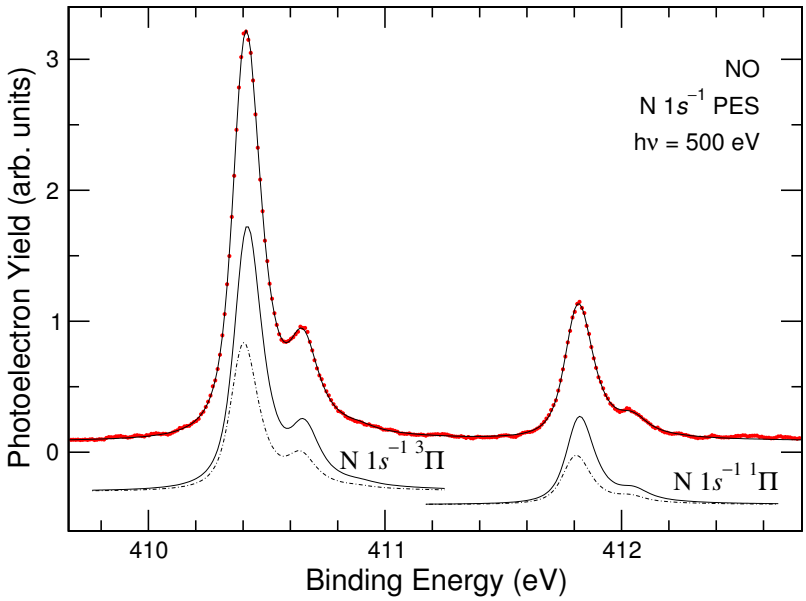

Figure 3.2: N $1s^{-1}$ photoelectron spectrum of the NO molecule measured at a photon energy of 500 eV. For a description of the lines see Figure 3.1.

Table 3.1: Equilibrium distances R_e, vibrational energies $\hbar\omega$, and anharmonicities $x\hbar\omega$ of the core-ionized states derived from the fit analyses of the O $1s^{-1}$ and the N $1s^{-1}$ photoelectron spectra of the NO molecule. Values for the ground state taken from the literature [77] are included for comparison.

state	R_e, Å	$\hbar\omega$, meV	$x\hbar\omega$, meV
ground state	1.1508	235.9	1.7309
O $1s^{-1}$ $^1\Pi$	1.2014(6)	192(2)	1.3(8)[a]
O $1s^{-1}$ $^3\Pi$	1.1855(9)	206(2)	
N $1s^{-1}$ $^1\Pi$	1.1280(5)	235(1)	2.2(5)[a]
N $1s^{-1}$ $^3\Pi$	1.1216(4)	247(1)	

[a] Estimated, see eqns. 3.1 and 3.2; fixed in the fit analysis.

2.0(5) meV [80]. Then, we refined these anharmonicities in compliance with the equations

$$x\hbar\omega(\mathrm{NO\ O}\ 1s^{-1}) = x\hbar\omega(\mathrm{NF^+}) \cdot \frac{\mu_{\mathrm{NF}}}{\mu_{\mathrm{NO}}} \tag{3.1}$$

and

$$x\hbar\omega(\mathrm{NO\ N}\ 1s^{-1}) = x\hbar\omega(\mathrm{O_2^+}) \cdot \frac{\mu_{\mathrm{O_2}}}{\mu_{\mathrm{NO}}}, \tag{3.2}$$

where the parameters μ are reduced masses of the corresponding molecules; to obtain these relations, eqn. 1.13 is used.

The equilibrium distances R_e and the vibrational energies $\hbar\omega$ derived in the subsequent fit analysis as well as the anharmonicities $x\hbar\omega$ derived with eqns. 3.1 and 3.2 are summarized in Table 3.1. As discussed, the error bars for the equilibrium distances and the vibrational energies originate from different values for the anharmonicities. This shows that neglecting the anharmonicities completely would lead to systematic errors of the order of 1 mÅ for the equilibrium distances.

Up to now only equilibrium distances and vibrational energies obtained in the harmonic approximation for the potential-energy curves are available in the literature. In this approach Rüdel *et al.* [81] report harmonic vibrational energies of 200 meV for both the O $1s^{-1}$ $^1\Pi$ and the O $1s^{-1}$ $^3\Pi$ core-ionized states, and 237(5) meV for both the N $1s^{-1}$ $^1\Pi$ and the N $1s^{-1}$ $^3\Pi$ core-ionized states. Hoshino *et al.* [82] observed for the vibrational energies of the N $1s^{-1}$ core-ionized state values of 228 meV and 256 meV, respectively, for its $^1\Pi$ and $^3\Pi$ components, *i.e.* all these values are in reasonable agreement with the present results. The latter authors present also equilibrium distances of 1.13197 Å and 1.12865 Å for the N $1s^{-1}$ $^1\Pi$ and the N $1s^{-1}$ $^3\Pi$ core-ionized states, respectively, which are several mil-

liangstroms larger than the present values; the differences are caused by a neglect of anharmonicities.

For the core-ionized states O $1s^{-1}$ $^1\Pi$, O $1s^{-1}$ $^3\Pi$, N $1s^{-1}$ $^1\Pi$, and N $1s^{-1}$ $^3\Pi$, lifetime widths Γ of 160(3) meV, 148(2) meV, 112(3) meV, and 108(3) meV, respectively, are derived, where the given error bars are estimated by varying the estimated experimental resolution by 10 meV to both lower and higher values. The difference of the lifetime widths $\Delta\Gamma = \Gamma(^3\Pi) - \Gamma(^1\Pi)$, however, could be derived with higher precision resulting in $\Delta\Gamma(\mathrm{O}\ 1s^{-1}) = 12.0(4)$ meV and $\Delta\Gamma(\mathrm{N}\ 1s^{-1}) = 3.9(2)$ meV. The actual differences of the lifetime widths of the core-ionized states $^1\Pi$ and $^3\Pi$ can be even larger, since the values for the latter states are only upper limits due to a possible unresolved splitting into the states $^3\Pi_0$, $^3\Pi_1$, and $^3\Pi_2$. The observed differences in the lifetime widths for the core-ionized states $^1\Pi$ and $^3\Pi$ are fully in line with the calculations of Ågren [83] resulting in different Auger-transition rates, see Table 3.5.

From the fit analysis, a splitting of 0.484(3) eV {1.4105(2) eV} between the O 1*s* $^1\Pi$ {N 1*s* $^1\Pi$} and the O 1*s* $^3\Pi$ {N 1*s* $^3\Pi$} core-ionized states is obtained. This value is in good agreement with a value of 0.48 eV {1.41 eV} reported recently by Rüdel *et al.* [81] and with a value of 0.530(21) eV {1.412(16) eV} reported much earlier by Davis and Shirley [84]. Values of 1.47 eV and 1.40 eV derived for N $1s^{-1}$ ionization by Remmers *et al.* [75] and by Hoshino *et al.* [82], respectively, are also in reasonable agreement with the present results.

The $^3\Pi$ to $^1\Pi$ intensity ratio is found to be 3.10(9) in both photoelectron spectra. This number is fully in line with the multiplicity of the states $^1\Pi$ and $^3\Pi$ and suggests a photoionization cross section of the 1*s* electrons independent of the spin of the 2π electron. This result justifies the assumption made above, see page 48, that the photoelectron cross sections for excitations from the states $X^2\Pi_{1/2}$ and $X^2\Pi_{3/2}$ of the ground-state configuration are identical.

Auger spectra

The Auger spectra of the NO molecule subsequent to O $1s^{-1}$ and N $1s^{-1}$ photoionizations are measured in the kinetic-energy regions from 497.4 eV to 506.4 eV and from 359.4 eV to 376.4 eV, respectively. In these regions, previous medium-resolution Auger spectra reported by Pettersson *et al.* [68] revealed a set of narrow peaks, which were tentatively assigned to vibrations. As mentioned above, see page 46, in the present study both Auger spectra are fitted simultaneously in order to use the same sets of Morse parameters as well as relative energy positions for the dicationic states observed in both spectra. The spectra are presented in Figures 3.3 and 3.4, respectively, along with the corresponding fit results.

Due to the two core-ionized states $^1\Pi$ and $^3\Pi$ visible in each photoelectron spec-

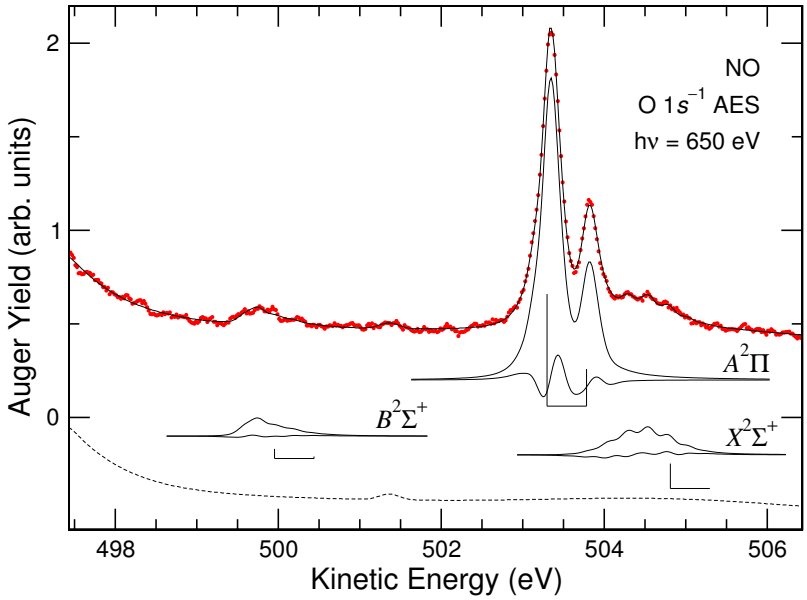

Figure 3.3: Auger spectrum of the NO molecule subsequent to O $1s^{-1}$ photoionization measured at a photon energy of 650 eV in the kinetic-energy region from 497.4 eV to 506.4 eV. The solid line through the data points represents the fit result, and the short-dashed line indicates the background used in the fit analysis. The vertical-bar diagrams give the kinetic-energy positions and the relative intensities of the Auger transitions, with the bar at higher {lower} kinetic energy representing the transition through the $^1\Pi$ $\{^3\Pi\}$ core-ionized state. The bars mark the kinetic-energy positions of the transitions $v' = 0 \rightarrow v = 0$. The upper subspectra represent the vibrational progressions of the Auger transitions through the core-ionized states $^1\Pi$ and $^3\Pi$ to the individual metastable dicationic states, and the lower subspectra the corresponding contributions from the vibrational lifetime interference.

trum, two transitions to each dicationic state are observed in the Auger spectra. In Figure 3.5 all revealed vibrational progressions as well as the contributions from the vibrational lifetime interference are summarized. The differences of the vibrational progressions in the O $1s^{-1}$ and the N $1s^{-1}$ Auger spectra are due to the different Franck-Condon regions of the Auger decay, see Figures 3.6 and 3.7.

In total, we observe five metastable dicationic states, namely $X^2\Sigma^+$, $A^2\Pi$, $B^2\Sigma^+$, $C^2\Sigma^+$, and $c^4\Pi$. Values of the parameters of the potential-energy curves of these states derived from the fit analysis are presented in Table 3.2; theoretical values from Ref. [76] are included in Table 3.3. The excitation energies of the dicationic states relative to the ground state of NO^{2+} are given in Table 3.4, and the intensities of the transitions in Table 3.5.

The three lowest dicationic states $X^2\Sigma^+$, $A^2\Pi$, and $B^2\Sigma^+$ are well known from the literature, however, with partially different values of the spectroscopic param-

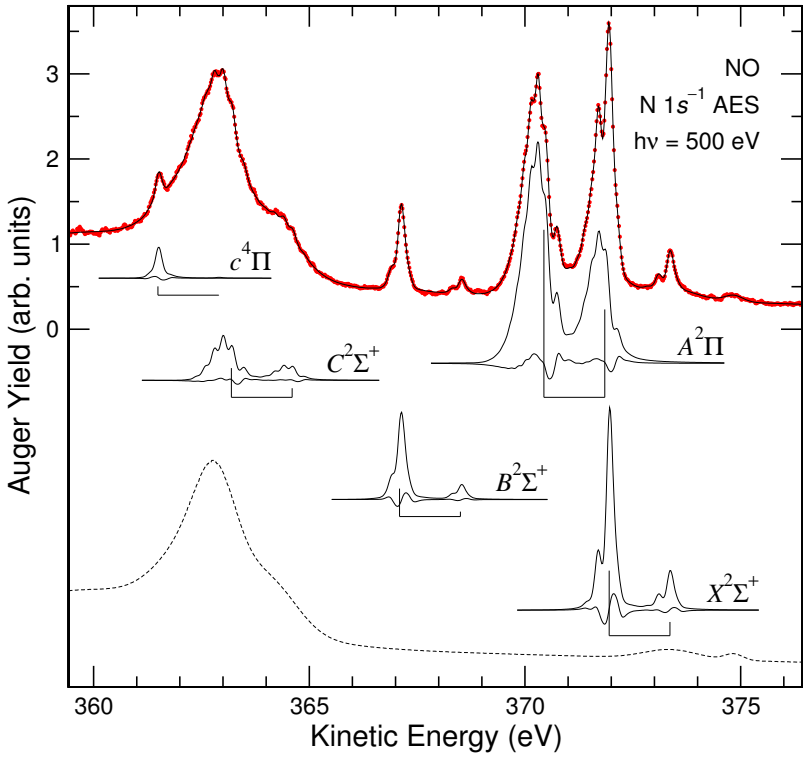

Figure 3.4: Auger spectrum of the NO molecule subsequent to N $1s^{-1}$ photoionization measured at a photon energy of 500 eV in the kinetic-energy region from 359.4 eV to 376.4 eV. For a description of the bar diagrams and the lines see Figure 3.3.

eters, see Tables 3.2 and 3.3. Consequently, the main aim on the data analysis of the corresponding Auger transitions is to obtain a new set of highly reliable spectroscopic data. The remaining two metastable dicationic states are not known from literature. Based on the theoretical results reported in Ref. [76], they are assigned to the dicationic states $C^2\Sigma^+$ and $c^4\Pi$. In the following, we discuss in detail the Auger transitions to these five dicationic states.

Auger transitions
O $1s^{-1} \rightarrow X^2\Sigma^+$
N $1s^{-1} \rightarrow X^2\Sigma^+$

The strongly overlapping vibrational progressions belonging to the dicationic states $X^2\Sigma^+$ and $A^2\Pi$ did not lead to reasonable values of the anharmonicities when all Morse parameters were treated as free parameters in the fit analysis. We, therefore, fixed the anharmonicity of the dicationic state $X^2\Sigma^+$ to a value of 2.56 meV given by Dawber *et al.* [69], see Table 3.2, since we consider this value as the most reliable one in the literature. In this way an equilibrium distance of $R_e = 1.090(1)$ Å was obtained in our analysis for the dicationic state $X^2\Sigma^+$, which can be compared with the values derived by Cossart *et al.* [66, 67] from their high-resolution optical

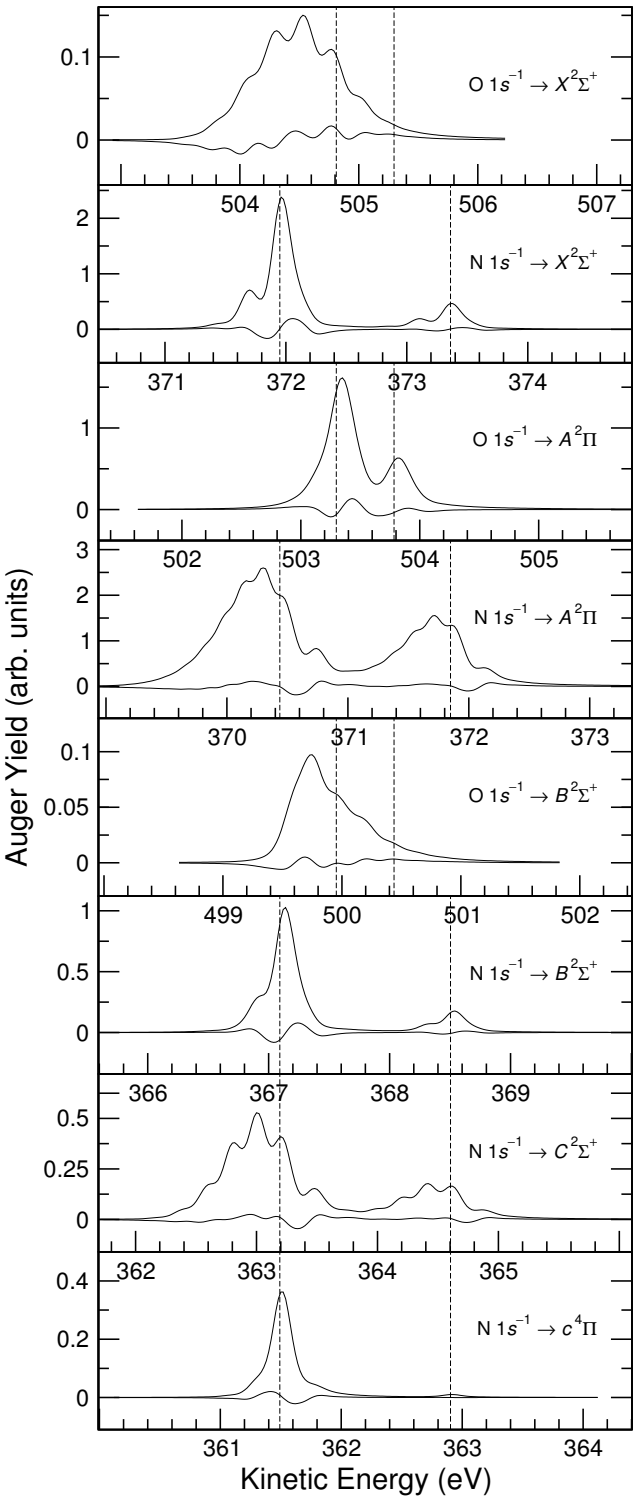

Figure 3.5: Detailed representation of the vibrational progressions of the Auger transitions (upper subspectra) and the corresponding contributions from the vibrational lifetime interference (lower subspectra) that are shown in Figures 3.3 and 3.4. The dashed vertical lines give the positions of the Auger transitions with the line at higher {lower} kinetic energy representing the transition through the $^1\Pi$ $\{^3\Pi\}$ core-ionized state.

rotational-spectroscopy data. These authors derived the rotational constants B_0 of the vibrational ground states of the dicationic states $X^2\Sigma^+$ and $B^2\Sigma^+$ that correspond to internuclear distances of $R_0 = 1.0926$ Å and $R_0 = 1.0963$ Å, respectively; these values are included in Table 3.2.

In the present fit analysis we derive the internuclear distance for the minimum of the potential-energy curve R_e, which is different from the expectation value of the internuclear distance in the vibrational ground state R_0. The rotational constant B derived in rotationally resolved spectroscopy is inversely proportional to the moment of inertia of a molecule and, as a consequence, to the square of its internuclear distance. We can, therefore, calculate the rotational constant B_e from the fit result for the equilibrium distance R_e corresponding to the minimum of the potential-energy curve by using the formula

$$B_e = \frac{h}{8\pi^2 \cdot c \cdot \mu \cdot R_e^2},$$

where h is the Planck constant and c the speed of light. To compare the present values for B_e with the values for B_0 reported by Cossart *et al.* [66, 67], we use the relation between the rotational constant B_v for the vibrational state v and the rotational constant B_e, namely

$$B_v = B_e - \alpha_e \cdot \left(v + \frac{1}{2}\right).$$

In order to obtain perfect agreement between the present equilibrium distance R_e and the value R_0 reported by Cossart *et al.* [66, 67], we have to assume $\alpha_e = 0.015$ cm^{-1} for the dicationic state $X^2\Sigma^+$. This value agrees well with $\alpha_e = 0.02$ – 0.06 cm^{-1} reported by Cossart *et al.* [66, 67]; it is discussed in more detail further below, see page 60.

There is also good agreement with the value of $R_e = 1.088(2)$ Å reported by Furuhashi *et al.* [11]. The experimental equilibrium distance of the present study is also in excellent agreement with the value of 1.0875 Å calculated in Ref. [76]. The theoretical potential-energy curves of the doublet states reported in Ref. [76] are displayed in Figure 3.6, while those of the quartet and the sextet states are presented in Figure 3.7. For comparison, Morse potentials based on the present data analysis are also shown in these figures; in general, Figures 3.6 and 3.7 illustrate excellent agreement between experiment and theory.

For the vibrational energy $\hbar\omega$, a value of 260(2) meV is derived from the present fit analysis, which is in good agreement with the experimental value of 257.26 meV reported by Dawber *et al.* [69] and identical to the theoretical value of 261 meV given in Ref. [76]. Note that some of the vibrational energies and the anharmonicities presented in Table 3.2 have been obtained by fitting the reported peak positions

Table 3.2: Equilibrium distances R_e, vibrational energies $\hbar\omega$, and anharmonicities $x\hbar\omega$ of the metastable dicationic states derived from the fit analysis of the Auger spectra of the NO molecule subsequent to O $1s^{-1}$ and N $1s^{-1}$ photoionizations. Experimental values reported by Furuhashi *et al.* [11], Eland *et al.* [70], Dawber *et al.* [69], and Cossart *et al.* [66, 67] are included for comparison.

parameter	state	present work	[11]	[70]	[69]	[66, 67]
R_e, Å	$X^2\Sigma^+$	1.090(1)	1.088(2)			1.0926[a]
	$A^2\Pi$	1.211(2)	1.222(18)			
	$B^2\Sigma^+$	1.085(1)				1.0963[a]
	$C^2\Sigma^+$	1.205(2)				
$\hbar\omega$, meV	$X^2\Sigma^+$	260(2)	252[b]	240[b]	257.26	
	$A^2\Pi$	182(7)	158[b]	220[b]	181.50	
	$B^2\Sigma^+$	222.1(1)		220[c]	224.22	
	$C^2\Sigma^+$	215(1)				
$x\hbar\omega$, meV	$X^2\Sigma^+$	2.56[d]	5[b]	−5[b]	2.56	
	$A^2\Pi$	2(1)	−0.5[b]	20[b]	4.00	
	$B^2\Sigma^+$	9.39[d]			9.39	
	$C^2\Sigma^+$	0.7(7)				

[a] Distance R_0 of the vibrational ground state; for details, see text.
[b] Derived from the positions of the first three vibrational peaks, see eqn. 1.16.
[c] Splitting between the two lowest vibrational levels.
[d] Taken from the work of Dawber *et al.* [69]; fixed in the fit analysis.

to eqn. 1.16. In this way, negative values of the anharmonicities are obtained in a few cases, probably due to unprecise energy positions.

Auger transitions
O $1s^{-1} \rightarrow A^2\Pi$
N $1s^{-1} \rightarrow A^2\Pi$

In the analysis of the vibrational progressions of the Auger transitions to the state $A^2\Pi$, all fit parameters are treated as free parameters. The equilibrium distance $R_e = 1.211(2)$ Å obtained in this way agrees well with the value of 1.222(18) Å reported previously by Furuhashi *et al.* [11]; it is, however, of much higher accuracy and agrees also with the theoretical result of $R_e = 1.2071$ Å from Ref. [76] as well as with $R_e = 1.21$ Å calculated by Wetmore and Boyd [72].

The experimental results for the vibrational energy $\hbar\omega$ reported in the literature for the dicationic state $A^2\Pi$ vary over a wide range from 158 meV to 220 meV. The result of the present work is $\hbar\omega = 182(7)$ meV, which agrees best with the result of $\hbar\omega = 181.50$ meV reported by Dawber *et al.* [69]; the latter value is derived from a long and well-resolved vibrational progression and is, therefore, of high precision. If we compare the present vibrational energy with theoretical results, we find good

Table 3.3: Equilibrium distances R_e, vibrational energies $\hbar\omega$, and anharmonicities $x\hbar\omega$ of the metastable dicationic states calculated in Ref. [76]. Theoretical values reported by Pettersson *et al.* [68, 73], Cooper [71], and Wetmore and Boyd [72] are included for comparison.

parameter	state	[76]	[68, 73][a]	[71]	[72]
R_e, Å	$X^2\Sigma^+$	1.0875		1.11	1.07
	$A^2\Pi$	1.2071		1.24	1.21
	$B^2\Sigma^+$	1.0881		1.13	
	$C^2\Sigma^+$	1.2220			
	$c^4\Pi$	1.1388			
$\hbar\omega$, meV	$X^2\Sigma^+$	261	249.42	242.65	290
	$A^2\Pi$	183	156.40	159.95	177
	$B^2\Sigma^+$	240	211.55	159.95	
	$C^2\Sigma^+$	192.5[b]			
	$c^4\Pi$	222.1[b]			
$x\hbar\omega$, meV	$X^2\Sigma^+$	2.5	2.00	2.60	9.5
	$A^2\Pi$	4.0	2.01	4.09	4.5
	$B^2\Sigma^+$	12.5	13.65	4.09	

[a] Presented in the work of Dawber *et al.* [69], based on the works of Pettersson *et al.* [68, 73].
[b] Splitting between the two lowest vibrational levels.

Table 3.4: Leading configurations as well as relative total energies of the metastable dicationic states derived from the fit analysis of the Auger spectra of the NO molecule subsequent to O $1s^{-1}$ and N $1s^{-1}$ photoionizations. Given are the total-energy differences between the $v = 0$ vibrational levels ΔE_0 and between the minima of the potential-energy curves ΔE_e of the corresponding dicationic states and the ground state $X^2\Sigma^+$ of NO^{2+}. Total-energy differences calculated in Ref. [76] are included in the last column.

state	configuration	present work		[76]
		ΔE_0, eV	ΔE_e, eV	ΔE_e, eV
$X^2\Sigma^+$	$5\sigma^{-1}2\pi^{-1}$	0	0	0
$A^2\Pi$	$1\pi^{-1}2\pi^{-1}$	1.47(1)	1.511(9)	1.5924
$B^2\Sigma^+$	$4\sigma^{-1}2\pi^{-1}$	4.835(4)	4.857(2)	4.8663
$C^2\Sigma^+$	$1\pi^{-1}5\sigma^{-1}$	8.735(5)	8.757(4)	8.8736
$c^4\Pi$	$1\pi^{-2}$	10.446(7)	10.458(6)	10.4926

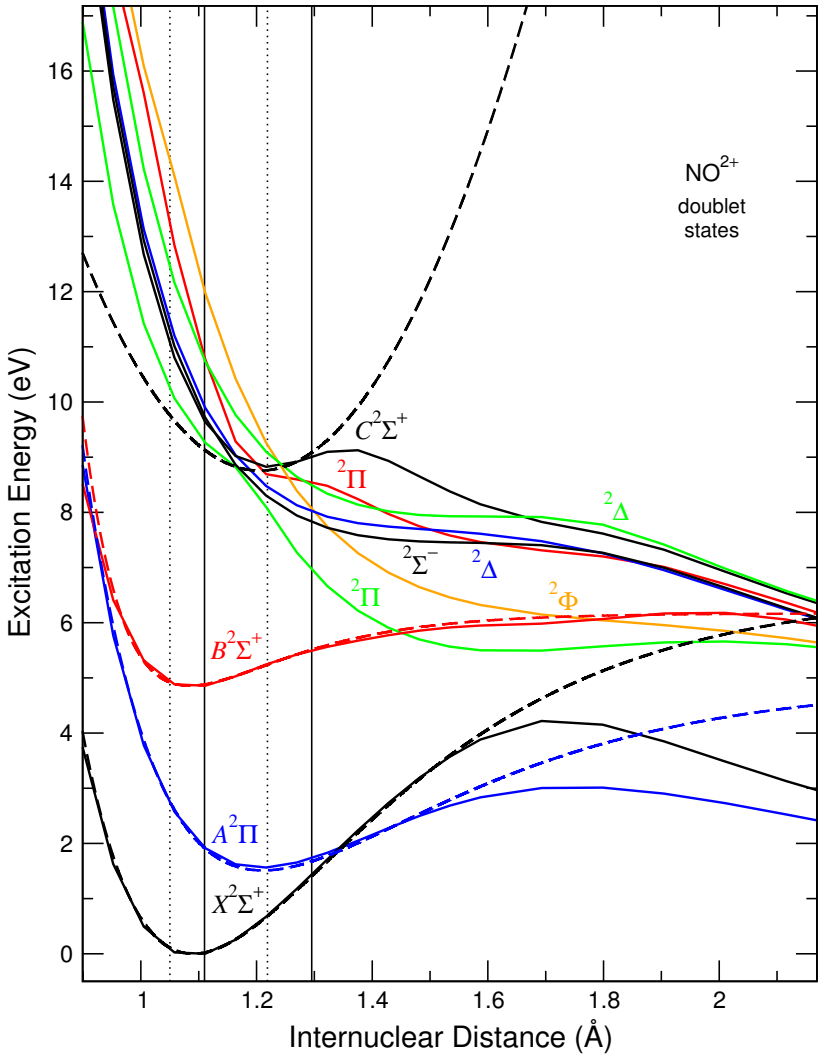

Figure 3.6: Theoretical potential-energy curves of the doublet states from Ref. [76] as well as Morse-potential-energy curves of four of these states derived from the present fit analysis. The solid lines represent the theoretical curves, and the dashed lines the curves derived from the fit procedure. The solid {dotted} vertical lines indicate the boundaries of the Franck-Condon region for the Auger transitions subsequent to O $1s^{-1}$ {N $1s^{-1}$} photoionization.

agreement with the theoretical result of $\hbar\omega = 183$ meV reported in Ref. [76] as well as with the result of $\hbar\omega = 177$ meV reported by Wetmore and Boyd [72], *i.e.* with the results of the same two calculations as in the case of the equilibrium distance. The present value for the anharmonicity $x\hbar\omega$ of $2(1)$ meV is very close to the value of 2.01 meV previously calculated by Pettersson *et al.* [68, 73].

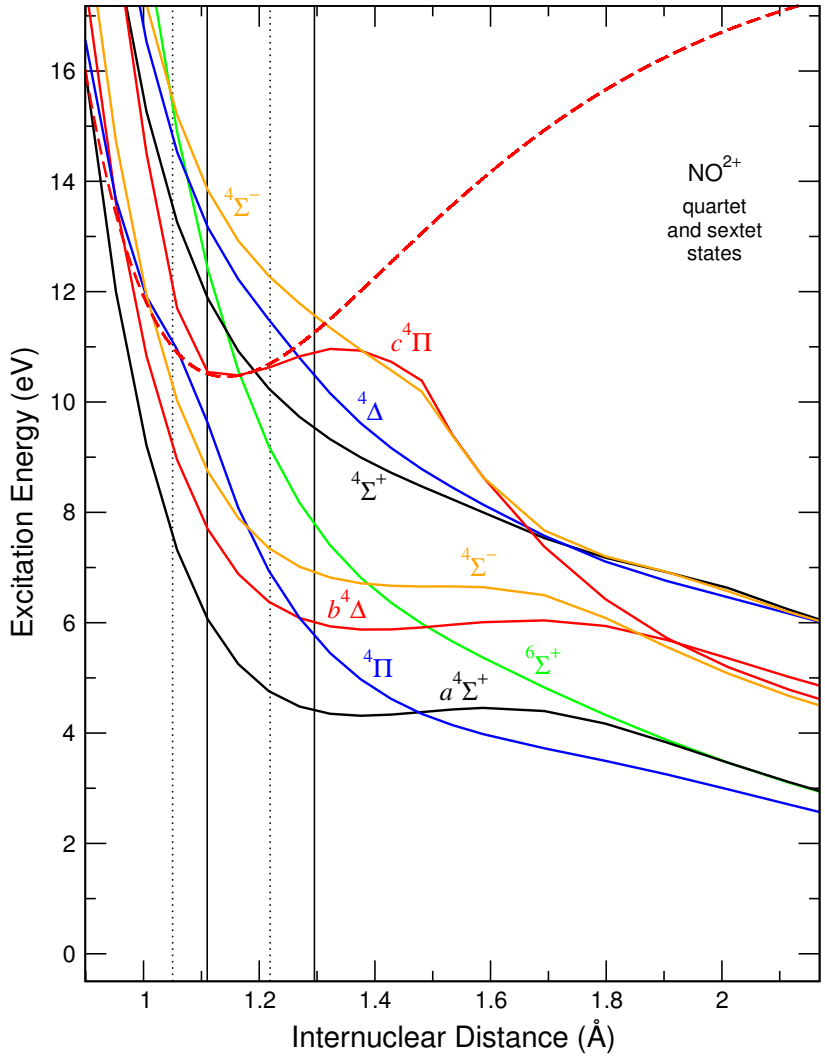

Figure 3.7: Theoretical potential-energy curves of the quartet and the sextet states from Ref. [76] as well as Morse-potential-energy curve of one of these states derived from the present fit analysis. For a description of the lines see Figure 3.6.

In our fit analysis we also allowed for a possible spin-orbit splitting of the dicationic state $A^2\Pi$ into two components with magnetic total angular momenta $\Omega = 1/2$ and $\Omega = 3/2$, assuming identical intensities of the two Auger transitions. However, no spin-orbit splitting significantly different from zero resulted from the fit analysis. Taking into account the error bars of the present experimental data, we consider a value of 13 meV as an upper limit for such a splitting; this value is in good agreement with the theoretical result from Ref. [76] that predicts a spin-orbit

splitting of 7.4 meV.

Auger transitions
O $1s^{-1} \rightarrow B^2\Sigma^+$
N $1s^{-1} \rightarrow B^2\Sigma^+$

As in case of the dicationic state $X^2\Sigma^+$, the fit analysis of the present data did not result in a reasonable value for the anharmonicity $x\hbar\omega$ of the dicationic state $B^2\Sigma^+$. We, therefore, used in the fit analysis a fixed value of 9.39 meV for the anharmonicity as derived by Dawber *et al.* [69]. In this way we obtained an equilibrium distance of $R_e = 1.085(1)$ Å. As in the case of the dicationic state $X^2\Sigma^+$, we can compare this result with the value of R_0 reported by Cossart *et al.* [66, 67] following the procedure described above, see page 55. In this way we obtain for the dicationic state $B^2\Sigma^+$ perfect agreement between the two distances with $\alpha_e = 0.082$ cm^{-1}, a value that agrees reasonably well with $\alpha_e = 0.05$ – 0.09 cm^{-1} given by Cossart *et al.* [66, 67]. However, the present difference of $\Delta\alpha_e = \alpha_e(B^2\Sigma^+) - \alpha_e(X^2\Sigma^+) = 0.067$ cm^{-1} is larger than the value of $0.030(12)$ cm^{-1} reported for the same quantity by Cossart *et al.* [66, 67].

The obtained values for α_e can be checked independently by applying the empirical rule given by Herzberg [85] according to which the ratio α_e/B_e is comparable with the ratio $x\hbar\omega/\hbar\omega$. With the present values we obtain $\alpha_e/B_e = 0.0079$ and $x\hbar\omega/\hbar\omega = 0.0098$ for the dicationic state $X^2\Sigma^+$ as well as $\alpha_e/B_e = 0.0436$ and $x\hbar\omega/\hbar\omega = 0.0422$ for the dicationic state $B^2\Sigma^+$. This tells us that the differences between the present values for R_e and the values for R_0 reported by Cossart *et al.* [66, 67] have its origin mainly in the different physical meaning of these two parameters; we estimate 1 mÅ as an upper limit for the error bars of the reported values of R_e, a value that agrees well with error bars estimated by the method described above, see page 48.

The present equilibrium distance $R_e = 1.085(1)$ Å agrees well with the theoretical value of 1.0881 Å reported in Ref. [76]. The vibrational energy of the dicationic state $B^2\Sigma^+$ derived from the fit analysis $\hbar\omega = 222.1(1)$ meV is also in reasonable agreement with the experimental values of 220 meV and 224.22 meV reported by Eland *et al.* [70] and Dawber *et al.* [69], respectively, as well as with the theoretical result of 211.55 meV given by Pettersson *et al.* [68, 73].

Auger transition
N $1s^{-1} \rightarrow C^2\Sigma^+$

The two dicationic states with potential-energy minima at 8.757(4) eV and 10.458(6) eV above that of the ground state $X^2\Sigma^+$ of NO^{2+} have not been reported before. The assignment of these two states is based on the theoretical results presented in Ref. [76], see Figures 3.6 and 3.7. A comparison of the theoretical potential-energy curves of the dicationic states $X^2\Sigma^+$, $A^2\Pi$, and $B^2\Sigma^+$ with those derived from the present experiment is shown in Figure 3.6; it reveals excellent agreement in the Franck-Condon region. We were, therefore, confident that these calculations provide also reliable results in the excitation-energy region around 10 eV.

For the dicationic state with a potential-energy minimum of $\Delta E_e = 8.757(4)$ eV above that of the ground state of NO^{2+}, an equilibrium distance $R_e = 1.205(2)$ Å, a vibrational energy $\hbar\omega = 215(1)$ meV, and an anharmonicity $x\hbar\omega = 0.7(7)$ meV are found from the fit analysis. The last value is quite small, probably due to the complex background. Both the obtained energy position and the equilibrium distance agree quite well with the theoretical results of $\Delta E_e = 8.8736$ eV and $R_e = 1.2220$ Å for the dicationic state $C^2\Sigma^+$ reported in Ref. [76], *i.e.*, according to these calculations, with the parameters of the only metastable dicationic state in this energy region. The present result of 214(2) meV for the splitting between the two lowest vibrational substates, see eqn. 1.16, agrees reasonably well with the theoretical result of 192.5 meV from Ref. [76]. The calculated potential barrier height of 318.5 meV, however, suggests the existence of only two vibrational substates, a result that is clearly in contradiction with the experimentally observed progression that consists of at least four vibrational levels. In summary, the calculations reported in Ref. [76] reproduce the experimental potential-energy curve quite well, even though they seem to underestimate the potential barrier height.

In the Auger spectrum subsequent to N $1s^{-1}$ photoionization, we observe an intensity ratio of 1 to 3.2(1) for Auger decays originating from the core-ionized states $^1\Pi$ and $^3\Pi$, see Table 3.5, *i.e.* a value that is close to the ratio of the statistical weights of the corresponding spins. This finding is in agreement with an assignment of the transition to the dicationic state $C^2\Sigma^+$, since the observed intensity ratio is only expected for doublet states. On the other hand, for a quartet state, we expect only the $^3\Pi$ component to be intense, since a transition from a singlet to a quartet state can only take place when a spin-flip is involved. Hence, the intensity of such processes is expected to be very low.

Auger transition N $1s^{-1} \rightarrow c^4\Pi$

The dicationic state $c^4\Pi$ is clearly identified on the basis of its excitation energy $E_e = 10.458(6)$ eV. In this case, a Franck-Condon analysis of the corresponding Auger transition is not possible, since only one vibrational substate is observed in the spectrum. For a simulation of the vibrational progression, we therefore use the calculated equilibrium distance $R_e = 1.1388$ Å presented in Ref. [76], see Figure 3.7, as well as the vibrational energy and the anharmonicity of the ground state; for reasons given below, the calculation used in Ref. [76] did not allow us to obtain values for the last two parameters. The results of this simulation are in full agreement with the experimental spectrum, see Figure 3.4, and the derived potential-energy curve agrees well with the calculated one within the Franck-Condon region of the N $1s^{-1}$ Auger decay, see Figure 3.7. For bond distances larger than 1.22 Å, the actual potential-energy curve differs considerably from a Morse potential. As a consequence, we were not able to construct a Morse potential on the basis of the theoretical energy

Table 3.5: Branching ratios of the Auger transitions to the metastable states derived from the fit analysis of the Auger spectra of the NO molecule subsequent to O $1s^{-1}$ and N $1s^{-1}$ photoionizations. Branching ratios are given relative to the transitions $^3\Pi \rightarrow X^2\Sigma^+$. Theoretical values reported by Ågren [83] are included for comparison.

state	O $1s^{-1}$ AES				N $1s^{-1}$ AES			
	present work		[83]		present work		[83]	
	$^1\Pi$	$^3\Pi$	$^1\Pi$	$^3\Pi$	$^1\Pi$	$^3\Pi$	$^1\Pi$	$^3\Pi$
$X^2\Sigma^+$	0.000	1	0.138	1	0.2114(9)	1	0.139	1
$A^2\Pi$	1.48(1)	4.46(5)	0.436	1.745	1.34(2)	2.57(3)	0.444	1.319
$B^2\Sigma^+$	0.080(2)	0.384(3)		0.636	0.074(3)	0.427(4)		0.667
$C^2\Sigma^+$					0.141(2)	0.452(7)		
$c^4\Pi$					0.003(1)	0.135(1)		

positions $E_0 = 137.8$ meV and $E_1 = 359.9$ meV for the vibrational sublevel $v = 0$ and $v = 1$, respectively, given in Ref. [76] as well as on the basis of the theoretical potential barrier height of 531.4 meV. The intensity of the transition N $1s^{-1}$ $^1\Pi \rightarrow c^4\Pi$ is zero, see Table 3.5, which is an additional argument for the correctness of the present assignment, see above.

Auger intensities The relative experimental and theoretical Auger intensities of the transitions to the five metastable dicationic states investigated in this study are presented in Table 3.5. The experimental and theoretical values for the relative Auger intensities agree qualitatively in their main tendencies and show that the $^3\Pi$ to $^1\Pi$ intensity ratio for a particular dicationic state can be substantially different from 3, *i.e.* from the statistical weights of the core-ionized states. This is fully in line with different values of the lifetime widths of the $^1\Pi$ and the $^3\Pi$ core-ionized states, see page 51. The largest disagreement between experiment and theory is observed in the intensities of the transitions to the dicationic state $A^2\Pi$. In the present fit analysis, the transitions to this state are more intense in both the O $1s^{-1}$ and the N $1s^{-1}$ Auger spectra than those calculated by Ågren [83].

Background The Auger spectra in Figures 3.3 and 3.4 exhibit a number of broad spectral features that are included in the background. The most pronounced spectral features are observed in the Auger spectrum subsequent to N $1s^{-1}$ photoionization at kinetic energies of approximately 375 eV and 363 eV. The weak structure at a kinetic energy of approximately 375 eV is due to shake-up Auger satellite transitions and is described by a Gaussian line. This structure has also been reported by Moddeman *et al.* [86] and by Pettersson *et al.* [68]. From the potential-energy curves presented in Figures 3.6 and 3.7 we notice a set of dis-

sociative final states around an excitations energy of 10.5 eV. Auger transitions to these states should result in broad spectral features in the Auger spectrum at kinetic energies of approximately 363 eV and are described in the fit model also by means of Gaussian lines, see Appendix A.

Summary

In the Auger spectra of the NO molecule analyzed in this study, transitions with vibrational progressions indicating five metastable dicationic states were observed. The transitions to the three dicationic states $X^2\Sigma^+$, $A^2\Pi$, and $B^2\Sigma^+$ were identified on the basis of previous experimental and theoretical studies, the transitions to the two hitherto unobserved dicationic states $C^2\Sigma^+$ and $c^4\Pi$ are assigned on the basis of the theoretical results presented in Ref. [76] as well as in the work of Baková *et al.* [32]. The Franck-Condon analysis of the photoelectron spectra was performed by taking into account spin-orbit splitting of the $X^2\Pi$ ground state into the two components $^2\Pi_{1/2}$ and $^2\Pi_{3/2}$. The lifetime broadenings of the various core-ionized states derived from the fit analysis revealed different values for the $^1\Pi$ and the $^3\Pi$ components at both the O 1*s* and the N 1*s* ionization thresholds.

3.2 C $1s^{-1}$ photoelectron and Auger spectra of CO_2

The Auger spectrum of the CO_2 molecule was investigated for the first time by Moddeman *et al.* [86] in the early 1970s. The experimental resolution available in those days was, however, not sufficient to observe the vibrational structure of the transitions to the metastable states. One decade later, this first Auger spectrum was reanalyzed by Ågren [83] using theoretical results. In the late 1990s, Hochlaf *et al.* [87] reported detailed calculations on the potential-energy curves of the lowest dicationic states of this molecule, which are mostly metastable. Recently, Eland [8] and Slattery *et al.* [9] studied these metastable states with the time-of-flight photoelectron-photoelectron-coincidence method as well as with the threshold-photoelectron-coincidence spectroscopy. In these double-ionization spectra, they resolved a number of transitions to dicationic states that exhibit vibrational structures and they were able to derive such spectroscopic quantities as vibrational energies and anharmonicities. The studies of Eland [8] and Slattery *et al.* [9] suggest vibrational progressions in the Auger spectrum of the CO_2 molecule.

A high-resolution Auger spectrum of the CO_2 molecule subsequent to C $1s^{-1}$ photoionization measured at beamline 27SU at SPring-8 in Japan is shown in Figure 3.9; the corresponding photoelectron spectrum is presented in Figure 3.8. All spectra exhibit the expected vibrational progressions. All clearly resolved vibrational states can be assigned to the symmetric stretching vibrational mode.

Details of data analysis

The matrix element of the **L** matrix, which gives the relation between the normal coordinate corresponding to the symmetric stretching vibrational mode and the internuclear distance $R(\mathrm{C-O})$, is calculated in Appendix B, see eqn. B.2. Due to symmetry arguments, this matrix element is identical for all electronic states. Therefore, the transformation equation 1.54 can be rewritten as

$$\Delta R_e(\mathrm{C-O}) = 0.177 \cdot \Delta Q_e,$$

where Q_e is the equilibrium value of the normal coordinate corresponding to the symmetric stretching vibration.

In order to calibrate the binding-energy scale of the photoelectron spectrum, a value of 297.664(1) eV for the C 1*s* binding energy reported by Myrseth *et al.* [88] is used. The calibration of the kinetic-energy scale of the Auger spectrum is performed on the basis of this binding energy as well as the double-ionization energy of 38.52(3) eV for the dicationic state $a^1\Delta_g$ as reported by Eland [8]. In this way an accuracy of 30 meV is obtained for the kinetic-energy scale of the Auger spectrum.

In the fit analysis of the present Auger spectrum, the PCI shift ΔT^P for the vibrational lifetime-interference terms, see Section 1.8, amounts to approximately 13 meV.

Ground state

The electronic configuration of the CO_2 molecule in the ground state is

$$(1\sigma_g^+)^2\ (1\sigma_u^+)^2\ (2\sigma_g^+)^2 \mid (3\sigma_g^+)^2\ (2\sigma_u^+)^2\ (4\sigma_g^+)^2\ (3\sigma_u^+)^2\ (1\pi_u)^4\ (1\pi_g)^4,$$

where the $1\sigma_g^+$ and the $1\sigma_u^+$ orbitals represent the O 1*s* core levels, the $2\sigma_g^+$ orbital the C 1*s* core level, and the remaining six orbitals describe the valence shell of the molecule.

For the description of the ground state in the Franck-Condon analysis we use the following values of the Morse parameters for the observed symmetric stretching vibrational mode: an equilibrium distance $R_e = 1.1615$ Å [89] as well as a vibrational energy $\hbar\omega = 167.71$ meV [90] and an anharmonicity $x\hbar\omega = 0.0001$ meV. In fact, literature provides for this mode a very small negative value for the anharmonicity [90], which actually allows to approximate the anharmonic oscillator by the harmonic one. However, our fit routine is not able to handle anharmonicities equal to zero or negative ones; therefore, we use the very small value, which leads to negligible systematic errors.

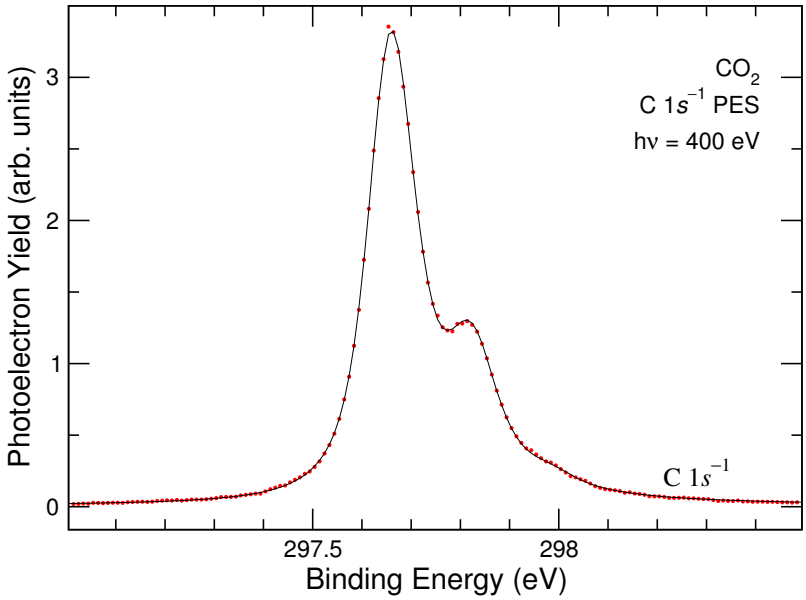

Figure 3.8: C $1s^{-1}$ photoelectron spectrum of the CO_2 molecule measured at a photon energy of 400 eV. The solid line through the data points represents the fit result.

Photoelectron spectrum

The photoelectron spectrum of the CO_2 molecule at the C 1*s* ionization threshold is shown in Figure 3.8. Using the presented values of the Morse parameters for the ground state, we derive in our fit analysis for the C $1s^{-1}$ core-ionized state an equilibrium distance $R_e = 1.1397(3)$ Å, a vibrational energy $\hbar\omega = 165.7(1.0)$ meV, and an anharmonicity $x\hbar\omega = 0.50(20)$ meV. These values agree reasonably well with previous results of $R_e = 1.1403(1)$ Å, $\hbar\omega = 164(1)$ meV, and $x\hbar\omega = 0.20(10)$ meV reported by Hatamoto *et al.* [91].

For the C $1s^{-1}$ core-ionized state lifetime widths Γ of 93(1) meV is derived. This result is in good agreement with the value of 95(2) meV measured by Hatamoto *et al.* [91].

Auger spectrum

Figure 3.9 displays the entire part of the Auger spectrum of the CO_2 molecule subsequent to C $1s^{-1}$ photoionization exhibiting vibrational structure. Figure 3.10 shows the kinetic-energy region from 252.6 eV to 260.7 eV in more detail. The dicationic states of the Auger transitions are mainly assigned on the basis of the theoretical potential-energy curves of Hochlaf *et al.* [87] as well as the assumption that the spectrum is dominated by transitions to singlet dicationic states [92].

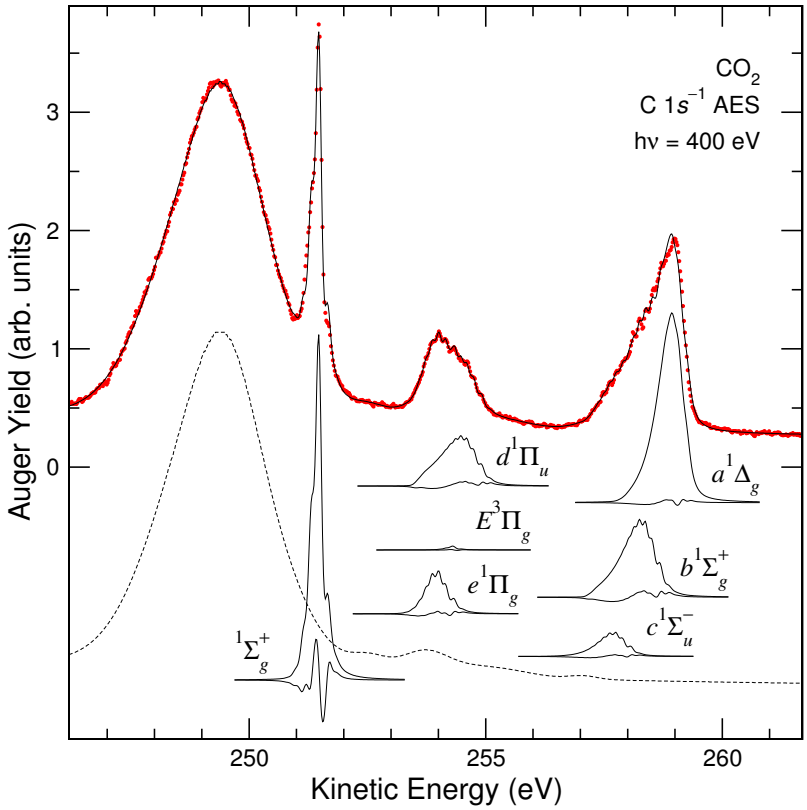

Figure 3.9: Auger spectrum of the CO_2 molecule subsequent to C $1s^{-1}$ photoionization measured at a photon energy of 400 eV in the kinetic-energy region from 246.2 eV to 261.7 eV. The solid line through the data points represents the fit result, and the short-dashed line indicates the background used in the fit analysis. The upper subspectra represent the vibrational progressions of the Auger transitions through the C $1s^{-1}$ core-ionized state to the individual metastable dicationic states, and the lower subspectra the corresponding contributions from the vibrational lifetime interference.

The vibrational progressions observed in the Auger spectrum were subjected to a fit analysis in order to extract detailed information on the corresponding potential-energy curves of the dicationic states. The results for the equilibrium distances R_e, the vibrational energies $\hbar\omega$, and the anharmonicities $x\hbar\omega$ are summarized in Table 3.6. The obtained equilibrium distances agree – with the dicationic state $c^1\Sigma_u^-$ being an exception – reasonably well with the theoretical values of Hochlaf *et al.* [87]. In Table 3.7 the kinetic energies T_0^A and the branching ratios of the observed Auger transitions derived from the fit analysis are also presented. In the following, we discuss the individual transitions in the order of increasing binding energies of the dicationic states, *i.e.* decreasing kinetic energies of the Auger

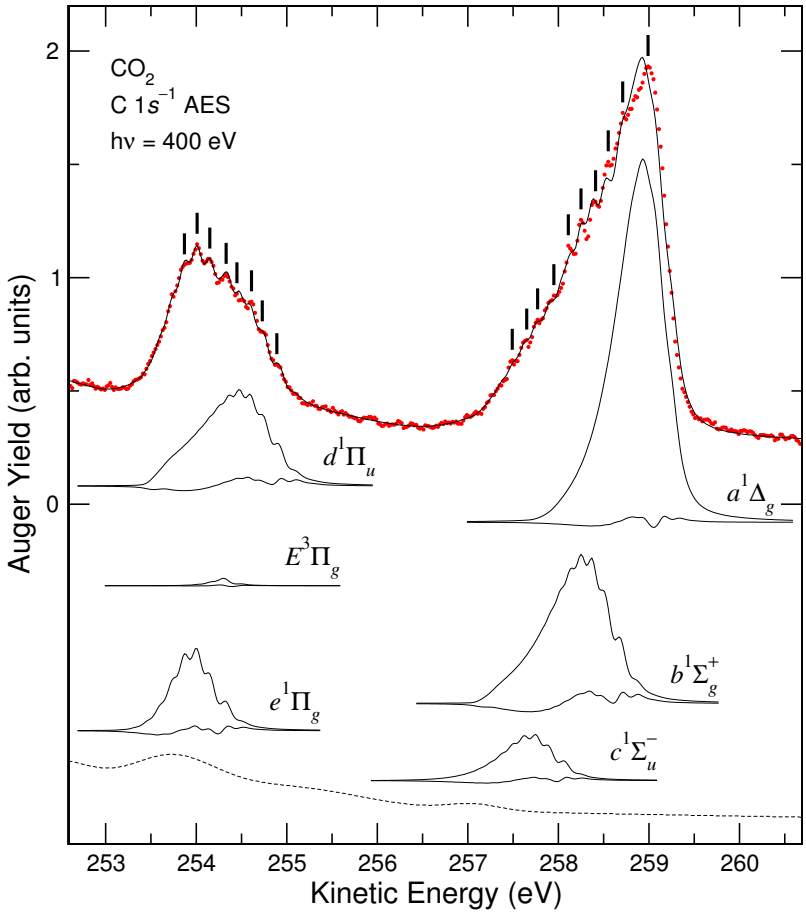

Figure 3.10: Detailed representation of the Auger spectrum and the fit results shown in Figure 3.9 in the kinetic-energy region from 252.6 eV to 260.7 eV. The observed vibrational structure is indicated by the vertical bars.

electrons.

Auger transitions
C $1s^{-1} \rightarrow a^1\Delta_g$
C $1s^{-1} \rightarrow b^1\Sigma_g^+$
C $1s^{-1} \rightarrow c^1\Sigma_u^-$

In contrast to the spectra measured with the time-of-flight photoelectron-photoelectron-coincidence [8] and the threshold-photoelectron-coincidence [9] techniques, Auger transitions to the ground state $X^3\Sigma_g^-$ of CO_2^{2+} are absent in the spectra of the present work. This observation can be explained by the triplet character of the dicationic state and is in full agreement with the results obtained for the CO molecule [15], where triplet states play only a minor role in the Auger spectrum. The peak in the kinetic-energy region from 257 eV to 260 eV shows a structure that can be identified as being caused by three vibrational progressions, which are the results of Auger transitions to the states $a^1\Delta_g$, $b^1\Sigma_g^+$, and

Table 3.6: Equilibrium distances R_e, vibrational energies $\hbar\omega$, and anharmonicities $x\hbar\omega$ of the core-ionized and the metastable dicationic states derived from the fit analyses of the C $1s^{-1}$ photoelectron spectrum and the subsequent Auger spectrum of the CO_2 molecule. Values for the ground state taken from the literature [89, 90] as well as theoretical equilibrium distances for the dicationic states reported by Hochlaf *et al.* [87] are included for comparison.

state	R_e, Å		$\hbar\omega$, meV	$x\hbar\omega$, meV
	present work	[87]		
ground state	1.1615		167.71	0.0001
C $1s^{-1}$	1.1397(3)		165.7(1.0)	0.50(20)
$a^1\Delta_g$	1.1865(5)	1.22	139[a]	3.6(1.0)
$b^1\Sigma_g^+$	1.2002(5)	1.22	138[a]	3.2(1.0)
$c^1\Sigma_u^-$	1.1960(5)	1.27	140[a]	1.8(1.0)
$d^1\Pi_u$	1.2033(5)	1.22	139.6(5)	3.7(1.0)
$E^3\Pi_g$	1.1631(10)	1.16	160[b]	2.6(1.0)
$e^1\Pi_g$	1.1949(5)	1.21	141.5(5)	0.1(1.0)
$^1\Sigma_g^+$	1.1667(5)		169.7(5)	0.0(1.0)

[a] Taken from the work of Slattery *et al.* [9]; fixed in the fit analysis.
[b] Estimated based on the theoretical equilibrium distance reported by Hochlaf *et al.* [87]; fixed in the fit analysis.

Table 3.7: Leading configurations of the metastable dicationic states as well as kinetic energies T_0^A and branching ratios of the corresponding Auger transitions derived from the fit analysis of the Auger spectrum of the CO_2 molecule subsequent to C $1s^{-1}$ photoionization. Branching ratios are given relative to the well-separated transition C $1s^{-1} \rightarrow {}^1\Sigma_g^+$.

state	configuration	T_0^A, eV	branching ratio
$a^1\Delta_g$	$(1\pi_g)^{-2}$	259.110(30)	1.29(13)
$b^1\Sigma_g^+$	$(1\pi_g)^{-2}$	258.487(30)	0.67(7)
$c^1\Sigma_u^-$	$(1\pi_u)^{-1}(1\pi_g)^{-1}$	257.869(30)	0.17(2)
$d^1\Pi_u$	$(3\sigma_u^+)^{-1}(1\pi_g)^{-1}$	254.715(30)	0.49(5)
$E^3\Pi_g$	$(4\sigma_g^+)^{-1}(1\pi_g)^{-1}$	254.300(30)	0.02(1)
$e^1\Pi_g$	$(4\sigma_g^+)^{-1}(1\pi_g)^{-1}$	254.131(30)	0.24(3)
$^1\Sigma_g^+$	$(3\sigma_u^+)^{-2} + (1\pi_u)^{-2}$	251.473(30)	1

$c^1\Sigma_u^-$.

From the studies of Slattery *et al.* [9] it is well known that the dicationic state $a^1\Delta_g$ is metastable with respect to dissociation, since it possesses a vibrational progression in the time-of-flight photoelectron-photoelectron-coincidence and the threshold-photoelectron-coincidence spectra. Both spectra exhibit also contributions from the bending vibrational mode. In addition, in contrast to all other Auger transitions, the transition C $1s^{-1} \rightarrow a^1\Delta_g$ could not be described by excitations of the symmetric stretching vibrational mode only; instead, contributions of the bending vibrational mode were necessary to obtain a good description. This observation gives rise to the assumption that the dicationic state $a^1\Delta_g$ is bent. This lowering of symmetry can be readily explained by a Jahn-Teller distortion caused by the degeneracy of this state, and it is in line with the recent observation of bent states in CO_2^{2+} by Bapat and Sharma [93].

Auger transitions
C $1s^{-1} \rightarrow d^1\Pi_u$
C $1s^{-1} \rightarrow E^3\Pi_g$
C $1s^{-1} \rightarrow e^1\Pi_g$

The spectral features in the kinetic-energy region from 253 eV to 255 eV are decomposed in our fit analysis into three vibrational progressions. The Auger transitions with the highest and lowest kinetic energy exhibit strong vibrational progressions and are assigned to the transitions to the dicationic states $d^1\Pi_u$ and $e^1\Pi_g$, respectively. To obtain a good description of the spectrum, a less intense transition with a short vibrational progression is additionally employed. This short vibrational progression indicates an equilibrium distance close to the value for the C $1s^{-1}$ core-ionized state, and its low intensity indicates a triplet character of the dicationic state. These findings are in good agreement with the theoretical results of Hochlaf *et al.* [87] that predict the dicationic state $E^3\Pi_g$ with a bond distance of approximately 1.16 Å in this energy region.

Auger transition
C $1s^{-1} \rightarrow {}^1\Sigma_g^+$

The narrow and intense spectral feature at 251.5 eV exhibits a relatively large vibrational splitting of 169.7(5) meV and a bond distance of 1.1667(5) Å; *i.e.* only slightly larger than of the ground state. In addition, the fit description of this transition is worse than for all other regions of the spectrum. The results of Hochlaf *et al.* [87] provide no information about the character of this state. However, from the high intensity of the transition we conclude that this state has a singlet character. In addition, the relatively poor fit description indicates a stronger deviation from the Morse potential assumed in the fit analysis. This observation as well as the small equilibrium distance can be explained by an avoided level crossing. These findings are in full agreement with the theoretical results of Feyer *et al.* [94], which predict a state with ${}^1\Sigma_g^+$ symmetry in this energy region. This state possesses contributions of two configurations, namely $(3\sigma_u^+)^{-2}$ and $(1\pi_u)^{-2}$, which explains the avoided level crossing and, in the case of the configuration $(3\sigma_u^+)^{-2}$, the small equilibrium distance; note

Table 3.8: Total energies of the metastable dicationic states ΔE_0 relative to the state $a^1\Delta_g$ expressed in eV. Given are the values derived from the present fit analysis, see Table 3.7, the theoretical values reported by Hochlaf *et al.* [87] and the experimental values reported by Slattery *et al.* [9]. The last column displays the energy values of Slattery *et al.* [9] upon revision of the assignments suggested in the present work.

state	present work	[87]	[9]	[9] revised
$X^3\Sigma_g^-$		-1.35	$-1.18(1)$	$-1.18(1)$
$a^1\Delta_g$	0	0	0	0
$b^1\Sigma_g^+$	0.623(3)	0.58	0.64(2)	0.64(2)
$c^1\Sigma_u^-$	1.241(3)	1.20	1.58(10)	
$A^3\Delta_u$		1.80		2.91(1)
$B^3\Sigma_u^+$		1.95		2.91(1)
$C^3\Sigma_u^-$		2.95		3.78(1)
$D^3\Pi_u$		3.00	2.91(1)	4.13(1)/4.30(1) ($v = 1$)
$d^1\Pi_u$	4.395(3)	3.96	3.78(1)	4.30(1)
$E^3\Pi_g$	4.810(3)	4.41	4.13(1)	
$e^1\Pi_g$	4.979(3)	4.67	4.30(1)	

that the $3\sigma_u^+$ orbital has a strong lone-pair character so that two vacancies in this orbital do not lead to a strong increase of the equilibrium distance.

Background The background used in the fit analysis and indicated in Figures 3.9 and 3.10 consists of a number of broad Gaussians structures of various origins, see Appendix A. In the energy region from 252 eV to 258 eV, Hochlaf *et al.* [87] calculated four different triplet states that are all metastable with large equilibrium distances. Therefore, we expect extended vibrational progressions with vibrational energies of less than 140 meV, which are difficult to resolve. In addition, the triplet states are expected to be very weak with a low signal-to-noise ratio, which renders it difficult to observe a possible vibrational structure. Consequently, we assume that weak triplet states with an unresolved vibrational structure cause at least part of the background in the energy region under discussion.

The broad and intense Gaussian structure at a kinetic energy of approximately 249.5 eV in Figure 3.9 is due to Auger transitions to dissociative final states. In this energy region, Ågren [83] calculated intense transitions to four dicationic states of the configurations $(1\pi_u)^{-2}$ (the states $^1\Sigma_g^+$ and $^1\Delta_g$), $(3\sigma_u^+)^{-1}(1\pi_u)^{-1}$ (the state $^1\Pi_g$), and $(4\sigma_g^+)^{-1}(1\pi_u)^{-1}$ (the state $^1\Pi_u$).

Assignment In Table 3.8, the energy positions obtained in the present work as well as those of Hochlaf *et al.* [87] and Slattery *et al.* [9] are given relative to the position of the dicationic state $a^1\Delta_g$. Based on the results presented

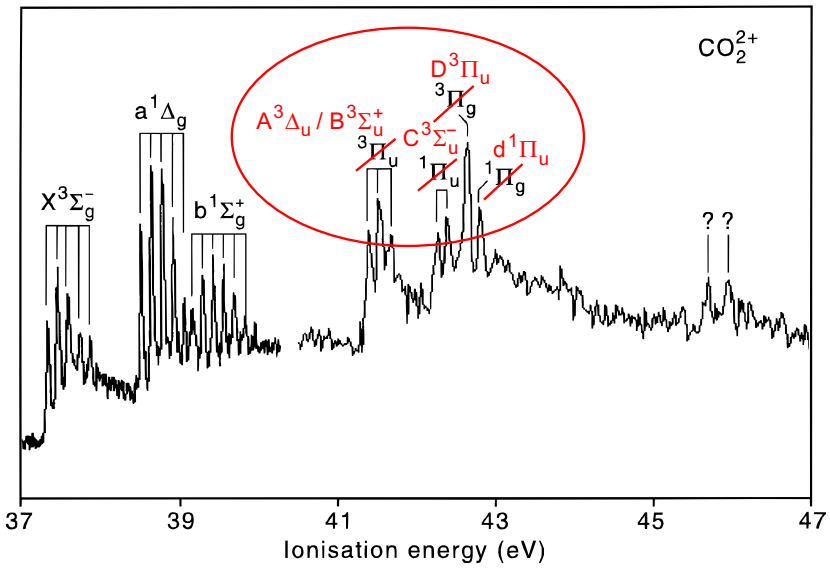

Figure 3.11: Time-of-flight photoelectron-photoelectron-coincidence spectrum of the CO_2 molecule studied by Slattery *et al.* [9] and taken from the work of Eland [8] (with permission from Elsevier © 2003, black lines) with the reassignments of the dicationic states made in the present work (given in red color), see Table 3.8.

in this table, the assignments of the dicationic states $X^3\Sigma_g^-$, $a^1\Delta_g$, $b^1\Sigma_g^+$, and $c^1\Sigma_u^-$ are unambiguous. However, for all other states the energies of the present studies disagree considerably with those presented by Slattery *et al.* [9]. In particular, the present energies for the states $d^1\Pi_u$, $E^3\Pi_g$, and $e^1\Pi_g$ are by 0.3 to 0.4 eV higher than those calculated by Hochlaf *et al.* [87], and even by 0.6 to 0.7 eV higher than those of Slattery *et al.* [9]. However, the present results are based on the assumption that only transitions to singlet states are strong in the Auger spectrum and the observed potential-energy curves agree reasonably well with the calculated curves. In addition, we want to point out that the tentative assignment given by Slattery *et al.* [9] is only based on the energies given by Hochlaf *et al.* [87] but not on the equilibrium distances. This leads to the fact that the triplet states $A^3\Delta_u$, $B^3\Sigma_u^+$, and $C^3\Sigma_u^-$ calculated by Hochlaf *et al.* [87] are not taken into account in the assignment by Slattery *et al.* [9], although time-of-flight photoelectron-photoelectron-coincidence and threshold-photoelectron-coincidence measurements allow to observe strong contributions of triplet states as can be seen by the observation of the ground state $X^3\Sigma_g^-$ of CO_2^{2+}.

According to Slattery *et al.* [9], the state at 3.78 eV relative to the dicationic state $a^1\Delta_g$ is accompanied by a vibrational excitation with a splitting of 112 meV, *i.e.* much lower than for all other states. This assignment implies a considerably larger equilibrium distance than for all the other states and it agrees well with the

potential-energy curve of the dicationic state $C^3\Sigma_u^-$ calculated by Hochlaf *et al.* [87]. Based on this tentative assignment, we reassign the vibrational progression in the spectra of Slattery *et al.* [9], which starts at 2.91 eV above the dicationic state $a^1\Delta_g$ with a splitting of approximately 130 meV to the dicationic states $A^3\Delta_u$ and/or $B^3\Sigma_u^+$. Note that the calculated splitting between these two states is of similar magnitude as the observed vibrational splitting. Based on this assignment, the relative energies of the dicationic states $A^3\Delta_u$, $B^3\Sigma_u^+$, and $C^3\Sigma_u^-$ are by approximately 1 eV higher than those calculated by Hochlaf *et al.* [87]. Therefore, it seems reasonable to assign the spectral feature observed by Slattery *et al.* [9] at 4.13 eV to the dicationic state $D^3\Pi_u$, and the feature at 4.30 eV to the first vibrational substate. The resulting vibrational energy of 170 meV is high, but not unreasonably high. Nevertheless, an assignment of the spectral feature at 4.30 eV to the dicationic state $d^1\Pi_u$ cannot be excluded. The discussed double-ionization spectrum of the CO_2 molecule reported by Slattery *et al.* [9] with the indicated reassignments of the dicationic states suggested in the present work is shown in Figure 3.11.

Summary

The Franck-Condon analysis applied in this study to the CO_2 molecule allowed us to reveal Auger transitions to seven metastable dicationic states. Six of these states were assigned by relating the present results to theoretical potential-energy curves as presented by Hochlaf *et al.* [87]; the resulting assignment disagrees partially with previous results of Eland [8] and Slattery *et al.* [9]. The seventh state is assigned using the calculations of Feyer *et al.* [94], which focus mainly on the low kinetic-energy part of the spectrum.

3.3 S $2p^{-1}$ photoelectron and Auger spectra of OCS

The Auger spectrum of the OCS molecule subsequent to S $2p^{-1}$ photoionization had been studied before by Carroll *et al.* [95]. More recently, Bolognesi *et al.* [96] reported a *photoelectron-Auger-electron-coincidence* spectrum, while Kaneyasu *et al.* [97] presented the results of *Auger-electron-ion-coincidence* measurements. These three publications, however, are limited by relatively moderate energy resolution of the Auger spectra. Complementary calculations of the Auger spectrum had been reported by Carroll *et al.* [95] and by Minelli *et al.* [98]. On the other hand, several studies exist of resonant Auger spectrum [99, 100, 101] as well as of resonant X-ray fluorescence spectra of this molecule [101, 102, 103]. In this context, a core-excited state of the sulphur atom with an exceptionally long core-hole lifetime had been observed [101, 102].

The high-resolution Auger spectrum of the OCS molecule subsequent to S $2p^{-1}$

photoionization measured at beamline I411 at Max II in Sweden is presented in Figure 3.13; the corresponding photoelectron spectrum is shown in Figure 3.12. For the fit analysis the Auger spectrum was divided into three energy regions; they are shown in Figures 3.14, 3.16, and 3.18, respectively. All spectra exhibit vibrational progressions as well as transitions between states with vibrational energies corresponding to the C−O and the C−S stretching vibrational modes.

The spectra were measured at three photon energies, namely 200 eV, 220 eV, and 240 eV, since in the Auger spectra of the molecules HBr/DBr [12], HCl/DCl [13], and H_2S [14] intensities of some narrow lines were found to depend on photon energy. These lines originate from Auger processes resulting from shake-up and shake-off transitions in the photoionization process or from doubly excited states. The present procedure of measuring at three different photon energies was performed to identify similar contributions to the Auger spectrum of the OCS molecule. However, no clear evidence for such processes was found.

Details of data analysis

The **L** matrix for the electronic ground state of the OCS molecule that describes the mentioned modes is calculated in Appendix B, see eqn. B.1. Since the **L** matrix in this case is different for all electronic states, we estimated the error bars using the **L** matrix for the electronic ground state as well as the **L** matrices for the three lowest metastable dicationic states, namely $\tilde{X}^3\Sigma^-$, $\tilde{a}^1\Delta$, and $\tilde{b}^1\Sigma^+$, as calculated by Hochlaf [104]. Thus, the transformation equation 1.54 can be rewritten as

$$\begin{bmatrix} \Delta R_e(\mathrm{C{-}O}) \\ \Delta R_e(\mathrm{C{-}S}) \end{bmatrix} = \begin{bmatrix} 0.378(4) & -0.04(3) \\ -0.25(2) & -0.23(2) \end{bmatrix} \cdot \begin{bmatrix} \Delta Q_{e1} \\ \Delta Q_{e2} \end{bmatrix}, \tag{3.3}$$

where Q_{e1} and Q_{e2} are the equilibrium values of the normal coordinates corresponding to the C−O and the C−S stretching vibrational modes, respectively. Taking the large error bars of the matrix elements into account, we report not only the equilibrium distances R_e(C−O) and R_e(C−S) but also the changes of the equilibrium values of the normal coordinates upon an electronic transition ΔQ_{e1} and ΔQ_{e2}, see Table 3.10. These values are much more accurate and allow one to repeat the transformation into real space using an improved **L** matrix that could be obtained by more sophisticated calculations.

In order to calibrate the binding-energy scales of the photoelectron spectra, a value of 171.93(3) eV for the S $2p_{1/2}$ binding energy reported by Coville *et al.* [105] is used. The calibration of the kinetic-energy scales of the Auger spectra is performed on the basis of this binding energy as well as the double-ionization energy of 37.76(3) eV for the dicationic state $2^1\Pi$ reported by Eland [8]. This spectral feature could be related to lines in the present Auger spectra – independent of the assignment – by comparing the present experimental energy separation of the states

assigned to $2^1\Pi$ and $2^3\Pi$ as well as the splitting of the latter state by approximately 40 meV, see Table 3.13, with the corresponding values reported by Eland [8]. In this way an accuracy of 60 meV is obtained for the kinetic-energy scale of the Auger spectrum.

In the fit analysis of the Auger spectrum measured at a photon energy of 200 eV {220 eV, 240 eV}, the PCI shift ΔT^P for the vibrational lifetime-interference terms, see Section 1.8, amounts to approximately 12 meV {7 meV, 4 meV} for all three kinetic-energy regions, see page 79.

Calculations of our colleagues

The assignment of the dicationic states of the OCS molecule performed in the present work is mainly based on calculations. For this purpose we used new calculations for the Auger spectrum performed by Prof. Dr. Reinhold Fink and his group at the University of Tübingen, Germany, that take into account spin-orbit and molecular-field splitting as well as the various orientations of the three S $2p^{-1}$ core-ionized states [106, 107, 108, 109]. The calculations of the Auger energies and the transition rates were performed interactively with the present data analysis by using the experimental internuclear distances $R(\mathrm{C{-}O) = 1.124}$ Å and $R(\mathrm{C{-}S) = 1.581}$ Å for the S $2p^{-1}$ core-ionized state; these values were derived for the first time from the present S $2p^{-1}$ photoelectron spectrum of the OCS molecule, see below. The theoretical spectra resulted in different intensity ratios for the Auger transitions and, therefore, were very helpful in the assignment process. These calculations were published together with our experimental results, which are being discussed in the present section. Therefore, in the following, when we refer to these calculations, we give a reference to our joint paper [110]. The results of the calculations are also presented in Table 3.9 and Figure 3.13. More details about these calculations can be found in Ref. [110].

Ground state

The electronic configuration of the OCS molecule in the ground state is

$$1\sigma^2\,2\sigma^2\,3\sigma^2\,4\sigma^2\,5\sigma^2\,1\pi^4 \mid 6\sigma^2\,7\sigma^2\,8\sigma^2\,2\pi^4\,9\sigma^2\,3\pi^4,$$

where the orbitals 1σ, 2σ, 3σ, and 4σ represent the core levels S $1s$, O $1s$, C $1s$, and S $2s$, respectively, the 5σ and the 1π orbitals result from molecular-field splitting of the S $2p$ core level (in this description the spin-orbit splitting of the S $2p$ core level is neglected), and the remaining six orbitals describe the valence shell of the molecule.

To describe the ground state in the Franck-Condon analysis, we use the following values of the Morse parameters [111]: the C−O stretching vibrational mode is

Table 3.9: Leading configurations of the dicationic states as well as kinetic energies of the corresponding Auger transitions ΔT_e^A and Auger-transition rates for the different core-ionized states derived from the calculations presented in Ref. [110]. For each state the contribution of the leading configuration is indicated by changes (in %) relative to the ground-state configuration of the OCS molecule. Kinetic energies are presented relative to the Auger transition S $2p^{-1} \rightarrow \tilde{X}^3\Sigma^-$.

state	label	configuration	%	ΔT_e^A, eV	intensity, 10^{-6} au		
					S $2p_{1/2}^{-1}$	S $2p_{3/2,1/2}^{-1}$	S $2p_{3/2,3/2}^{-1}$
$\tilde{X}^3\Sigma^-$	*a*	$3\pi^{-2}$	90.13	0	267.21	204.06	471.27
$\tilde{a}^1\Delta$	*b*	$3\pi^{-2}$	87.75	1.003	278.98	219.00	472.80
$\tilde{b}^1\Sigma^+$	*c*	$3\pi^{-2}$	84.44	1.503	149.89	117.40	254.88
$1^1\Sigma^-$		$2\pi^{-1}3\pi^{-1}$	84.99	3.574	0.03	0.02	0.05
$1^3\Delta$		$2\pi^{-1}3\pi^{-1}$	88.71	3.862	0.18	0.13	0.31
$1^3\Sigma^+$		$2\pi^{-1}3\pi^{-1}$	89.61	3.976	0.10	0.08	0.16
$2^3\Sigma^-$	*d*	$2\pi^{-1}3\pi^{-1}$	69.08	4.546	40.85	31.20	72.05
$1^3\Pi$	*e*	$9\sigma^{-1}3\pi^{-1}$	80.08	5.169	270.88	268.04	280.02
$2^1\Delta$	*f*	$2\pi^{-1}3\pi^{-1}$	68.45	5.573	65.40	51.23	111.20
$1^1\Pi$	*g*	$9\sigma^{-1}3\pi^{-1}$	49.41	6.096	88.42	86.42	94.90
$2^1\Sigma^+$	*h*	$2\pi^{-1}3\pi^{-1}$	68.65	6.256	39.40	30.98	66.60
$2^3\Pi$	*i*	$8\sigma^{-1}3\pi^{-1}$	76.10	6.672	79.22	72.48	101.02
$2^1\Pi$	*j*	$8\sigma^{-1}3\pi^{-1}$	38.91	7.410	93.78	85.76	119.76
$^1\Sigma^-$		$3\pi^{-3}4\pi^{+1}$	61.38	8.255	0.01	0.00	0.01
$^3\Delta$		$3\pi^{-3}4\pi^{+1}$	57.30	8.256	0.03	0.01	0.04
$^3\Sigma^+$		$3\pi^{-3}4\pi^{+1}$	60.91	8.386	0.00	0.00	0.00
$^3\Sigma^-$		$2\pi^{-1}3\pi^{-2}4\pi^{+1}$	93.24	8.527	0.32	0.25	0.57
$^3\Delta$		$2\pi^{-1}3\pi^{-2}4\pi^{+1}$	92.15	8.798	0.00	0.00	0.00
$^3\Pi$	*k*	$2\pi^{-1}9\sigma^{-1}$	74.15	9.387	37.52	34.84	46.14
$^3\Sigma^+$		$2\pi^{-1}3\pi^{-2}4\pi^{+1}$	96.52	9.394	0.00	0.00	0.00
$^3\Sigma^+$		$2\pi^{-1}3\pi^{-2}4\pi^{+1}$	93.48	9.809	0.00	0.00	0.00
$^3\Delta$		$2\pi^{-1}3\pi^{-2}4\pi^{+1}$	96.01	9.970	0.00	0.00	0.00
$^3\Gamma$		$2\pi^{-1}3\pi^{-2}4\pi^{+1}$	97.71	9.985	0.00	0.00	0.00
$^1\Delta$		$2\pi^{-1}3\pi^{-2}4\pi^{+1}$	94.39	9.990	0.59	0.46	1.00
$^3\Sigma^-$		$2\pi^{-2}$	60.76	10.069	0.40	0.31	0.71
$^1\Sigma^+$		$2\pi^{-1}3\pi^{-2}4\pi^{+1}$	95.07	10.409	0.43	0.37	0.65
$^1\Pi$	*l*	$2\pi^{-1}9\sigma^{-1}$	55.90	10.424	95.00	87.60	118.92
$^1\Sigma^+$	*m*	$8\sigma^{-1}9\sigma^{-1}$	51.99	11.014	16.22	20.79	1.44
$^3\Pi$	*n*	$2\pi^{-1}9\sigma^{-1}3\pi^{-1}4\pi^{+1}$	57.80	14.352	13.06	11.02	19.72
$^1\Sigma^+$	*o*	$9\sigma^{-2}$	54.38	15.164	143.90	177.67	34.83

described by a vibrational energy $\hbar\omega_1 = 257.13$ meV and an anharmonicity $x_1\hbar\omega_1 = 1.4321$ meV, and the C−S stretching vibrational mode by a vibrational energy $\hbar\omega_2 = 107.77$ meV and an anharmonicity $x_2\hbar\omega_2 = 0.496$ meV. Equilibrium distances used in the data analysis are R_e(C−O) = 1.157 Å and R_e(C−S) = 1.560 Å.

Photoelectron spectrum

As mentioned above, the photoelectron spectra and the subsequent Auger spectra, see page 79, of the OCS molecule measured at photon energies of 200 eV, 220 eV, and 240 eV revealed no significant photon-energy dependence. Furthermore, the fit results obtained for the three different excitation energies turned out to be identical within the estimated error bars. Therefore, the values of the fit parameters presented in this section are average values obtained for the three photon energies. The quoted error bars are based on the scattering of the values obtained for the different photon energies but not on the statistical error bars resulting from the fit procedure; the latter values are unphysically small, since they are not taking into account small insufficiencies of the fit model like, for example, the fact that vibrational modes, which are not clearly observed, have been omitted (for example, the C−S stretching vibrational mode in the photoelectron spectrum, see page 78).

The photoelectron spectrum of the OCS molecule at the S $2p$ ionization threshold measured at a photon energy of 200 eV is shown in Figure 3.12. Due to spin-orbit interaction and molecular-field splitting, the three well-known core-ionized states S $2p^{-1}_{1/2}$, S $2p^{-1}_{3/2,1/2}$, and S $2p^{-1}_{3/2,3/2}$ are observed. In the first fit approach, we assumed different potential-energy surfaces for these three states. However, we found no significant differences in values of the fit parameters and, therefore, we use identical potential-energy surfaces for all three states in our analysis reducing the CPU-time considerably. The high quality of the fit result shown in Figure 3.12 demonstrates that one vibrational progression for each core-ionized state is sufficient to describe the spectrum well.

A comparison with the well-known vibrational energies of the ground state of the OCS molecule, see above, shows that the vibrational progressions in the photoelectron spectrum correspond to the C−O stretching vibrational mode. We, therefore, use the Morse parameters for this normal mode of vibrations for a description of the ground state in the fit analysis of the photoelectron spectrum. In this way, we obtain a vibrational energy of $\hbar\omega_1 = 280.8(4)$ meV and an anharmonicity of $x_1\hbar\omega_1 = 1.3(1)$ meV for the S $2p^{-1}$ core-ionized state. The result for $\hbar\omega_1$ is in reasonable agreement with the value of $\hbar\omega_1 = 290.39$ meV calculated by Siggel *et al.* [112]. From the vibrational energy and the anharmonicity we obtain a splitting of $278.2(5)$ meV between the first two vibrational sublevels of the S $2p^{-1}$ core-ionized states, a value that agrees well with the previous experimental result of 279 meV by Kukk *et al.* [113].

For the three core-ionized states S $2p^{-1}_{1/2}$, S $2p^{-1}_{3/2,1/2}$, and S $2p^{-1}_{3/2,3/2}$, lifetime widths Γ of $61(2)$ meV, $64(2)$ meV, and $68(2)$ meV, respectively, are derived. The slight differences can be qualitatively understood by the well-known dependence of the Auger-transition rate and hence of the lifetime broadening on the orienta-

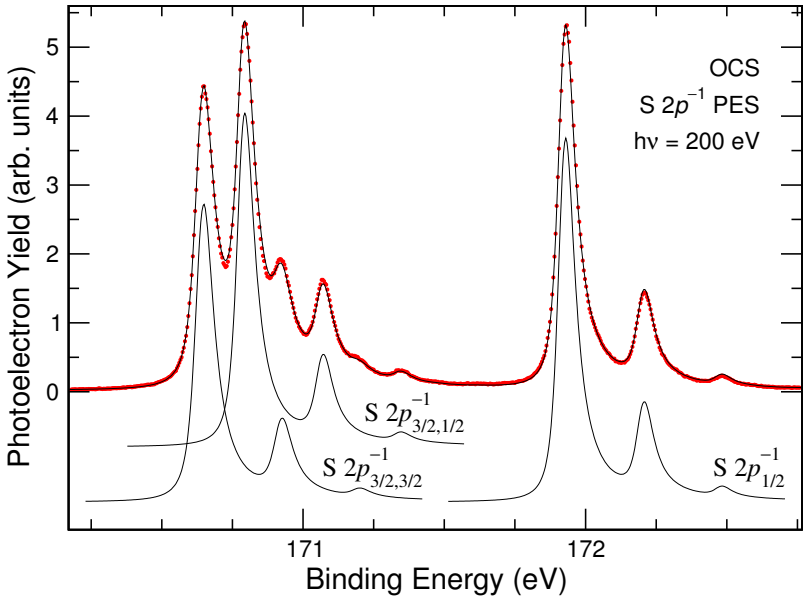

Figure 3.12: S $2p^{-1}$ photoelectron spectrum of the OCS molecule measured at a photon energy of 200 eV. The solid line through the data points represents the fit result. The three subspectra result from transitions to the spin-orbit and the molecular-field split core-ionized states.

tion of the core hole [109, 114, 115]. As reported by Kosugi and Ishida [116], the S $2p^{-1}_{3/2,3/2}$ core hole is π-oriented ($2p\pi^{-1}$, *i.e.* a hole in the 1π orbital). In contrast to this, the S $2p^{-1}_{1/2}$ core hole has 57% π-orientation and 43% σ-orientation, while the S $2p^{-1}_{3/2,1/2}$ core hole has 43% π-orientation and 57% σ-orientation ($2p\sigma^{-1}$, *i.e.* a hole in the 5σ orbital). These theoretical values are confirmed by the present study of the Auger spectrum, see page 96. Assuming a higher Auger-transition rate for a $2p\pi^{-1}$ core hole as compared to a $2p\sigma^{-1}$ core hole and considering the similar orientations of the core holes S $2p^{-1}_{1/2}$ and S $2p^{-1}_{3/2,1/2}$ (both are roughly 50% $2p\sigma^{-1}$ and 50% $2p\pi^{-1}$), we can understand qualitatively that their lifetime broadenings are rather similar, while the lifetime broadening of the S $2p^{-1}_{3/2,3/2}$ core hole (100% $2p\pi^{-1}$) is larger, see eqn. 1.26.

The calculations reported in Ref. [110] give a lifetime widths of 77 meV for the S $2p\pi^{-1}$ core hole and of 34 meV for the S $2p\sigma^{-1}$ core hole resulting in lifetime widths of 59 meV, 52 meV, and 77 meV for the core-ionized states S $2p^{-1}_{1/2}$, S $2p^{-1}_{3/2,1/2}$, and S $2p^{-1}_{3/2,3/2}$, respectively. The calculated differences are clearly too large, but they correctly predict the similarities of the broadenings of the core holes S $2p^{-1}_{1/2}$ and S $2p^{-1}_{3/2,1/2}$, while that of the S $2p^{-1}_{3/2,3/2}$ core hole is larger; this is in qualitative agreement with observation. On the other hand, we can derive from the known core-hole

orientations and the measured lifetime widths of the spin-orbit and the molecular-field split core-ionized states lifetime widths of 68(2) meV for the S $2p\pi^{-1}$ core hole and of 58(4) meV for the S $2p\sigma^{-1}$ core hole, respectively. These values for the lifetime broadening show that the theoretical value for the total $2p\sigma^{-1}$ Auger-transition rate from Ref. [110] is considerably underestimated in comparison to the total $2p\pi^{-1}$ Auger-transition rate. An analogous conclusion can be drawn from the branching ratios of the Auger transitions from different core holes to a given dicationic state, see page 97.

The fit analysis of the present data results in a splitting of 1.1367(5) eV {1.2828(3) eV} between the S $2p^{-1}_{1/2}$ and the S $2p^{-1}_{3/2,1/2}$ {S $2p^{-1}_{3/2,3/2}$} core-ionized states, which is in good agreement with a previous experimental value of 1.1395(5) eV {1.2845(5) eV} reported by Kukk *et al.* [113]. The relative intensities of the core-ionized states S $2p^{-1}_{1/2}$, S $2p^{-1}_{3/2,1/2}$, and S $2p^{-1}_{3/2,3/2}$ derived from the fit analysis are 0.33(1), 0.33(1), and 0.34(1), respectively, and reveal no dependence on photon energy.

The fit of the photoelectron spectrum allowed us to derive the change of the equilibrium value of the normal coordinate associated with an excitation of the C−O stretching vibrational mode ΔQ_{e1}. By applying the transformation equation 3.3, we obtain the following changes of the equilibrium distances: $\Delta R_e(\mathrm{C{-}O) = -0.0330(8)}$ Å and $\Delta R_e(\mathrm{C{-}S) = 0.021(2)}$ Å. These values agree quite well with the result given by Kosugi and Ishida [116]: $\Delta R_e(\mathrm{C{-}O) = -0.041}$ Å and $\Delta R_e(\mathrm{C{-}S) = 0.042}$ to 0.049 Å (the different values for $\Delta R_e(\mathrm{C{-}S)}$ are caused by the different core-ionized states). These results demonstrate that S $2p^{-1}$ ionization causes a decrease in the equilibrium distance $R_e(\mathrm{C{-}O)}$, while the equilibrium distance $R_e(\mathrm{C{-}S)}$ increases. The absolute numbers as well as the different equilibrium distances $R_e(\mathrm{C{-}S)}$ for the various core-ionized states could, however, not be obtained in the present fit analysis.

Possible differences in the equilibrium distances $R_e(\mathrm{C{-}S)}$ can be associated with very weak and, therefore, unobserved excitations of the C−S stretching vibrational mode. From the data analysis we can give an upper limit of 0.01 for the intensity ratio $\frac{I(v''=(00)\rightarrow v'=(01))}{I(v''=(00)\rightarrow v'=(00))}$. This results in an upper limit of 0.007 Å for possible corrections of both equilibrium distances $R_e(\mathrm{C{-}O)}$ and $R_e(\mathrm{C{-}S)}$. Since possible excitations of the C−S stretching vibrational mode can be different for the various core-ionized states, the presented upper limit of such contributions does not exclude differences up to 0.007 Å for the equilibrium distances of the various core-ionized states as predicted by Kosugi and Ishida [116]. Using for the ground state the equilibrium distances given above, see page 74, we obtain $R_e(\mathrm{C{-}O) = 1.124(8)}$ Å and $R_e(\mathrm{C{-}S) = 1.581(9)}$ Å for all core-ionized states. These values were used for the calculations presented in Ref. [110].

Auger spectrum

The upper part of Figure 3.13 presents the S $2p^{-1}$ Auger spectrum of the OCS molecule in the kinetic-energy region from 124.8 eV to 142.8 eV, *i.e.* the region where a previous publication [95] reported medium-resolution spectra with structures of a total width of approximately 1 eV. The theoretical results of Ref. [110] are displayed in the lower part of the figure; here the accuracy of the relative-kinetic-energy positions is estimated to be of the order of 1 eV. Note that the theoretical spectrum is obtained by convoluting all transition rates with a Gaussian of the same width, while the experimental line shapes are different for the individual transitions. Consequently, the peak heights cannot be compared directly. However, the calculated Auger-transition rates turned out to be particularly helpful in assigning dicationic states with peculiar branching ratios in the Auger spectrum, see below.

Contrary to the study of Carroll *et al.* [95], we resolve a number of narrow lines with a total width of approximately 65 meV in the kinetic-energy region from 128 eV to 135 eV. According to spacings of approximately 250 meV, some of these lines – for example, in the region from 129 eV to 132 eV – are assigned to the C−O stretching vibrational mode of different Auger transitions. In addition, we observe splittings of approximately 70 meV in the region from 138 eV to 142 eV as well as of approximately 100 meV in the region from 132 eV to 135 eV; we assigned them to an excitation of the C−S stretching vibrational mode. In total, we observe eight Auger transitions with a vibrational progression, *i.e.* transitions to metastable dicationic states. The information about their potential-energy surfaces derived from the data analysis is summarized in Tables 3.10 and 3.11.

To perform a Franck-Condon analysis of the vibrational progressions, this spectrum was divided into three energy regions that were treated separately. The first region from 137.7 eV to 142.2 eV consists of three dicationic states of the configuration $3\pi^{-2}$. The second region from 131.4 eV to 137.5 eV contains Auger transitions with vibrational progressions to four metastable dicationic states, which are mainly assigned to the configurations $2\pi^{-1}3\pi^{-1}$, $9\sigma^{-1}3\pi^{-1}$, and $8\sigma^{-1}3\pi^{-1}$. The third region from 128.3 eV to 132 eV exhibits Auger transitions to one metastable dicationic state of the configuration $8\sigma^{-1}9\sigma^{-1}$ on top of a rather intense smooth background. In the following, we discuss the three regions separately.

Auger transitions S $2p^{-1} \rightarrow 3\pi^{-2}$

Figure 3.14 shows the Auger spectrum in the kinetic-energy region from 137.7 eV to 142.2 eV as well as the corresponding fit results revealing Auger transitions to the states $\tilde{X}^3\Sigma^-$, $\tilde{a}^1\Delta$, and $\tilde{b}^1\Sigma^+$ that belong all to the configuration $3\pi^{-2}$. This energy region is dominated by vibrational splittings of approximately 65 meV that can be assigned to excitations of the C−S stretching vibrational mode. This mode is clearly visible for the transitions to the dicationic states $\tilde{a}^1\Delta$ and $\tilde{b}^1\Sigma^+$, but it is much less pronounced for

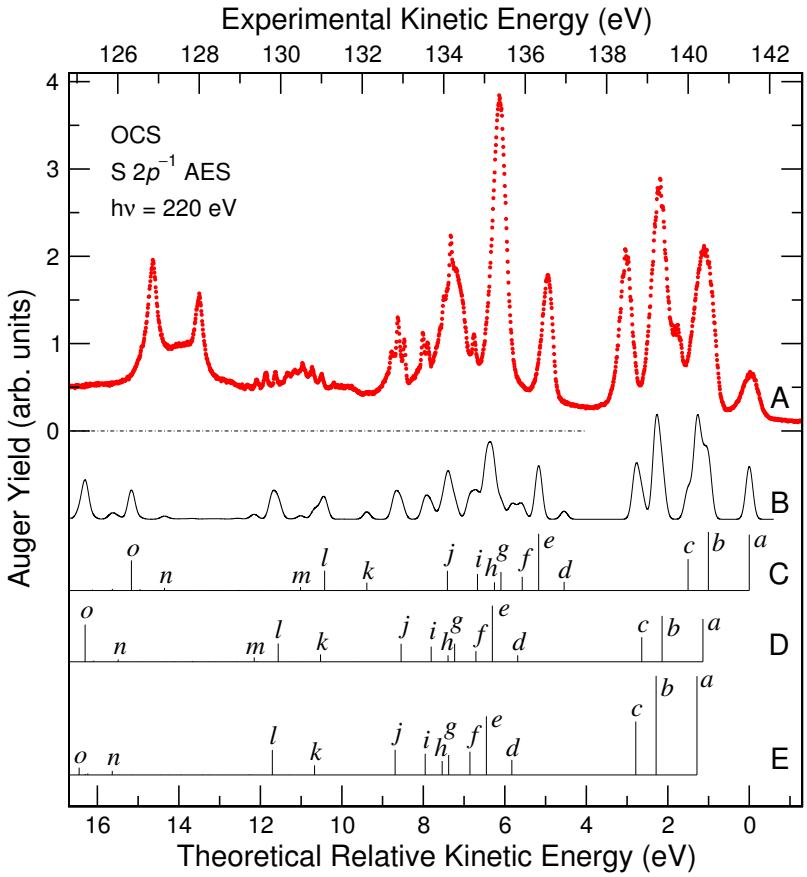

Figure 3.13: Auger spectrum of the OCS molecule subsequent to S $2p^{-1}$ photoionization measured at a photon energy of 220 eV in the kinetic-energy region from 124.8 eV to 142.8 eV (spectrum A, upper energy scale) as well as theoretical Auger spectrum reported in Ref. [110] (spectrum B, lower energy scale). The baseline of the experimental Auger spectrum is indicated by the dash-dotted line. The vertical-bar diagrams C, D, and E indicate the calculated partial Auger spectra originating from the core-ionized states S $2p^{-1}_{1/2}$, S $2p^{-1}_{3/2,1/2}$, and S $2p^{-1}_{3/2,3/2}$, respectively. For a comparison with Table 3.9, Auger transitions to the same state are marked with the same lower-case letters; only intensities $\geqslant 10^{-5}$ au are marked.

the transition to the state $\tilde{X}^3\Sigma^-$. In the last case, only some weak structure with a splitting of 65(5) meV on top of the Auger transition S $2p^{-1}_{1/2} \rightarrow \tilde{X}^3\Sigma^-$ at approximately 141.5 eV is observed. This weak vibrational structure indicates that the dicationic state $\tilde{X}^3\Sigma^-$ is stable with respect to dissociation that is in full agreement with the potential-energy surfaces presented by Brites *et al.* [25] and the experimental observation of OCS^{2+} in coincidence with the Auger transition S $2p^{-1} \rightarrow \tilde{X}^3\Sigma^-$ reported by Kaneyasu *et al.* [97].

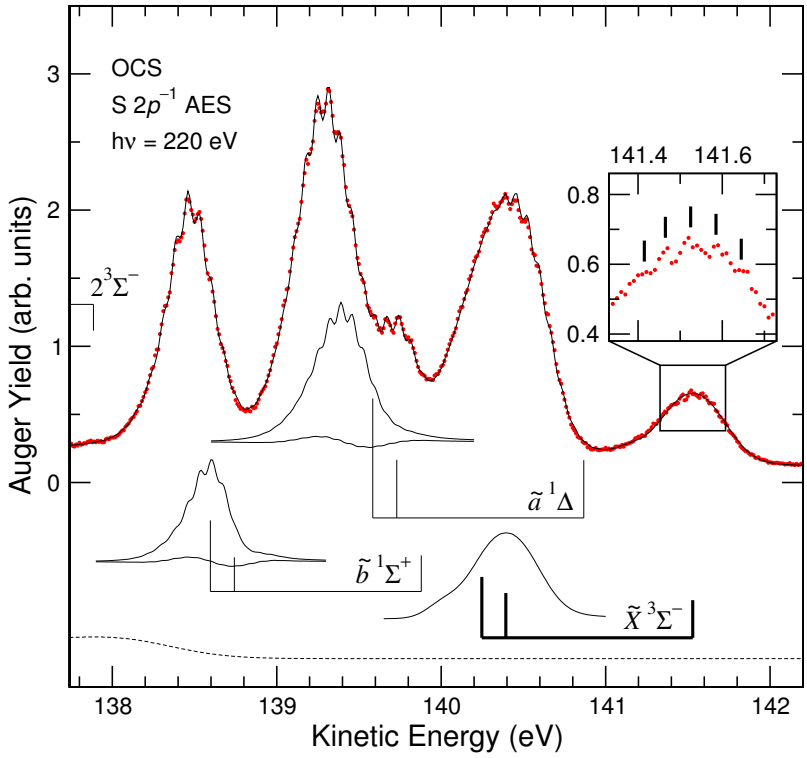

Figure 3.14: Auger spectrum of the OCS molecule subsequent to S $2p^{-1}$ photoionization measured at a photon energy of 220 eV in the kinetic-energy region from 137.7 eV to 142.2 eV. The solid line through the data points represents the fit result, and the short-dashed line indicates the background used in the fit analysis. The up-directed vertical-bar diagrams give the kinetic-energy positions and the relative intensities of the Auger transitions, with the bar at higher {middle, lower} kinetic energy representing the transition through the core-ionized state S $2p^{-1}_{1/2}$ {S $2p^{-1}_{3/2,1/2}$, S $2p^{-1}_{3/2,3/2}$}. The thin up-directed bars mark the kinetic-energy positions of the transitions $v' = (00) \rightarrow v = (00)$, while the bold bars mark the approximate kinetic-energy positions of the peaks. The upper subspectra by the thin up-directed bar diagrams represent the vibrational progressions of the Auger transitions through the S $2p^{-1}_{3/2,1/2}$ core-ionized state to the individual metastable dicationic states, and the lower subspectra the corresponding contributions from the vibrational lifetime interference. The subspectrum by the bold bar diagram displays the peak profile for the transition S $2p^{-1}_{3/2,1/2} \rightarrow \tilde{X}^3\Sigma^-$. The inset displays the weak vibrational progression of the transition S $2p^{-1}_{1/2} \rightarrow \tilde{X}^3\Sigma^-$ with the observed vibrational structure indicated by the vertical bars.

For the Auger transitions S $2p^{-1} \rightarrow \tilde{a}^1\Delta$ and S $2p^{-1} \rightarrow \tilde{b}^1\Sigma^+$, a two-dimensional Franck-Condon analysis was performed, which reveals the presence of the C−O stretching vibrational mode. In contrast to this, we were not able to obtain a reasonable fit for the Auger transition S $2p^{-1} \rightarrow \tilde{X}^3\Sigma^-$ from our Franck-Condon approach.

Because of this, we describe this transition with an empirical lineshape that was derived from the well-separated transition S $2p_{1/2}^{-1} \rightarrow \tilde{X}^3\Sigma^-$, see Figure 3.14.

The fact that the C−S stretching vibrational mode is only weakly pronounced in the Auger transition S $2p^{-1} \rightarrow \tilde{X}^3\Sigma^-$ and that the Franck-Condon analysis failed in this case goes along with the work of Brites *et al.* [25], where these vibrations are completely absent in the time-of-flight photoelectron-photoelectron-coincidence spectrum. For the transition S $2p^{-1} \rightarrow \tilde{a}^1\Delta$, which is described within the Franck-Condon approach in the present work, Brites *et al.* [25] observed a pronounced vibrational progression corresponding to the C−S stretching vibrational mode. This comparison suggests that there is a link between the occurrence of the C−S stretching vibrational mode in the time-of-flight photoelectron-photoelectron-coincidence spectra of Brites *et al.* [25] and the possibility to describe the Auger transitions within a Franck-Condon approach.

Brites *et al.* [25] already excluded the possibility that the C−S stretching vibrational mode can just be masked by a splitting of the dicationic state $\tilde{X}^3\Sigma^-$ into spin-orbit split components $\tilde{X}^3\Sigma_0^-$ and $\tilde{X}^3\Sigma_1^-$, since such a splitting calculated by them is of the order of 1 meV. This result is fully confirmed by the calculations from Ref. [110] resulting in the same value. Brites *et al.* [25] then suggested that an indirect population of this final state by autoionization of excited OCS^{2+}, possible under their experimental conditions, could mask the vibrational progression of the C−S stretching vibrational mode. In the present experimental approach, however, such processes can be excluded. Therefore, we assume that the Auger transition S $2p^{-1} \rightarrow \tilde{X}^3\Sigma^-$ exhibits a complicated and unresolved vibrational structure with contributions of the bending vibrational mode that might be caused by Fano resonances. However, more detailed calculations of the vibrational structure of this transition are necessary to clarify this question.

Since the C−S stretching vibrational mode is not observed in the photoelectron spectrum, we cannot determine the potential-energy surface of the S $2p^{-1}$ core-ionized state correctly. On the other hand, the missing excitations of the C−S stretching vibrational mode in the photoelectron spectrum indicate that upon S $2p^{-1}$ photoionization the potential-energy surface changes along the normal coordinate Q_2 only slightly, namely with $\Delta R_e(\mathrm{C{-}O}) = 0.007$ Å and $\Delta R_e(\mathrm{C{-}S}) = 0.007$ Å being upper limits, see page 78. It allows to estimate the potential-energy surface of the core-ionized state by using the ground-state values for the C−S stretching vibrational mode, see page 74; we use these values in the fit analysis of the Auger spectrum.

The fit analysis treating the vibrational energies of the C−O stretching vibrational mode $\hbar\omega_1$ as free parameters resulted for the two dicationic states $\tilde{a}^1\Delta$ and $\tilde{b}^1\Sigma^+$ in values of approximately 240 meV, which are by 15 to 25 meV smaller than the values calculated by Brites *et al.* [25]. Since these authors predict the vibrational

energies of the C−S stretching vibrational mode very well, see above, and since the excitations of the C−O stretching vibrational mode are not directly observed in the present spectrum, we fixed in our fit analysis the vibrational energies and the anharmonicities of the C−O stretching vibrational mode to the values given by Brites *et al.* [25], obtaining in this way a good description of the spectrum.

The Auger transitions $v' = (00) \rightarrow v = (00)$, which are indicated by the thin vertical-bar diagrams in Figure 3.14, are very weak and obviously not unambiguous, see also Figure 3.15. To check the indicated energy positions, we shifted them by one quantum of the C−S stretching vibrational mode to lower and higher kinetic energies and repeated the fit analysis. However, all these analyses resulted in considerably worse descriptions of the spectral features. The Auger transition S $2p_{3/2}^{-1} \rightarrow \tilde{b}^1\Sigma^+$ overlaps partially with a structure at approximately 137.9 eV included in the background in Figure 3.14; the latter structure is assigned to the transition S $2p_{1/2}^{-1} \rightarrow 2^3\Sigma^-$, see page 89.

Tables 3.10 and 3.11, where values of the Morse parameters derived from the fit analysis are summarized, show that the values for the equilibrium distances R_e(C−O) and R_e(C−S) as well as the values for the vibrational energies of the C−S stretching vibrational mode $\hbar\omega_2$ agree quite well for both dicationic states with those calculated by Brites *et al.* [25]. The fit results for the anharmonicities of the C−S stretching vibrational mode $x_2\hbar\omega_2$ are of the order of several hundredths of meV, *i.e.* much smaller than those predicted theoretically. We do not consider this as a contradiction, since in the present Franck-Condon analysis the anharmonicities cannot be determined from measured energy positions of the vibrational substates, but only from intensity distributions. In fact, the intensity distribution is substantially influenced by anharmonicity. In contrast to this, the effects of anharmonicity on the energy positions of the vibrational substates are way too small to be observed due to the large linewidths in core-level spectroscopy. The observed intensities – and hence also the fitted anharmonicities – can, however, be influenced by effects beyond the present approach, which simplifies the full three-dimensional potential-energy surfaces to two decoupled Morse potentials.

The full complexity of the Auger transitions S $2p^{-1} \rightarrow \tilde{a}^1\Delta$ and S $2p^{-1} \rightarrow \tilde{b}^1\Sigma^+$, including excitations of the C−O and the C−S stretching vibrational modes, is displayed in Figure 3.15. This figure shows that the vibrational progressions visible in Figure 3.14 are mainly due to the Auger transitions $v' = (00) \rightarrow v = (0v_2)$. This is due to the fact that the transition $v'' = (00) \rightarrow v' = (00)$ in the photoelectron spectrum is the most intense one and that the population of the higher vibrational substates $v' = (v_1'0)$ in the photoelectron spectrum is distributed in the Auger decay to the final states $v = (v_1v_2)$ partially with $v_1' \neq v_1$. In particular, for the Auger transitions S $2p_{3/2,1/2}^{-1} \rightarrow \tilde{a}^1\Delta$, starting from $v' = (20)$, we see strong transitions to the vibrational levels $v = (1v_2)$, $v = (2v_2)$, and $v = (3v_2)$.

Table 3.10: Equilibrium distances R_e of the core-ionized and the metastable dicationic states derived from the fit analyses of the S $2p^{-1}$ photoelectron spectra and the subsequent Auger spectra of the OCS molecule. Changes of the equilibrium values of the normal coordinates ΔQ_e (relative to the ground state) are included for future conversions into real space using improved **L** matrices. Values for the ground state taken from the literature [111] as well as theoretical equilibrium distances for the dicationic states reported by Brites *et al.* [25] are included for comparison. For an assignment of the dicationic states A and B see text.

state	R_e, Å				ΔQ_e, Å·u$^{1/2}$	
	present work		[25]		present work	
	C−O	C−S	C−O	C−S	C−O	C−S
ground state	1.157	1.560				
S $2p^{-1}$	1.124(8)	1.581(9)			−0.087(1)	0
$\tilde{X}^3\Sigma^-$			1.11	1.79		
$\tilde{a}^1\Delta$	1.18(3)	1.74(2)	1.12	1.75	−0.027(4)	−0.758(5)
$\tilde{b}^1\Sigma^+$	1.17(2)	1.69(2)	1.13	1.71	−0.037(4)	−0.508(2)
$2^1\Delta$	1.15(4)	1.57(3)	1.24[a]	1.75[a]	−0.03(8)	0
$2^3\Pi$	1.158(12)	1.583(11)	1.16[a]	—[b]	−0.008(5)	−0.090(5)
$2^1\Pi$			1.22[a]	1.58[a]		
A	1.155(14)	1.603(13)			−0.023(5)	−0.159(6)
$2^1\Sigma^+$			1.24[a]	1.70[a]		
B	1.126(12)	1.581(11)			−0.08(1)	0
$^1\Sigma^+$	1.195(8)	1.535(9)			0.100(1)	0

[a] Derived from the position of the minimum of the potential-energy curve.
[b] No minimum in the potential-energy curve.

Auger transitions
S $2p^{-1} \rightarrow 2\pi^{-1}3\pi^{-1}$
S $2p^{-1} \rightarrow 9\sigma^{-1}3\pi^{-1}$
S $2p^{-1} \rightarrow 8\sigma^{-1}3\pi^{-1}$

Figure 3.16 shows the Auger spectrum in the kinetic-energy region from 131.4 eV to 137.5 eV as well as the corresponding fit results representing nine spin-orbit and molecular-field split Auger transitions: five transitions are to a dissociative state and four transitions to a metastable state.

To extract information on the potential-energy surfaces of the metastable dicationic states, we performed a Franck-Condon analysis. However, three facts rendered it impossible to determine the vibrational energies of all states exactly:

- ▷ for some of the Auger transitions, only the vibrational substate $v = (00)$ is clearly visible, while the higher vibrational substates are extremely weak;

Table 3.11: Vibrational energies $\hbar\omega$ and anharmonicities $x\hbar\omega$ of the core-ionized and the metastable dicationic states derived from the fit analyses of the S $2p^{-1}$ photoelectron spectra and the subsequent Auger spectra of the OCS molecule. Values for the ground state taken from the literature [111] as well as theoretical values for the dicationic states reported by Brites *et al.* [25] are included for comparison. For an assignment of the dicationic states A and B see text.

state	$\hbar\omega$, meV				$x\hbar\omega$, meV			
	present work		[25]		present work		[25]	
	C−O	C−S	C−O	C−S	C−O	C−S	C−O	C−S
ground state	257.13	107.77			1.4321	0.496		
S $2p^{-1}$	280.8(4)				1.3(1)			
$\tilde{X}^3\Sigma^-$		65(5)	284.1	63.0			3.4716	0.09
$\tilde{a}^1\Delta$	267.3[a]	70.0(4)	267.3	67.9	2.3559[a]	0	2.3559	0.35
$\tilde{b}^1\Sigma^+$	255.7[a]	73.0(9)	255.7	72.9	2.7278[a]	0	2.7278	0.47
$2^1\Delta$	266(20)				2[b]			
$2^3\Pi$	259(1)	100[b]			2[b]			
A	262(1)	93(3)			2[b]			
B	280(4)				2[b]			
$^1\Sigma^+$	238.0(5)				0.16(13)			

[a] Taken from the work of Brites *et al.* [25]; fixed in the fit analysis.
[b] Estimated, see text; fixed in the fit analysis.

- ▷ the transitions are on a non-linear background that is not exactly known;
- ▷ the Auger transitions to the states $2^3\Pi$ and A, see page 91, exhibit excitations of both the C−O and the C−S stretching vibrational modes.

To overcome these problems, we reduced the number of free parameters by relating the changes of the equilibrium values of the normal coordinates upon electronic transitions ΔQ_{e1} and the vibrational energies $\hbar\omega_1$, corresponding to the C−O stretching vibrational mode, with each other by using the approximation

$$R_e^2 \cdot \hbar\omega = const$$

for the various electronic states of a given molecule; this relation was originally established for diatomic molecules by Birge [117] and Mecke [118]. We tested this relation for the present case of the OCS molecule by applying it to the equilibrium distance R_e(C−O) and the vibrational energy $\hbar\omega_1$ of the ground state, the S $2p^{-1}$

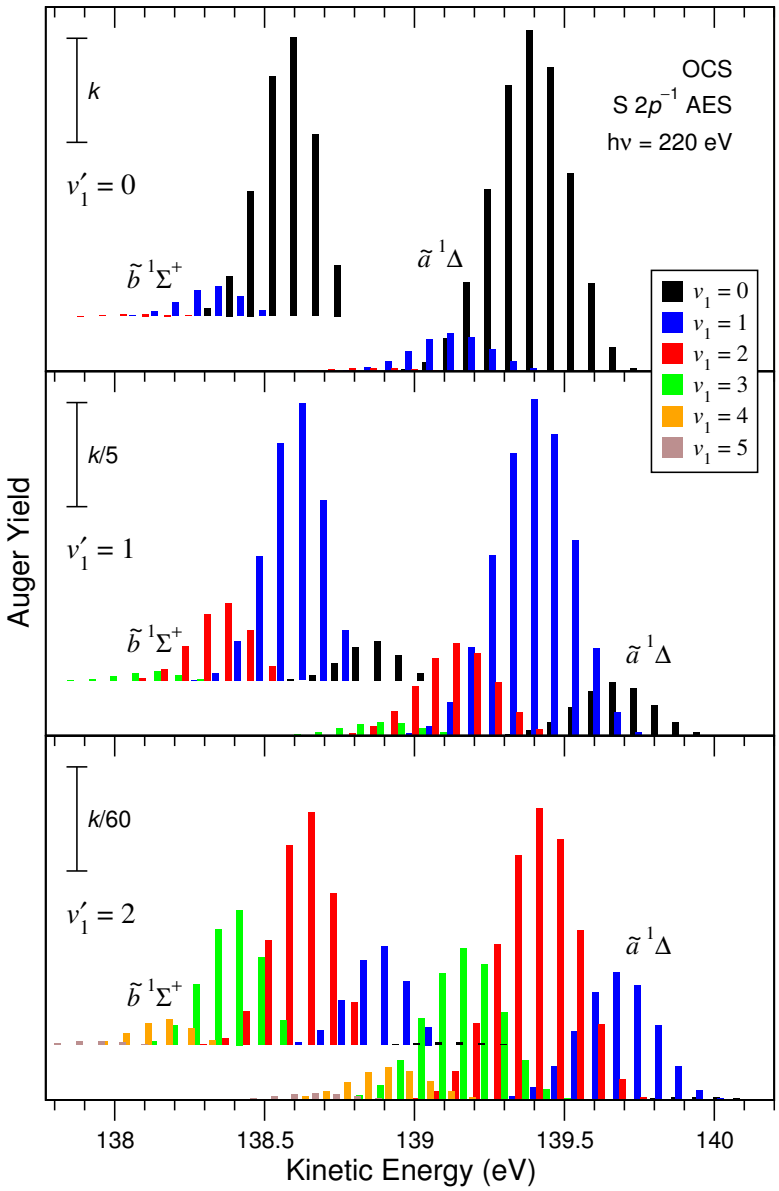

Figure 3.15: Detailed vibrational structure of the Auger transitions S $2p^{-1}_{3/2,1/2} \rightarrow \tilde{a}^1\Delta$ and S $2p^{-1}_{3/2,1/2} \rightarrow \tilde{b}^1\Sigma^+$ as obtained from the fit analysis. The different frames distinguish the vibrational levels v_1' in the S $2p^{-1}_{3/2,1/2}$ core-ionized state, and the different colors describe the vibrational levels v_1 in the dicationic states. The vertical bars of a given color give for the two Auger transitions the vibrational progressions for the C−S stretching vibrational mode, which belongs to fixed values of v_1' and v_1. The contributions from the vibrational lifetime interference are not included in the progressions. The intensity ratios for the frames with $v_1' = 0$, 1, and 2 are 60 : 12 : 1, respectively.

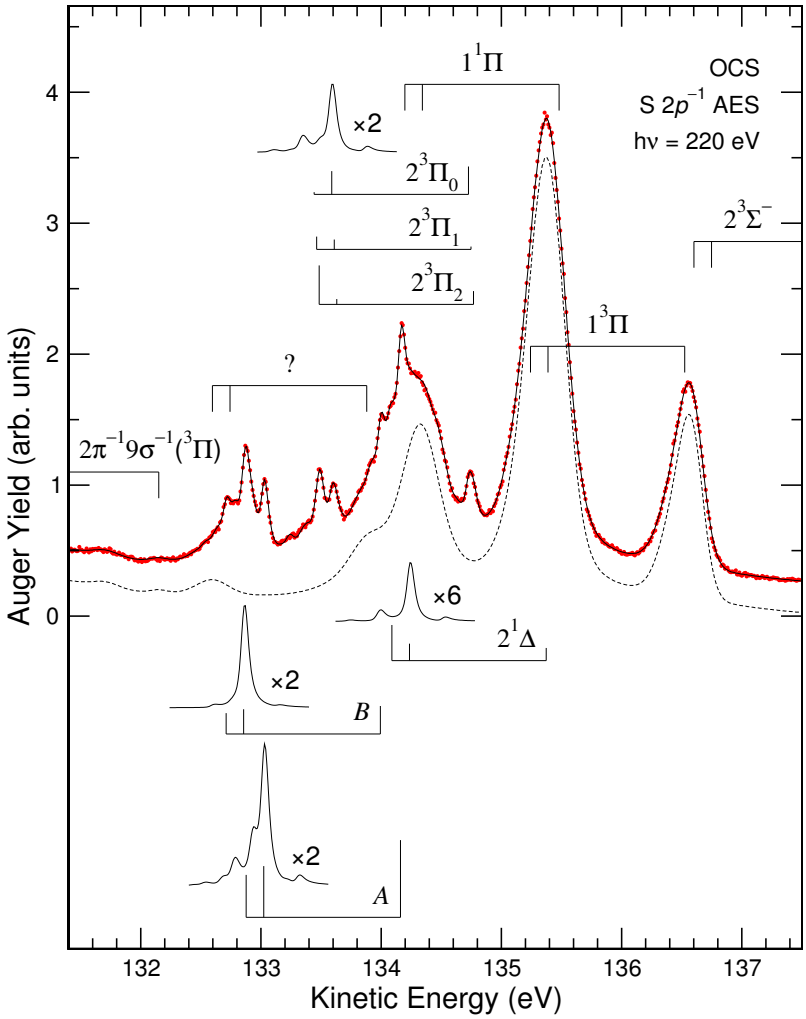

Figure 3.16: Auger spectrum of the OCS molecule subsequent to S $2p^{-1}$ photoionization measured at a photon energy of 220 eV in the kinetic-energy region from 131.4 eV to 137.5 eV. The down-directed vertical-bar diagrams give the approximate kinetic-energy positions of the peaks corresponding to the Auger transitions to the dissociative final states; these transitions are included in the background. For a description of the other bar diagrams and the lines see Figure 3.14; for an assignment of the dicationic states A and B see text.

core-ionized state, and the dicationic state $8\sigma^{-1}9\sigma^{-1}\left(^1\Sigma^+\right)$, see page 95, which all have the same value of the normal coordinate Q_{e2}. As a result, we found it to be valid within 5%. Therefore, we used these states to establish a relationship between ΔQ_{e1} and $\hbar\omega_1$ that was included in the fit analysis.

For Auger transitions S $2p^{-1} \rightarrow 2^3\Pi$ and S $2p^{-1} \rightarrow A$, which exhibit both the

Table 3.12: Comparison of the results derived from the calculations presented in Ref. [110], see Table 3.9, with the results reported by Brites *et al.* [25] and Minelli *et al.* [98] for the kinetic-energy region from 132.5 eV to 137.5 eV. Given are the kinetic energies ΔT_e^A presented relative to the S $2p^{-1} \rightarrow \tilde{X}^3\Sigma^-$ Auger transition as well as the branching ratios taken from the total S $2p^{-1}$ Auger intensities and presented relative to the S $2p^{-1} \rightarrow 1^3\Pi$ Auger transition.

state	label	ΔT_e^A, eV			branching ratio	
		[110]	[25]	[98]	[110]	[98]
$2^3\Sigma^-$	*d*	4.55	4.59	4.71	0.18	0.22
$1^3\Pi$	*e*	5.17	4.88	4.85	1	1
$2^1\Delta$	*f*	5.57	5.59	5.70	0.28	0.33
$1^1\Pi$	*g*	6.10	5.93	5.93	0.33	0.42
$2^1\Sigma^+$	*h*	6.26	6.36	6.46	0.17	0.25
$2^3\Pi$	*i*	6.67	6.64	6.45	0.31	0.30
$2^1\Pi$	*j*	7.41	7.30	7.28	0.37	0.45

C−O and the C−S stretching vibrational modes, the contributions from the C−S stretching vibrational mode turn out to be very small. In these cases, only vibrational substates with $v_2 = 1$ can be observed, but no higher ones. Therefore, for these Auger transitions the Franck-Condon analysis of the C−S stretching vibrational mode was simplified by applying the relation for the intensity ratio

$$\frac{I(v' = (00) \rightarrow v = (01))}{I(v' = (00) \rightarrow v = (00))} = \frac{\Delta Q_{e2}^2 \cdot \omega_2}{2\hbar},$$

where ω_2 is the vibrational frequency of the C−S stretching vibrational mode. Such a description is given by Cederbaum and Domcke [119]: it is based on the assumption of harmonic potentials for both the electronic initial and the electronic final states, which both have the same vibrational frequency. However, in the present cases, when the intensity ratios $\frac{I(v'=(00) \rightarrow v=(01))}{I(v'=(00) \rightarrow v=(00))}$ are small, the loss of accuracy due to this approximation is marginal, while the required computer time for a fit analysis is substantially reduced. As a result, an excellent fit result for this energy region was obtained.

To assign the observed transitions, we summarize in Table 3.12 the theoretical results from Ref. [110] for the kinetic-energy region from 132.5 eV to 137.5 eV as well as those from the works of Brites *et al.* [25] and Minelli *et al.* [98]. In this energy region, the agreement between experiment and theory is, however, not sufficient for an unequivocal assignment. This holds, in particular, for the region from 132.5 eV to 134.2 eV, where not even tentative assignments can be presented. The most striking difference between experiment and theory in this region is the fact

that eight Auger transitions are observed experimentally, while the calculations from Ref. [110] as well as the results of Minelli *et al.* [98] predict only seven transitions with rates significantly different from zero, namely the transitions to the dicationic states of the configurations $2\pi^{-1}3\pi^{-1}$ (the states $2^3\Sigma^-$, $2^1\Delta$, and $2^1\Sigma^+$), $9\sigma^{-1}3\pi^{-1}$ (the states $1^3\Pi$ and $1^1\Pi$), and $8\sigma^{-1}3\pi^{-1}$ (the states $2^3\Pi$ and $2^1\Pi$). These seven states are designated with letters from *d* to *j* in Tables 3.9 and 3.12 as well as in Figure 3.13. The sequence of the states obtained as a consequence of the calculations reported in Ref. [110], namely $2^3\Sigma^-$, $1^3\Pi$, $2^1\Delta$, $1^1\Pi$, $2^1\Sigma^+$, $2^3\Pi$, and $2^1\Pi$, with increasing relative kinetic energy ΔT_e^A, is in full agreement with the results of Brites *et al.* [25]. In the sequence of Minelli *et al.* [98], however, the order of the dicationic states $2^1\Sigma^+$ and $2^3\Pi$ is exchanged. The obvious contradiction between eight experimentally observed spin-orbit and molecular-field split Auger transitions and the seven theoretically predicted transitions requires an assignment beyond the above listed sequence of transitions.

In the first step, we identified the S $2p_{3/2}^{-1}$ components of the Auger transitions by employing the experimental S $2p_{3/2}^{-1}$ Auger spectrum obtained from the photoelectron-Auger-electron-coincidence work of Bolognesi *et al.* [96]. This spectrum displays four sharp peaks in the energy region from 131.5 eV to 137.5 eV. According to their fit analysis, these peaks are split from the transition S $2p_{3/2}^{-1} \rightarrow \tilde{X}^3\Sigma^-$ by 5.11 eV, 6.03 eV, 6.72 eV, and 7.28 eV; in the present kinetic-energy scale these energies correspond to 135.22 eV, 134.30 eV, 133.61 eV, and 133.05 eV, respectively.

The two peaks at 135.22 eV and 134.30 eV are in the energy region where the present high-resolution spectrum is dominated by broad peaks, which are formed as a consequence of dissociation. The peak at 135.22 eV is assigned by Bolognesi *et al.* [96], due to its high intensity, to the transition S $2p_{3/2}^{-1} \rightarrow 1^3\Pi$, which is in agreement with the calculations of Minelli *et al.* [98]. This assignment is also fully in line with the theoretical results of Ref. [110] and shows that this transition forms the low-kinetic-energy part of the peak at approximately 135.4 eV in the present spectrum, see Figure 3.16.

According to the calculations presented in Table 3.12, the transition S $2p_{3/2}^{-1} \rightarrow 2^3\Sigma^-$ should be at a kinetic energy that is by 0.15 to 0.62 eV higher than that of the transition S $2p_{3/2}^{-1} \rightarrow 1^3\Pi$, and it should be intense enough to be visible in the spectrum. Unfortunately, the S $2p_{3/2}^{-1}$ Auger spectrum of Bolognesi *et al.* [96] is too noisy in the respective energy region to allow an identification of the transition S $2p_{3/2}^{-1} \rightarrow 2^3\Sigma^-$. In the present spectrum we also do not find any structure that can be assigned clearly to this transition. Assuming that the calculated intensities for the transition S $2p_{3/2}^{-1} \rightarrow 2^3\Sigma^-$ are in the right order of magnitude, we had to conclude that this transition overlaps almost perfectly either with the transition S $2p_{1/2}^{-1} \rightarrow 1^1\Pi$ or the transition S $2p_{1/2}^{-1} \rightarrow 1^3\Pi$. From these two possible explanations we prefer an over-

lap with the latter transition at approximately 136.6 eV, since such an assignment explains the broad peak at approximately 137.9 eV included in the background in Figure 3.14. This assignment results in a splitting of 1.3 eV between the dicationic states $2^3\Sigma^-$ and $1^3\Pi$, which is by 0.68 to 1.15 eV larger than the theoretical splittings summarized in Table 3.12; we consider these numbers as an estimate for the accuracy of the theoretical relative-kinetic-energy values presented in this table.

The peak at 134.30 eV in the high-resolution Auger spectrum, presented in Figure 3.16, shows three S $2p_{3/2}^{-1}$ Auger transitions, namely a broad and intense peak that overlaps on its low-kinetic-energy tail with two molecular-field split weak and narrow peaks. In addition, a strong and narrow peak is observed in the present spectrum at 134.16 eV originating from the transition S $2p_{1/2}^{-1} \rightarrow A$, see page 92. In the discussed energy region all calculations predict the transitions S $2p_{3/2}^{-1} \rightarrow 2^1\Delta$ and S $2p_{3/2}^{-1} \rightarrow 1^1\Pi$, with the former having slightly lower intensities and slightly higher kinetic energies, see Table 3.12. The experimental intensity ratio for these two transitions is obviously not reproduced by the calculations, *i.e.* the theoretical results might not be highly reliable for the states $2^1\Delta$ and $1^1\Pi$, see below. Based on the calculated potential-energy surfaces of Brites *et al.* [25], we expect that the state $2^1\Delta$ is metastable, while the state $1^1\Pi$ is dissociative. As a consequence, we suggest that the broad peaks at higher kinetic energies are due to the transition S $2p_{3/2}^{-1} \rightarrow 1^1\Pi$, while the narrow peaks stem from the transition S $2p_{3/2}^{-1} \rightarrow 2^1\Delta$. Further below, we show that the potential-energy surfaces calculated for this energy region by Brites *et al.* [25] are not very accurate; see page 93 and, in particular, the potential-energy curve of the dicationic state $2^3\Pi$. All these deviations from experiment can be readily explained by avoided level crossings that have not been taken into account with sufficient accuracy. However, for the state $2^1\Delta$, an influence of an avoided level crossing can be excluded, since it is the only state with this symmetry in the considered energy region. We, consequently, assume the predicted metastability to be valid.

The intensities of the transitions to the dicationic state $2^1\Delta$, resulting from the present assignment, are much lower than the theoretical values discussed further below, see page 97. This might question the given assignment, in particular, since an alternative assignment for these transitions are Auger decays of S $2p^{-1}$ satellite states, which are expected to be very weak [13, 14]. However, such an assignment is even less convincing, since it would require the unlikely case that the following prerequisites are fulfilled:

- ▷ the dicationic states $1^1\Pi$ and $2^1\Delta$ are – contrary to expectation – both dissociative and overlap almost perfectly, since only this would explain the fact that only one state is observed;
- ▷ the S $2p^{-1}$ satellite state is stable with respect to dissociation and possesses a

state	T_e^A, eV
$\tilde{a}^1\Delta$	140.87(6)
$\tilde{b}^1\Sigma^+$	139.89(7)
$2^1\Delta$	135.36(9)
$2^3\Pi_2$	134.77(7)
$2^3\Pi_1$	134.75(7)
$2^3\Pi_0$	134.73(7)
A	134.16(7)
B	134.00(7)
$^1\Sigma^+$	131.00(7)

Table 3.13: Kinetic energies T_e^A of the Auger transitions to the metastable dicationic states derived from the fit analyses of the Auger spectra of the OCS molecule subsequent to S $2p^{-1}$ photoionization. Kinetic energies are given for the transitions through the S $2p_{1/2}^{-1}$ core-ionized state. For an assignment of the dicationic states A and B see text.

molecular-field splitting that deviates less than 20 meV from that of the S $2p^{-1}$ main component;

- ▷ the geometry of the S $2p^{-1}$ satellite state matches that of the dicationic state very well.

The peak at 133.61 eV in the S $2p_{3/2}^{-1}$ Auger spectrum reported by Bolognesi *et al.* [96] is much narrower than the other peaks. It can be related to the Auger transition S $2p_{3/2}^{-1} \rightarrow 2^3\Pi$ in the present spectrum. This assignment is based on an additional splitting of the transition as well as the intensity ratio of the subcomponents. It is also in full agreement with the assignment given in the work of Eland [8], where a line broadening is observed and where it is suggested that this is caused by a splitting of a triplet state. The assignment of the discussed transition to a state with $^3\Pi$ symmetry is supported by the fact that the centroids of the structures at approximately 134.8 eV, 133.6 eV, and 133.5 eV, which are all due to transitions to the same dicationic state, do not fully obey the spin-orbit and the molecular-field splittings of the S $2p^{-1}$ core-ionized state. Instead, they are shifted by several tens of meV. This finding suggests a spin-orbit splitting of the dicationic state $2^3\Pi$ into the components $2^3\Pi_2$, $2^3\Pi_1$, and $2^3\Pi_0$. Consequently, these three spectral features are fitted using three dicationic states with an equidistant splitting. For the resulting nine transitions we assumed the same vibrational progression but different Auger intensities. In this way a splitting of 22(1) meV between each two neighboring states is obtained, see Table 3.13, that is in full agreement with calculations of Hochlaf [104], which resulted in the state $2^3\Pi_2$ being the lowest one in energy and which gave a splitting of 21 meV between each two states. The vertical-bar diagrams indicating the Auger-transition rates in Figure 3.16 show a different behavior for the three components of the dicationic state $2^3\Pi$, see also Table 3.14. In particular, the intensity of the transition S $2p_{3/2,3/2}^{-1} \rightarrow 2^3\Pi_0$ vanishes almost completely. This can be readily understood by selection rules if one takes the

100% π-character of the S $2p^{-1}_{3/2,3/2}$ core-ionized state into account, *i.e.* the fact that it is a pure $^2\Pi_{3/2}$-state. For a transition to the state $2^3\Pi_0$, the outgoing Auger electron must have σ symmetry and it has to carry a magnetic total-angular-momentum Ω of $^3/_2$, which is forbidden on the basis of angular-momentum arguments. These observations clearly support the given assignment for the discussed structures.

In the energy region of the peak at 133.05 eV in the S $2p^{-1}_{3/2}$ Auger spectrum of Bolognesi *et al.* [96], the present high-resolution measurements reveal three different transitions. One of these transitions shows broad lines, and the corresponding final state is labeled by the sign "?" due to its rather unclear nature, see below. The remaining two transitions consist of narrow lines so that we relate them to the expected Auger transitions in this energy region, namely S $2p^{-1}_{3/2} \rightarrow 2^1\Sigma^+$ and S $2p^{-1}_{3/2} \rightarrow 2^1\Pi$. However, neither the present experimental results alone nor a combination with the available theoretical results allow to give a conclusive assignment for these two transitions, in particular, since this also depends on the assignment of the transition to the final state "?". In order to simplify the following discussion concerning these two transitions, we designate the final state of the Auger transition at higher kinetic energy as A, and the one at lower kinetic energy as B.

In the following, we discuss two possible assignments of the final state "?" and consider the consequences of these assignments. The first possible assignment is an Auger decay of a satellite excitation in the photoelectron spectrum. Such contributions in the Auger spectrum subsequent to $2p^{-1}$ photoionization have been observed before for the HCl molecule [13] and the H_2S molecule [14]. An assignment along these lines would be in agreement with the low intensity of the Auger transition, since such satellite lines are normally quite weak in the photoelectron spectrum. The dicationic state A can then be assigned to $2^1\Pi$, and the dicationic state B to $2^1\Sigma^+$, since the theoretical results give a higher Auger-transition rate for the transition to the state $2^1\Pi$ that is in agreement with the experiment, see Table 3.14. As a consequence, the kinetic energy of the transition S $2p^{-1} \rightarrow 2^1\Sigma^+$ is by 0.16 eV lower than that of the transition S $2p^{-1} \rightarrow 2^1\Pi$ and by 0.75 eV lower than that of the transition S $2p^{-1} \rightarrow 2^3\Pi$, see Table 3.13. Contrary to this, the theoretical results shown in Table 3.12 predict the kinetic energy of the transition S $2p^{-1} \rightarrow 2^1\Sigma^+$ by 0.94 to 1.15 eV higher than that of the transition S $2p^{-1} \rightarrow 2^1\Pi$ and by -0.01 to 0.41 eV higher than that of the transition S $2p^{-1} \rightarrow 2^3\Pi$. Therefore, the discussed assignment leads to a situation, where the experimental kinetic energy of the Auger electrons related to the dicationic state $2^1\Sigma^+$ is – on a relative energy scale – by more than 1 eV lower than predicted by all calculations. The same effect, but with opposite sign, is observed for the dicationic state $2^3\Sigma^-$, see page 89. Both states belong to the configuration $2\pi^{-1}3\pi^{-1}$, with $2^3\Sigma^-$ $\{2^1\Sigma^+\}$ being the one with the highest {lowest} kinetic energy. This might indicate that all calculations underestimate systematically the splitting between the dicationic states that belong to the

configuration $2\pi^{-1}3\pi^{-1}$.

The second possible assignment relates the final state "?" to higher vibrational substates of the Auger transition to the state B, however, with a considerable line broadening. Such a broadening effect for higher vibrational substates can be explained by a shallow potential minimum that can host only a small number of vibrational substates. In this case, the higher vibrational levels may have a shorter lifetime due to fast tunneling through the potential barrier or may even be continuum states; both situations would explain the broadening effect. Such an explanation is in line with the observed energy splitting of approximately 300 meV between the final state B and the state "?" as well as with the fact that the Auger transition to the state B consists of almost only one line, namely $v' = (00) \rightarrow v = (00)$. The suggested broadening effect has been observed before in the resonant Auger spectrum of the HBr molecule [120]. As a consequence of this assignment for the final state "?", we have to take into account the sum of the intensities of the Auger transitions to the states B and "?" for an assignment of the states A and B. However, the intensity ratio between the Auger transition to the state A and the Auger transition to the state B plus "?" is less pronounced than the ratio between the transitions to the states A and B alone so that the above intensity arguments for the tentative assignment, *i.e.* the Auger transitions S $2p_{3/2}^{-1} \rightarrow 2^1\Sigma^+$ and S $2p_{3/2}^{-1} \rightarrow 2^1\Pi$, no longer hold.

Thus, the assignment of the Auger transitions to the states A, B, and "?" is rather unclear at the moment. However, additional and more sophisticated calculations or further high-resolution photoelectron-Auger-electron-coincidence spectra, as described by Ulrich *et al.* [121], should allow to shed light on this part of the spectrum. In particular, coincidence spectra should allow to distinguish between the two possible assignments of the final state "?".

The Morse parameters extracted from the fit analysis of the transitions to the dicationic states $2^1\Delta$ and $2^3\Pi$ as well as to those labeled A and B are listed in Tables 3.10 and 3.11. A comparison of the equilibrium distances with the calculated results of Brites *et al.* [25] shows that the experimental values for $R_e(\mathrm{C{-}O})$ and $R_e(\mathrm{C{-}S})$ are on average by approximately 0.1 Å and 0.15 Å, respectively, smaller than the theoretical values. In addition, the dicationic state $2^3\Pi$ is clearly stable with respect to dissociation, although the calculations do not give a minimum along the internuclear distance $R(\mathrm{C{-}S})$. However, this potential-energy surface is strongly influenced by an avoided level crossing with the dicationic state $2\pi^{-1}9\sigma^{-1}\left(^3\Pi\right)$ considered below, and a slightly different potential-energy surface for the latter state can easily result in a metastable dicationic state $2^3\Pi$. This means that the accuracy of a given potential-energy surface depends on the accuracy of all other potential-energy surfaces of states with the same symmetry. In general, the agreement between an experimentally determined and a calculated potential-

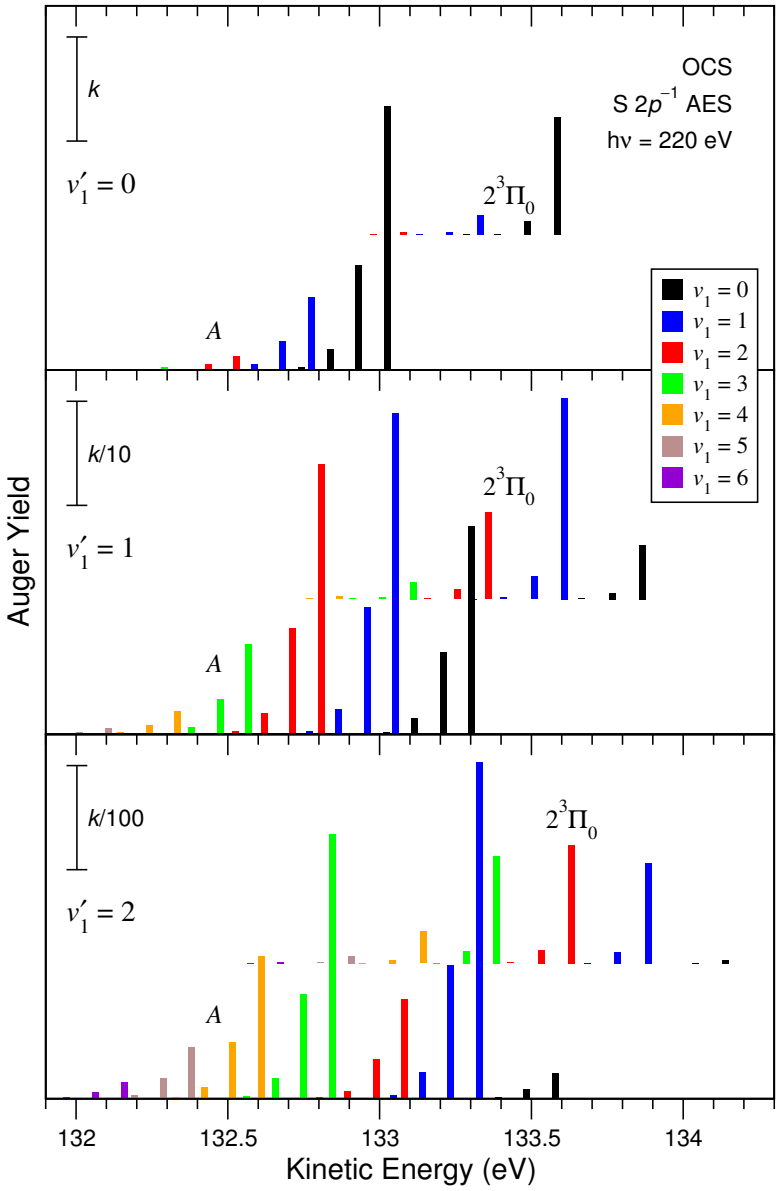

Figure 3.17: Detailed vibrational structure of the Auger transitions S $2p^{-1}_{3/2,1/2} \rightarrow 2^3\Pi_0$ and S $2p^{-1}_{3/2,1/2} \rightarrow A$ as obtained from the fit analysis. For an explanation to the frames and the colors see Figure 3.15. The intensity ratios for the frames with $v_1' = 0$, 1, and 2 are 100 : 10 : 1, respectively. For an assignment of the dicationic state A see text.

energy surface is not very accurate in this energy region. This low accuracy is probably due to the fact that the geometries of the molecule are not fully optimized. Instead, the curves along the internuclear distance R(C−S) are calculated with a

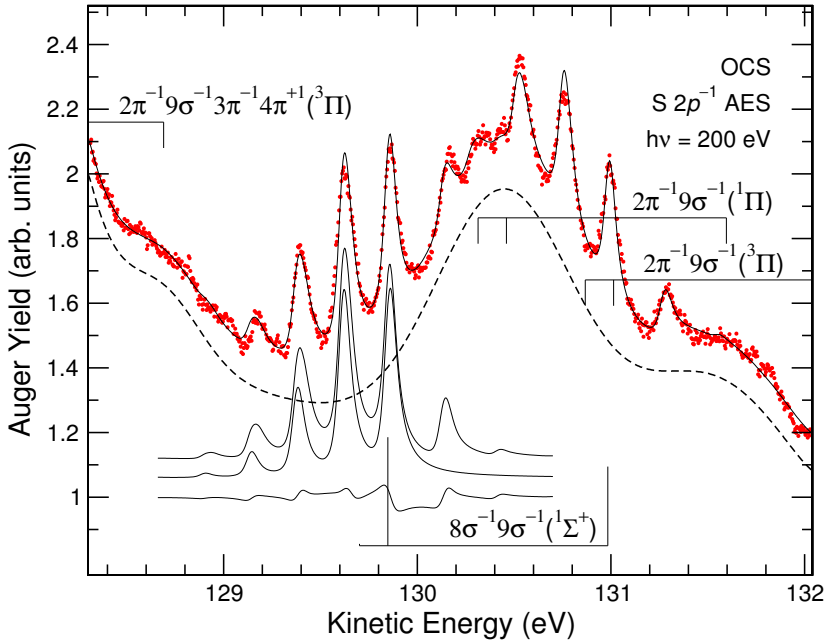

Figure 3.18: Auger spectrum of the OCS molecule subsequent to S $2p^{-1}$ photoionization measured at a photon energy of 200 eV in the kinetic-energy region from 128.3 eV to 132 eV. The middle subspectrum represents the contribution originating from the Auger decay of the vibrational level $v' = (00)$ of the core-ionized state alone. For a description of the bar diagrams and the other lines see Figures 3.14 and 3.16.

fixed value for the internuclear distance $R(\mathrm{C{-}O)}$ and *vice versa*.

In Figure 3.17, the detailed vibrational progressions including the excitations of the C−O and the C−S stretching vibrational modes of the transitions to the dicationic states $2^3\Pi_0$ and A are presented.

Auger transitions
S $2p^{-1}$ $\rightarrow$ $2\pi^{-1}9\sigma^{-1}$
S $2p^{-1}$ $\rightarrow$ $8\sigma^{-1}9\sigma^{-1}$
S $2p^{-1}$ $\rightarrow$ $2\pi^{-1}9\sigma^{-1}3\pi^{-1}4\pi^{+1}$

The Auger spectrum in the kinetic-energy region from 128.3 eV to 132 eV including the fit results is shown in Figure 3.18. From the experimental data points we clearly see a vibrational structure with a spacing of approximately 240 meV, which is typical for the C−O stretching vibrational mode.

From the fit analysis of this region only one dicationic state with a vibrational structure is found. In addition, the S $2p^{-1}_{3/2,3/2}$ component of the corresponding Auger transition is missing. An assignment of this transition is achieved by using the theoretical results from Ref. [110], see Table 3.9 and Figure 3.13. In the discussed kinetic-energy region, the intensity of the S $2p^{-1}_{3/2,3/2}$ component of the Auger transition to the state $8\sigma^{-1}9\sigma^{-1}\left(^1\Sigma^+\right)$ is calculated to be almost zero, while

the two other components have much higher intensities. Therefore, this transition can be assigned to S $2p^{-1} \rightarrow 8\sigma^{-1}9\sigma^{-1}\left(^1\Sigma^+\right)$.

The missing component S $2p^{-1}_{3/2,3/2} \rightarrow 8\sigma^{-1}9\sigma^{-1}\left(^1\Sigma^+\right)$ indicates clearly that the rate of the Auger transition $2p\pi^{-1} \rightarrow 8\sigma^{-1}9\sigma^{-1}\left(^1\Sigma^+\right)$ is very low, while the whole intensity is carried by the transition $2p\sigma^{-1} \rightarrow 8\sigma^{-1}9\sigma^{-1}\left(^1\Sigma^+\right)$. This allows one to estimate the $2p\sigma^{-1}$ contributions of the core-ionized states S $2p^{-1}_{1/2}$ and S $2p^{-1}_{3/2,1/2}$ as being 45% and 55%, respectively, by considering the intensity ratio of the corresponding Auger transitions. These values are in good agreement with the values of 43% and 57% for the core-ionized states S $2p^{-1}_{1/2}$ and S $2p^{-1}_{3/2,1/2}$ as calculated by Kosugi *et al.* [116]. To our knowledge this is the first direct experimental determination of the orientation of spin-orbit and molecular-field split $2p^{-1}$ core holes.

The background presented in Figure 3.18 consists of broad spin-orbit split spectral features at approximately 131.5 eV and 130.4 eV. We assign these features to the transition S $2p^{-1} \rightarrow 2\pi^{-1}9\sigma^{-1}\left(^1\Pi\right)$, since the ratio of their intensities and the intensities of the transition S $2p^{-1} \rightarrow 8\sigma^{-1}9\sigma^{-1}\left(^1\Sigma^+\right)$ agree well with the theoretical prediction in Ref. [110]. By taking into account that the calculated energies of the Auger transitions to the states $2\pi^{-1}9\sigma^{-1}3\pi^{-1}4\pi^{+1}\left(^3\Pi\right)$ and $9\sigma^{-2}\left(^1\Sigma^+\right)$ are clearly too high, see Figure 3.13, we assign the broad spectral feature at approximately 128.7 eV to the transition S $2p^{-1}_{1/2} \rightarrow 2\pi^{-1}9\sigma^{-1}3\pi^{-1}4\pi^{+1}\left(^3\Pi\right)$, although its intensity is underestimated by the theoretical results, see Table 3.9. In Figure 3.13, the S $2p^{-1}_{3/2}$ components of these Auger transitions exhibit high intensities between the lines at approximately 128 eV and 126.8 eV, which are assigned to the transition S $2p^{-1} \rightarrow 9\sigma^{-2}\left(^1\Sigma^+\right)$. The intense line corresponding to the transition S $2p^{-1}_{3/2} \rightarrow 2\pi^{-1}9\sigma^{-1}3\pi^{-1}4\pi^{+1}\left(^3\Pi\right)$ is also clearly visible in the S $2p^{-1}_{3/2}$ Auger spectrum presented by Bolognesi *et al.* [96].

The calculations presented in Ref. [110] as well as those of Minelli *et al.* [98] predict that the Auger transitions to the state $2\pi^{-1}9\sigma^{-1}\left(^3\Pi\right)$ have non-vanishing intensities. The kinetic energy of the transition S $2p^{-1} \rightarrow 2\pi^{-1}9\sigma^{-1}\left(^3\Pi\right)$ is calculated to be by 0.7 to 1.0 eV higher as compared to that of the transition S $2p^{-1} \rightarrow 8\sigma^{-1}9\sigma^{-1}\left(^1\Sigma^+\right)$, with the consequence that the S $2p^{-1}_{3/2}$ components are located at approximately 131 eV. This assignment is in agreement with double-charge-transfer measurements reported by Langford *et al.* [122], where a triplet state at approximately 9 eV above the ground state of OCS^{2+} is observed. Moreover, this assignment also explains the weak spectral feature at approximately 132.3 eV as the transition S $2p^{-1}_{1/2} \rightarrow 2\pi^{-1}9\sigma^{-1}\left(^3\Pi\right)$, see Figure 3.16.

The Morse parameters for the dicationic state $8\sigma^{-1}9\sigma^{-1}\left(^1\Sigma^+\right)$ derived from the Franck-Condon analysis are presented in Tables 3.10 and 3.11. However, since this state is more than 10 eV above the ground state of OCS^{2+}, calculations of the potential-energy surfaces are not available for comparison.

Table 3.14: Branching ratios of the Auger transitions to the metastable states derived from the fit analyses of the Auger spectra of the OCS molecule subsequent to S $2p^{-1}$ photoionization. Given are the mean values derived from the spectra measured at photon energies of 220 eV and 240 eV presented relative to the transition S $2p_{1/2}^{-1} \rightarrow \tilde{a}^1\Delta$. Theoretical branching ratios from Ref. [110] are included for comparison, see also Table 3.9. For an assignment of the dicationic states *A* and *B* see text.

state	present work				[110]			
	S $2p_{1/2}^{-1}$	S $2p_{3/2,1/2}^{-1}$	S $2p_{3/2,3/2}^{-1}$	$\sum$ S $2p^{-1}$	S $2p_{1/2}^{-1}$	S $2p_{3/2,1/2}^{-1}$	S $2p_{3/2,3/2}^{-1}$	$\sum$ S $2p^{-1}$
$\tilde{X}^3\Sigma^-$	0.646(5)	0.75(2)	1.02(3)	2.42(6)	0.958	0.731	1.689	3.378
$\tilde{a}^1\Delta$	1	0.99(1)	2.02(5)	4.01(6)	1	0.785	1.695	3.480
$\tilde{b}^1\Sigma^+$	0.626(1)	0.61(2)	1.19(4)	2.42(6)	0.537	0.421	0.914	1.872
$2^1\Delta$	0.012(7)	0.028(2)	0.0539(5)	0.09(1)	0.234	0.184	0.399	0.817
$2^3\Pi_2$	0.053(7)	0.025(1)	0.173(2)	0.25(1)				
$2^3\Pi_1$	0.04(2)	0.06(2)	0.0580(4)	0.15(4)				
$2^3\Pi_0$	0.11(2)	0.09(1)	0.005(4)	0.20(4)				
$\sum 2^3\Pi$	0.20(5)	0.18(3)	0.236(8)	0.61(9)	0.284	0.260	0.366	0.909
$2^1\Pi$					0.336	0.307	0.429	1.073
A	0.340(8)	0.226(5)	0.184(7)	0.75(2)				
$2^1\Sigma^+$					0.141	0.111	0.239	0.491
B	0.123(4)	0.108(4)	0.091(3)	0.32(1)				
$^1\Sigma^+$	0.128(1)	0.163(3)	0.003(2)	0.294(7)	0.058	0.075	0.005	0.138

Auger intensities Table 3.14 summarizes the present experimental intensities of the observed Auger transitions and the corresponding theoretical intensities reported in Ref. [110]. Given are the values for the various core-ionized states as well as the total Auger intensities to the individual metastable dicationic states. For the clearly assigned states the experimental and theoretical total Auger intensities agree on a qualitative level, with exception of the transitions to the dicationic state $2^1\Delta$. In this case, the theoretical Auger intensities are approximately by one order of magnitude too large.

The experimental Auger intensities vary significantly for the different core-ionized states. In particular, the intensities of the Auger transitions from the S $2p_{1/2}^{-1}$ and the S $2p_{3/2,1/2}^{-1}$ core-ionized states to the dicationic states $\tilde{X}^3\Sigma^-$, $\tilde{a}^1\Delta$, $\tilde{b}^1\Sigma^+$, $2^1\Delta$, and $2^3\Pi$ are lower than those starting from the S $2p_{3/2,3/2}^{-1}$ core-ionized state. Contrary to this, the S $2p_{3/2,3/2}^{-1}$ component of the Auger transition to the state $8\sigma^{-1}9\sigma^{-1}\left(^1\Sigma^+\right)$ vanishes almost completely. All these findings are qualitatively reproduced by the calculations and can be explained on the basis of the orientation of the core hole relative to the valence orbitals from which the electrons are missing [114, 115]. On a more detailed level, it turns out that the S $2p_{3/2,3/2}^{-1}$ components of the Auger transitions to the states $\tilde{X}^3\Sigma^-$, $\tilde{a}^1\Delta$, $\tilde{b}^1\Sigma^+$, and $2^3\Pi$ are overestimated by theory. Moreover, the theoretical intensities of the S $2p_{3/2,1/2}^{-1}$ components of

the Auger transitions to the states $\tilde{X}^3\Sigma^-$, $\tilde{a}^1\Delta$, and $\tilde{b}^1\Sigma^+$ are lower than those of the S $2p_{1/2}^{-1}$ components; in contrast to this, the experimental intensities are almost identical. All these observations are in line with the fact that the present theory overestimates the total $2p\pi^{-1}$ Auger-transition rates as compared to the total $2p\sigma^{-1}$ Auger-transition rates, see page 77.

Summary

From the Franck-Condon analyses of the Auger spectra of the OCS molecule performed in this work, vibrational structures for eight transitions could be separated and studied. These structures were assigned to the C−O or the C−S stretching vibrational modes. The assignment of the observed Auger transitions is partially based on the results of the new calculations for the Auger spectrum that take into account spin-orbit and molecular-field splitting as well as the various orientations of the three S $2p^{-1}$ core-ionized states [110]. From the Franck-Condon analysis of the photoelectron spectra we were able to derive for the first time the geometry of the S $2p^{-1}$ core-ionized states.

Summary and outlook

In the present work, the Auger spectra of the NO molecule subsequent to O $1s^{-1}$ and N $1s^{-1}$ photoionizations, the CO_2 molecule subsequent to C $1s^{-1}$ photoionization, and the OCS molecule subsequent to S $2p^{-1}$ photoionization are presented with high energy resolution together with corresponding photoelectron spectra. In all spectra vibrational progressions were observed. In contrast to the vibrational progressions in the photoelectron spectra, which are well known from literature, the vibrational progressions in the Auger spectra were clearly resolved in the experimental spectra for the first time.

For the open-shell molecule NO, the Franck-Condon analysis of the O $1s^{-1}$ and the N $1s^{-1}$ photoelectron spectra was performed by considering spin-orbit splitting of the $X^2\Pi$ ground state into the two components $^2\Pi_{1/2}$ and $^2\Pi_{3/2}$; the interaction of the spin moments of the $1s$ electron and the 2π electron from the open-shell orbital leading to a singlet-triplet splitting in the photoelectron spectra was taken into account as well. Lifetime broadenings of the various core-ionized states were derived from the fit analyses and they revealed different values for the $^1\Pi$ and the $^3\Pi$ components at both the O $1s$ and the N $1s$ ionization thresholds.

In the Auger spectra of the molecule, transitions to five metastable dicationic states were observed. Three of these states – $X^2\Sigma^+$, $A^2\Pi$, and $B^2\Sigma^+$ – are well known from the literature, while the other two states had also not been observed experimentally before and had not been predicted theoretically. Complementary calculations of the potential-energy curves of the dicationic states performed by Dr. Vladimir Špirko and Dr. Tereza Šedivcová-Uhlíková were used for the assignment of these states. The results of these calculations show excellent agreement with the experimental results for the states $X^2\Sigma^+$, $A^2\Pi$, and $B^2\Sigma^+$. Moreover, they predict seven metastable states, with five of them having equilibrium distances in the Franck-Condon region of the Auger process, *i.e.* the corresponding Auger transitions were expected to exhibit a vibrational structure that is in full agreement with the experimental observations. A comparison of the theoretical potential-energy curves with the experimental results allowed us to assign unambiguously the two hitherto unobserved metastable dicationic states to $C^2\Sigma^+$ and $c^4\Pi$. Thus, the present combined experimental and theoretical approach results in an improved understanding of the Auger spectra of the NO molecule subsequent to O $1s^{-1}$ and N $1s^{-1}$ photoionizations and provides experimentally tested potential-

energy curves for NO^{2+}.

In the Auger spectrum of the CO_2 molecule subsequent to C $1s^{-1}$ photoionization, seven transitions to metastable dicationic states were observed. Six transitions were assigned on the basis of the energy positions and equilibrium distances calculated by Hochlaf *et al.* [87] as well as on the assumption that Auger rates for transitions to triplet states are small. The seventh transition was assigned using the theoretical results of Feyer *et al.* [94]. The resulting assignment differs partly from previous results reported by Slattery *et al.* [9]. A comparison of the present Auger spectrum with the time-of-flight photoelectron-photoelectron-coincidence and the threshold-photoelectron-coincidence spectra [8, 9] reveals that the energy positions of the observed dicationic states disagree in part, *i.e.* different states are observed. The observed energy positions agree only qualitatively with the values calculated by Hochlaf *et al.* [87]; this fact indicates that the assignments might not be final. To arrive at more conclusive assignments, more sophisticated calculations and additional experimental studies are necessary.

For the OCS molecule, the Franck-Condon analysis was applied to the S $2p^{-1}$ photoelectron spectra by taking into account spin-orbit and molecular-field splittings of the core-ionized state. As a result, we obtained the geometry of the S $2p^{-1}$ core-ionized states.

In the Auger spectra of the OCS molecule subsequent to S $2p^{-1}$ photoionization, transitions to eight metastable dicationic states were observed. Auger transitions to seven of these states exhibit excitations of the C−O stretching vibrational mode and partially also of the C−S stretching vibrational mode. For an assignment of the dicationic states, calculations of Auger intensities taking into account the core-hole orientation of the different spin-orbit and molecular-field split S $2p^{-1}$ core-ionized states performed by Prof. Dr. Reinhold Fink were used. The results of these calculations in combination with previous results available in the literature and an experimentally observed splitting that clearly identified one dicationic state as $2^3\Pi$ allowed to assign six of the eight observed metastable dicationic states. The remaining two states were related to the states $2^1\Sigma^+$ and $2^1\Pi$. An assignment for transitions to dissociative states is also presented. In this way we obtained a clear picture of the potential-energy surfaces of the metastable dicationic states of the OCS molecule and compared the results with recent theoretical predictions of Brites *et al.* [25].

The Auger transition to the ground state $\tilde{X}^3\Sigma^-$ of OCS^{2+} exhibits only a weak vibrational structure that originates from the C−S stretching vibrational mode, and it turned out that a description within the Franck-Condon approximation is not possible. Up to now, the experimentally obtained potential-energy surfaces are reproduced well by theory for only two of the dicationic states, namely $\tilde{a}^1\Delta$ and $\tilde{b}^1\Sigma^+$, which both belong to the ground-state configuration $3\pi^{-2}$. For the transition

S $2p^{-1} \rightarrow 8\sigma^{-1}9\sigma^{-1}\left(^1\Sigma^+\right)$, the S $2p^{-1}_{3/2,3/2}$ component is missing. This peculiarity allowed an unambiguous assignment of this transition. Since this core hole has a pure $2p\pi^{-1}$ orientation, we were able to derive the core-hole orientation for the three spin-orbit and molecular-field split S $2p^{-1}$ core-ionized states; the obtained results are in good agreement with theoretical predictions.

Thus, a considerably improved understanding of the S $2p^{-1}$ Auger spectrum of the OCS molecule and the corresponding dicationic states has been achieved. For further improvement more accurate calculations of the potential-energy surfaces and of the vibrational structures are required. This holds, in particular, for the ground state $\tilde{X}^3\Sigma^-$ of OCS^{2+} as well as for all states that do not belong to the $3\pi^{-2}$ configuration. Further experimental studies are also required. For example, high-resolution photoelectron-Auger-electron-coincidence studies would allow to separate the overlapping Auger spectra that originate from the different spin-orbit and molecular-field split core holes. Such studies would, in particular, allow to separate the strongly overlapping Auger transitions to dissociative parts of the potential-energy surfaces and to derive their individual Auger intensities. They would also allow to identify possible contributions of Auger transitions originating from S $2p^{-1}$ satellite lines. It would also be interesting to record complementary high-resolution O $1s^{-1}$ and C $1s^{-1}$ Auger spectra, since in these cases partially different dicationic states are populated [95, 98]. In addition, the core-ionized states O $1s^{-1}$ and C $1s^{-1}$ of the OCS molecule have different geometries, *i.e.* different parts of the potential-energy surfaces of the dicationic states are probed by the two Auger processes.

In summary, for all the observed vibrational progressions the Franck-Condon analyses were performed. Assuming a Morse potential, the equilibrium distances, the vibrational energies, and the anharmonicities were obtained for all metastable dicationic states as well as core-ionized states. Moreover, the relative intensities of the various Auger transitions and the lifetime broadenings of the core-ionized states were derived. The information obtained on the potential-energy curves of the dicationic states was compared with the theoretical and experimental data available in the literature. For the dicationic states of the NO molecule, excellent agreement with the latest calculations was achieved. In contrast to this, the latest calculations of the triatomic molecules CO_2 and OCS do not allow an unambiguous assignment of the dicationic states. By taking into account the results for the dicationic states of other molecules [12, 13, 15], we conclude that state-of-the-art calculations can describe the dicationic states of diatomic molecules very well. However, the dicationic states of triatomic molecules are far from being fully understood theoretically.

Appendix A

Curve fitting

In this appendix, formulas for the curves fitted to the data of the photoelectron and Auger spectra are presented; moreover, all the physical quantities that can be derived from this analysis are summarized. In order to obtain the formulas for the fitting curves, some corrections to eqns. 1.55 and 1.58, which describe all lines corresponding to the transitions between stable or metastable electronic states in the photoelectron and Auger spectra, have to be introduced.

In an Auger spectrum, transitions to dissociative final states can be observed. A description of the corresponding spectral features based on assumed potential-energy curves is, in principle, possible. In this case, one has to apply the *Condon reflection principle*, as recently shown in Ref. [123]. However, an adoption of this approach leads to additional free parameters in the fit analysis; in the present cases, the number of free parameters becomes too large to obtain reliable fit result. Therefore, we describe the profiles of these Auger lines empirically, namely with a set of *Gaussian functions*, each of which is defined as

$$G_p(T) = A_p \cdot \frac{1}{\sqrt{2\pi \cdot \sigma_p^2}} \cdot e^{-\frac{(T-T_p)^2}{2\sigma_p^2}}. \tag{A.1}$$

The graph of this function is plotted in Figure A.1. The parameters T_p, A_p, and σ_p are responsible for the position, the intensity, and the width of the curve, respectively; the subscript p numbers the Gaussian functions used in the fit analysis. If we set the intensity A_p equal to 1, the function given by eqn. A.1 becomes normalized to unit area under the curve. The full width at half maximum of the Gaussian function amounts to $2 \cdot \sqrt{2 \cdot \ln 2} \cdot \sigma_p \approx 2.35 \cdot \sigma_p$.

The employed Gaussian functions do not have physical meaning with the exception of an Auger transition from the vibrational ground substate of the electronic intermediate state to a dissociative final state with a straight line as a potential-energy curve. In this case, the vibrational wave function of the intermediate state has a Gaussian shape, see Figure 1.1. For such a transition, the Condon reflection principle leads to a Gaussian lineshape, and the width of the Gaussian function can give information on the slope of the potential line of the dissociative state.

In addition, the PCI effect, which is discussed in Section 1.8, has to be included

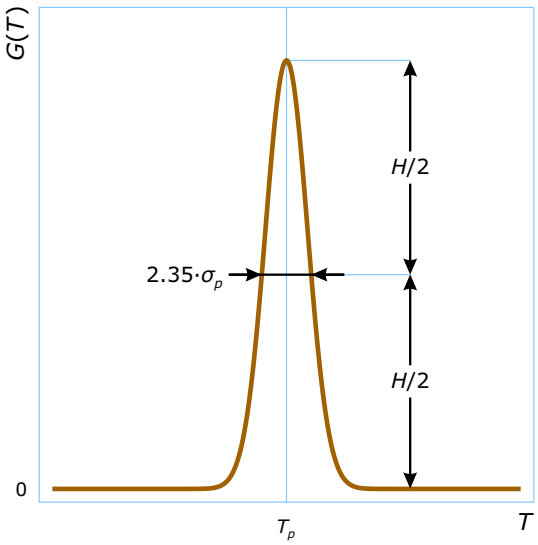

Figure A.1: Gaussian function used for a description of the lines corresponding to Auger transitions to dissociative final states.

in eqns. 1.55 and 1.58. For this purpose, we replace the normalized Lorentzian functions describing the direct terms, see eqn. 1.24, by the corresponding normalized PCI functions P^{ph}_{gif} and P^{A}_{gif}, see eqn. 1.59, and include the shift ΔT^P into the indirect terms of eqn. 1.58.

Finally, in order to describe the backgrounds of the photoelectron and Auger spectra, we include into eqns. 1.55 and 1.58 the quadratic functions $U^{ph}(T)$ and $U^{A}(T)$, respectively.

Thus, introducing all mentioned corrections, we obtain the curve fitted to a photoelectron spectrum as

$$I^{ph}_{g}(T) = U^{ph}(T) + \sum_{\varepsilon'}\sum_{v'} |\boldsymbol{D}_{\varepsilon''\varepsilon'}|^2 \cdot |F^{ph}_{v''v'}|^2 \cdot P^{ph}_{gif}(T), \tag{A.2}$$

and the curve fitted to an Auger spectrum as

$$I^{A}_{g}(T) = U^{A}(T) + \sum_{p} G_p(T) + I^{A1}_{g}(T) + I^{A2}_{g}(T), \tag{A.3}$$

where

$$I^{A1}_{g}(T) = \sum_{\varepsilon}\sum_{v}\sum_{\varepsilon'}\sum_{v'} |\boldsymbol{D}_{\varepsilon''\varepsilon'}|^2 \cdot |C_{\varepsilon'\varepsilon}|^2 \cdot |F^{ph}_{v''v'}|^2 \cdot |F^{A}_{v'v}|^2 \cdot P^{A}_{gif}(T),$$

and

$$I^{A2}_{g}(T) = \sum_{\varepsilon}\sum_{v}\sum_{\varepsilon'}\sum_{b'\neq v'} |\boldsymbol{D}_{\varepsilon''\varepsilon'}|^2 \cdot |C_{\varepsilon'\varepsilon}|^2 \cdot F^{ph}_{v''v'} \cdot F^{A}_{v'v} \cdot F^{ph}_{b'v''} \cdot F^{A}_{vb'}$$
$$\times \frac{\Gamma_{\varepsilon'}}{2\pi} \cdot \frac{\left(T-\Delta T^P-T^A_{\varepsilon' v' \varepsilon v}\right)\cdot\left(T-\Delta T^P-T^A_{\varepsilon' b' \varepsilon v}\right)+\left(\frac{\Gamma_{\varepsilon'}}{2}\right)^2}{\left(\left(T-\Delta T^P-T^A_{\varepsilon' v' \varepsilon v}\right)\cdot\left(T-\Delta T^P-T^A_{\varepsilon' b' \varepsilon v}\right)+\left(\frac{\Gamma_{\varepsilon'}}{2}\right)^2\right)^2+(E_{\varepsilon' v'}-E_{\varepsilon' b'})^2\cdot\left(\frac{\Gamma_{\varepsilon'}}{2}\right)^2}.$$

The sign of proportionality "$\propto$" presented in eqns. 1.55 and 1.58 is replaced in eqns. A.2 and A.3 by the sign of equality "$=$" because the corresponding constants of proportionality are included in the latter formulas into the intensity parameters $|\boldsymbol{D}_{\varepsilon''\varepsilon'}|^2$ and $|C_{\varepsilon'\varepsilon}|^2$. The inclusion of the constants of proportionality into these intensity parameters is reasonable because values of these parameters are not calculated in this study but are just derived from the fit analysis.

In order to simulate the experimental broadening of the photoelectron and Auger spectra, see Section 2.3, the functions defined by eqns. A.2 and A.3 are convoluted with a Gaussian function, see eqn. A.1 (with T_p set to 0, and A_p set to 1), of the width σ^{ph} or σ^{A}, respectively. The experimental broadening is defined as the full widths at half maximum of the corresponding Gaussian function. Thus, the experimental broadenings of the photoelectron and Auger spectra are equal to approximately $2.35 \cdot \sigma^{ph}$ and $2.35 \cdot \sigma^{A}$, respectively. The parameters σ^{ph} and σ^{A} are included in the fit analysis as free parameters; in this way the fit analysis allows to estimate the experimental broadening for both types of spectra.

The procedure of convolution as well as the fit analysis and the calculation of the Franck-Condon factor in the space of the normal coordinates is realized in the present study in the programming language `Fortran`. The calculation of the Franck-Condon factor, *i.e.* the overlap integrals in accordance with eqn. 1.38, is performed using an algorithm based on the work of Halmann and Laulicht [124] as well as Ory *et al.* [125], where the Born-Oppenheimer approximation and the Morse potential are assumed.

Finally, let us list the parameters whose values can be derived from fit analysis. From Section 1.5 we know values from which parameters can be derived by the Franck-Condon analysis of the photoelectron and Auger spectra. Since the Franck-Condon analysis is just a part of the total fit analysis, the set of quantities obtainable in the total fit analysis is larger. Therefore, the fit analysis of the photoelectron spectrum, with the fitting curve defined by eqn. A.2, allows one to obtain values of the following parameters:

- changes of the equilibrium values of the normal coordinates upon the photoionization process $\Delta Q_{e1\varepsilon''\varepsilon'}$, $\Delta Q_{e2\varepsilon''\varepsilon'}$, …, $\Delta Q_{eK\varepsilon''\varepsilon'}$, see eqn. 1.54;
- vibrational energies $\hbar\omega_{1\varepsilon'}$, $\hbar\omega_{2\varepsilon'}$, …, $\hbar\omega_{K\varepsilon'}$ and anharmonicities $x_{1\varepsilon'}\hbar\omega_{1\varepsilon'}$, $x_{2\varepsilon'}\hbar\omega_{2\varepsilon'}$, …, $x_{K\varepsilon'}\hbar\omega_{K\varepsilon'}$ of the electronic intermediate states, see eqn. 1.40;
- photoelectron kinetic energies T_{gi}^{ph}, see eqn. 1.17;
- relative intensities of the electronic transitions $|\boldsymbol{D}_{\varepsilon''\varepsilon'}|^2$, see eqn. 1.30;
- lifetime widths of the intermediate states $\Gamma_{\varepsilon'}$, see eqn. 1.25;
- parameters defining the quadratic function $U^{ph}(T)$ of the background;
- Gaussian parameter σ^{ph} defining the experimental broadening, see above.

When the fit analysis of the photoelectron spectrum is finished, the obtained values can be used as fixed parameters in the formula for the curve fitted to the Auger spectrum, see eqn. A.3. After this, the fit analysis of the Auger spectrum can be started. As a result, values of the following parameters can be derived:

- ▷ changes of the equilibrium values of the normal coordinates upon the Auger decay $\Delta Q_{e1\varepsilon'\varepsilon}$, $\Delta Q_{e2\varepsilon'\varepsilon}$, ..., $\Delta Q_{eK\varepsilon'\varepsilon}$, see eqn. 1.54;
- ▷ vibrational energies $\hbar\omega_{1\varepsilon}$, $\hbar\omega_{2\varepsilon}$, ..., $\hbar\omega_{K\varepsilon}$ and anharmonicities $x_{1\varepsilon}\hbar\omega_{1\varepsilon}$, $x_{2\varepsilon}\hbar\omega_{2\varepsilon}$, ..., $x_{K\varepsilon}\hbar\omega_{K\varepsilon}$ of the electronic final states, see eqn. 1.40;
- ▷ Auger-electron kinetic energies T^A_{if}, see eqn. 1.18;
- ▷ relative intensities of the electronic transitions $|C_{\varepsilon'\varepsilon}|^2$, see eqn. 1.32;
- ▷ parameters defining the quadratic function $U^A(T)$ of the background;
- ▷ parameters T_p, A_p, and σ_p defining the Gaussian functions $G_p(T)$ of the background, see eqn. A.1;
- ▷ Gaussian parameter σ^A defining the experimental broadening, see above.

The kinetic energies T^{ph}_{gi} and T^A_{if} derived from the fit analysis give, in accordance with eqns. 1.17 and 1.18 as well as eqn. 1.40, the positions of minima of the Morse-potential-energy curves of the electronic intermediate and the electronic final states relatively to that of the electronic ground state. Consequently, by the description of the Morse potentials, the parameters T^{ph}_{gi} and T^A_{if} can be considered as replacing the parameters $E_{e\varepsilon''}$, $E_{e\varepsilon'}$, and $E_{e\varepsilon}$ defining the locations of minima of the potential-energy curves in the absolute scale, see eqn. 1.39. Thus, the present fit analysis provides information on all parameters being necessary to describe the Morse potentials of stable and metastable electronic states involved in the photoionization process and the Auger decay, see page 23.

Appendix B

Calculation of L matrix

Here the calculations of the **L** matrices for the electronic ground state of the OCS molecule as well as the CO_2 and the NO molecules are presented. All calculations are made in accordance with Section 1.5.

Let us start from the calculation of the **L** matrix for the OCS molecule ($N = 3$). At first, we define the **P** matrix and the **S** matrix being matrices of the Cartesian displacement coordinates and the internal coordinates, respectively. The **P** matrix contains nine ($3N = 9$) coordinates, *i.e.*

$$\mathbf{P} = \begin{bmatrix} \Delta X_{\mathrm{O}}^{i} \\ \Delta X_{\mathrm{O}}^{j} \\ \Delta X_{\mathrm{O}}^{k} \\ \Delta X_{\mathrm{C}}^{i} \\ \Delta X_{\mathrm{C}}^{j} \\ \Delta X_{\mathrm{C}}^{k} \\ \Delta X_{\mathrm{S}}^{i} \\ \Delta X_{\mathrm{S}}^{j} \\ \Delta X_{\mathrm{S}}^{k} \end{bmatrix},$$

while the **S** matrix contains two bond stretching coordinates, namely $S_1 = R(\mathrm{C{-}O}) - R_e(\mathrm{C{-}O})$ and $S_2 = R(\mathrm{C{-}S}) - R_e(\mathrm{C{-}S})$, *i.e.*

$$\mathbf{S} = \begin{bmatrix} S_1 \\ S_2 \end{bmatrix}.$$

In fact, for a full description of the molecular geometry, we have to include into the **S** matrix a third internal coordinate, namely the bond angle bending coordinate $S_3 = \alpha(\angle\mathrm{OCS}) - \alpha_e(\angle\mathrm{OCS})$. However, this internal coordinate corresponds to the normal coordinate of the *bending vibrational mode* alone and can be neglected, since this mode is not visible in the spectrum.

The locations of the nuclei in the Cartesian coordinates are shown in Figure B.1. With the help of this figure and in accordance with eqns. 1.41 and 1.42 we can find the **B** matrix representing the relation between the Cartesian displacement coordinates and the internal coordinates. This matrix is

$$\mathbf{B} = \begin{bmatrix} -c_\alpha \cdot c_\beta & -s_\alpha & -c_\alpha \cdot s_\beta & c_\alpha \cdot c_\beta & s_\alpha & c_\alpha \cdot s_\beta & 0 & 0 & 0 \\ 0 & 0 & 0 & -c_\alpha \cdot c_\beta & -s_\alpha & -c_\alpha \cdot s_\beta & c_\alpha \cdot c_\beta & s_\alpha & c_\alpha \cdot s_\beta \end{bmatrix},$$

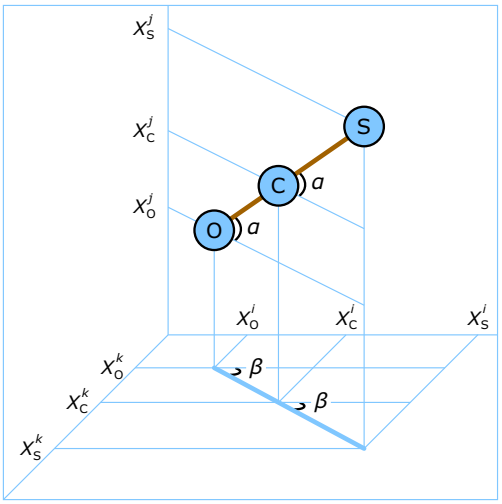

Figure B.1: OCS molecule in the Cartesian coordinates.

where c_α stands for $\cos\alpha$, c_β for $\cos\beta$, s_α for $\sin\alpha$, and s_β for $\sin\beta$.

The properties of the molecule are defined by the 9-by-9 ($3N$-by-$3N$) **M** matrix containing the atomic masses, see eqn. 1.43:

$$\mathbf{M} = \begin{bmatrix} M_O & 0 & 0 & 0 & 0 & 0 & 0 & 0 & 0 \\ 0 & M_O & 0 & 0 & 0 & 0 & 0 & 0 & 0 \\ 0 & 0 & M_O & 0 & 0 & 0 & 0 & 0 & 0 \\ 0 & 0 & 0 & M_C & 0 & 0 & 0 & 0 & 0 \\ 0 & 0 & 0 & 0 & M_C & 0 & 0 & 0 & 0 \\ 0 & 0 & 0 & 0 & 0 & M_C & 0 & 0 & 0 \\ 0 & 0 & 0 & 0 & 0 & 0 & M_S & 0 & 0 \\ 0 & 0 & 0 & 0 & 0 & 0 & 0 & M_S & 0 \\ 0 & 0 & 0 & 0 & 0 & 0 & 0 & 0 & M_S \end{bmatrix},$$

and with the 2-by-2 (K-by-K) **F** matrix containing the force constants of the bonds, see eqn. 1.44:

$$\mathbf{F} = \begin{bmatrix} F_{CO} & F_{OS} \\ F_{OS} & F_{CS} \end{bmatrix}.$$

Now, when the locations of the nuclei in the Cartesian displacement coordinates and in the internal coordinates are defined as well as the internal characteristics of the molecule are given, we can start to calculate the **L** matrix. Using eqn. 1.47, we find the **G** matrix as

$$\mathbf{G} = \begin{bmatrix} \frac{1}{M_O} + \frac{1}{M_C} & -\frac{1}{M_C} \\ -\frac{1}{M_C} & \frac{1}{M_C} + \frac{1}{M_S} \end{bmatrix}.$$

Then, in accordance with eqn. 1.51, the **H** matrix takes the form

$$\mathbf{H} = \begin{bmatrix} \frac{F_{CO}}{M_O} + \frac{F_{CO}-F_{OS}}{M_C} & \frac{F_{OS}}{M_O} + \frac{F_{OS}-F_{CS}}{M_C} \\ \frac{F_{OS}}{M_S} + \frac{F_{OS}-F_{CO}}{M_C} & \frac{F_{CS}}{M_S} + \frac{F_{CS}-F_{OS}}{M_C} \end{bmatrix}.$$

At this point, we proceed from designations to numbers. For this we substitute into the last expression the atomic masses: $M_O = 15.999$ u, $M_C = 12.011$ u, and $M_S = 32.066$ u, and the force constants [126]: $F_{CO} = 16.1036\ \frac{\text{mdyn}}{\text{Å}}$, $F_{OS} = 1.0304\ \frac{\text{mdyn}}{\text{Å}}$, and $F_{CS} = 7.4764\ \frac{\text{mdyn}}{\text{Å}}$.

Solving the secular equation 1.50 with the **H** matrix, we obtain two pairs of eigenvalues λ_k and eigenvectors $\mathbf{L}_k$. The first pair is

$$\left(\begin{array}{c} \lambda_1 = 2.5804\ \frac{\text{mdyn}}{\text{Å·u}} \\ \text{or} \\ \hbar\omega_1 = 259.3\ \text{meV} \end{array} \right) \text{and } \mathbf{L}_1 = \begin{bmatrix} 0.377 \\ -0.255 \end{bmatrix} \text{u}^{-1/2},$$

and the second one is

$$\left(\begin{array}{c} \lambda_2 = 0.4509\ \frac{\text{mdyn}}{\text{Å·u}} \\ \text{or} \\ \hbar\omega_2 = 108.4\ \text{meV} \end{array} \right) \text{and } \mathbf{L}_2 = \begin{bmatrix} -0.058 \\ -0.222 \end{bmatrix} \text{u}^{-1/2}.$$

The magnitudes λ_k and $\hbar\omega_k$ presented here are related to each other by using eqn. 1.53. The shown eigenvectors $\mathbf{L}_k$ are already normalized using normalization factors given by eqn. 1.52. Thus, uniting the eigenvectors $\mathbf{L}_1$ and $\mathbf{L}_2$, the following **L** matrix for the electronic ground state of the OCS molecule is constructed:

$$\mathbf{L} = \begin{bmatrix} 0.377 & -0.058 \\ -0.255 & -0.222 \end{bmatrix} \text{u}^{-1/2}. \tag{B.1}$$

As seen from the **L** matrix, for the first vibration, occurring at a frequency $\hbar\omega_1$, the C−O distance varies stronger than the C−S distance, while for the second vibration, occurring at a frequency $\hbar\omega_2$, the behavior is opposite. Due to these facts, the first normal vibration is called the *C−O stretching vibrational mode* and the second one the *C−S stretching vibrational mode*.

The presented calculation of the **L** matrix for the OCS molecule can be easily adapted to the CO_2 molecule, because CO_2 it is also a triatomic molecule. In spite of the fact that the bending vibrational mode contributes to the Auger spectrum of this molecule (the transition C $1s^{-1} \rightarrow a^1\Delta_g$), the bond angle bending internal coordinate $S_3 = \alpha(\angle\text{OCO}) - \alpha_e(\angle\text{OCO})$ can also be excluded from the **S** matrix, since – due to the mentioned symmetry reasons – the bending vibrational mode can be treated separately. For the mass M_3 we have to use M_O, for the force constant

F_{12} we use F_{OO}, and for the force constant F_{22} we use F_{CO}. These constants can be taken from the literature [127]: $F_{OO} = 1.3\ \frac{\text{mdyn}}{\text{Å}}$, and $F_{CO} = 15.5\ \frac{\text{mdyn}}{\text{Å}}$.

Substituting these values into the formula for the **H** matrix obtained for the OCS molecule (with M_O instead of M_S, F_{CO} instead of F_{CS}, and F_{OO} instead of F_{OS}), we find the following two pairs of eigenvalues and eigenvectors: the first one is

$$\begin{pmatrix} \lambda_1 = 1.0501\ \frac{\text{mdyn}}{\text{Å}\cdot\text{u}} \\ \text{or} \\ \hbar\omega_1 = 165.4\ \text{meV} \end{pmatrix} \text{and } \mathbf{L}_1 = \begin{bmatrix} 0.177 \\ 0.177 \end{bmatrix} \text{u}^{-1/2};$$

the second one is

$$\begin{pmatrix} \lambda_2 = 3.2521\ \frac{\text{mdyn}}{\text{Å}\cdot\text{u}} \\ \text{or} \\ \hbar\omega_2 = 291.1\ \text{meV} \end{pmatrix} \text{and } \mathbf{L}_2 = \begin{bmatrix} -0.338 \\ 0.338 \end{bmatrix} \text{u}^{-1/2}.$$

As a result, the **L** matrix for the CO_2 molecule can be formed from the eigenvectors $\mathbf{L}_1$ and $\mathbf{L}_2$ as

$$\mathbf{L} = \begin{bmatrix} 0.177 & -0.338 \\ 0.177 & 0.338 \end{bmatrix} \text{u}^{-1/2}.$$

The names of the considered vibrational modes of the CO_2 molecule once again originate from the characters of the normal vibrations, which are clearly seen from the **L** matrix. So, the vibration occurring at a frequency $\hbar\omega_1$ is called the *symmetric stretching vibrational mode*, while the vibration occurring at a frequency $\hbar\omega_2$ is called the *asymmetric stretching vibrational mode*.

The asymmetric stretching vibration is not seen in the spectra. Furthermore, it has a different symmetry than the symmetric stretching vibration, and from group theory we know that modes with different symmetries cannot interact. Because of these two reasons, the second column can be excluded from the **L** matrix. Thus, only one normal vibration and one normal coordinate remains under consideration. Since both bond stretching internal coordinates S_1 and S_2 expressed as $(R(\text{C}{-}\text{O}) - R_e(\text{C}{-}\text{O}))$ are indistinguishable at the remaining symmetric stretching vibration, we can consider only one of them and present the **L** matrix in the form of a scalar

$$\mathbf{L} = 0.177\ \text{u}^{-1/2}. \tag{B.2}$$

For completeness, let us present the **L** matrix for the simplest case of the diatomic NO molecule, which has only one vibrational mode. In this case, the **H** matrix is a number (an 1-by-1 matrix), which can be calculated as

$$\mathbf{H} = \frac{F_{NO}}{M_N} + \frac{F_{NO}}{M_O}.$$

After substitution of the atomic masses $M_N = 14.007$ u and $M_O = 15.999$ u and the force constant $F_{NO} = 15.9398 \frac{\text{mdyn}}{\text{Å}}$ (estimated from the data given in the literature [77]), the **L** matrix takes the form of a scalar

$$\mathbf{L} = 0.366 \text{ u}^{-1/2}, \tag{B.3}$$

while the vibrational frequency is equal to

$$\left(\begin{array}{c} \lambda = 2.1343 \frac{\text{mdyn}}{\text{Å·u}} \\ \text{or} \\ \hbar\omega = 235.8 \text{ meV} \end{array} \right).$$

As a matter of fact, eqns. B.2 and B.3 are particular cases of the equation

$$\mathbf{L} = \frac{1}{\sqrt{\mu}},$$

where μ is the *effective reduced mass* for the considered vibrational mode. In order to obtain eqn. B.2, we have to use the effective reduced mass

$$\mu = 2M_O,$$

while to obtain eqn. B.3,

$$\mu = \frac{M_N \cdot M_O}{M_N + M_O}.$$

Thus, we see that the **L** matrices for the CO_2 and the NO molecules do not depend on the force constants. This is due to the fact that the vibrations under considerations are the only ones with a given symmetry. In these cases, the force constants are required to calculate the vibrational frequencies, but not the **L** matrices.

Bibliography

[1] D. Mathur, Multiply charged molecules, *Phys. Rep.* **225**, 193 (1993).

[2] R. Thissen *et al.*, Doubly-charged ions in the planetary ionospheres: a review, *Phys. Chem. Chem. Phys.* **13**, 18264 (2011).

[3] Y. H. Jiang *et al.*, Few-photon multiple ionization of N_2 by extreme ultraviolet free-electron laser radiation, *Phys. Rev. Lett.* **102**, 123002 (2009).

[4] Y. H. Jiang *et al.*, Tracing direct and sequential two-photon double ionization of D_2 in femtosecond extreme-ultraviolet laser pulses, *Phys. Rev. A* **81**, 021401(R) (2010).

[5] H. Fukuzawa *et al.*, Ion momentum spectroscopy of N_2 and O_2 molecules irradiated by EUV free-electron laser pulses, *J. Phys. B: At. Mol. Opt. Phys.* **42**, 181001 (2009).

[6] A. Yamada *et al.*, Ion-ion coincidence studies on multiple ionizations of N_2 and O_2 molecules irradiated by extreme ultraviolet free-electron laser pulses, *J. Chem. Phys.* **132**, 204305 (2010).

[7] S. G. Cox *et al.*, High resolution spectroscopy and structure of molecular dications, *Phys. Chem. Chem. Phys.* **5**, 663 (2003).

[8] J. H. D. Eland, Complete double photoionisation spectra of small molecules from TOF-PEPECO measurements, *Chem. Phys.* **294**, 171 (2003).

[9] A. E. Slattery *et al.*, Spectroscopy and metastability of CO_2^{2+} molecular ions, *J. Chem. Phys.* **122**, 084317 (2005).

[10] O. Furuhashi *et al.*, Double charge transfer spectroscopy for N_2^{2+} and CO^{2+} at vibrational resolution, *Chem. Phys. Lett.* **337**, 97 (2001).

[11] O. Furuhashi *et al.*, Double charge transfer spectroscopy of NO^{2+} at vibrational resolution: Application of Franck-Condon analyses to a dicationic system, *Chem. Phys.* **295**, 185 (2003).

[12] R. Püttner *et al.*, Detailed analysis of the $3d^{-1} \rightarrow 4p\pi^{-2}$ normal Auger spectra in HBr and DBr, *Phys. Rev. A* **59**, 4438 (1999).

[13] R. Püttner *et al.*, Refinement in the analysis of molecular Auger electron spectra: The $2p^{-1} \rightarrow 3p\pi^{-2}$ spectra of HCl and DCl, *Phys. Rev. A* **65**, 042505 (2002).

[14] M. Poygin *et al.*, Detailed study of the S $2p^{-1} \rightarrow X^1A^1(2b_1^{-2})$ normal Auger spectra of H_2S, *Phys. Rev. A* **74**, 012711 (2006).

[15] R. Püttner *et al.*, Potential energy curves of the quasi-stable states of CO^{2+} determined using Auger spectroscopy, *Chem. Phys. Lett.* **445**, 6 (2007).

[16] R. Püttner *et al.*, State-dependent gerade/ungerade intensity ratios in the Auger spectrum of N_2, *J. Phys. B: At. Mol. Opt. Phys.* **41**, 141001 (2008).

[17] T. Matila *et al.*, Vibrational and electronic structure of the $3d^{-1} \rightarrow 4p(\pi, \sigma)^{-2}$ normal Auger spectrum of HBr studied by fully relativistic configuration-interaction calculations, *Phys. Rev. A* **61**, 032712 (2000).

[18] K. Ellingsen *et al.*, Fully relativistic configuration-interaction calculations on the vibrational and electronic structure of the $2p^{-1} \rightarrow 3p(\pi, \sigma)^{-2}$ normal Auger-electron spectrum of HCl, *Phys. Rev. A* **62**, 032502 (2000).

[19] B. Mondal *et al.*, Stability, spectroscopic constants, and dissociation of CO^{2+}: A theoretical study, *Int. J. Quantum Chem.* **109**, 469 (2009).

[20] T. Arion *et al.*, New insight into the Auger decay process in O_2: The coincidence perspective, *J. Electron Spectrosc. Relat. Phenom.* **185**, 234 (2012).

[21] L. Leman *et al.*, Carbonyl sulfide-mediated prebiotic formation of peptides, *Science* **306**, 283 (2004).

[22] A. S. Newton, Triple ionization in small molecules, *J. Chem. Phys.* **40**, 607 (1964).

[23] J. H. D. Eland *et al.*, Triple ionization spectra by coincidence measurements of double Auger decay: The case of OCS, *J. Chem. Phys.* **132**, 014311 (2010).

[24] J. Ridard *et al.*, Theoretical investigation of the dissociation of OCS^{2+} in the process $OCS(X^1\Sigma^+) + h\nu \rightarrow OCS^{2+} \rightarrow CO^+(X^2\Sigma^+) + S^+(^4S)$, *Chem. Phys.* **122**, 403 (1988).

[25] V. Brites *et al.*, OCS^{2+} dication spectroscopy and electronic states, *Chem. Phys.* **346**, 23 (2008).

[26] P. Atkins and R. Friedman, Molecular quantum mechanics, 4$^{\text{th}}$ edn., *Oxford University Press, New York, USA* (2005), p. 249.

[27] M. Born and R. Oppenheimer, Zur Quantentheorie der Molekeln, *Ann. Phys.* **389**, 457 (1927).

[28] P. M. Morse, Diatomic molecules according to the wave mechanics. II. Vibrational levels, *Phys. Rev.* **34**, 57 (1929).

[29] see Ref. [26], p. 359.

[30] L. Meitner, Über die Entstehung der β-Strahl-Spektren radioaktiver Substanzen, *Z. Phys. A* **9**, 131 (1922).

[31] P. Auger, Sur les rayons β^- secondaires produits dans un gaz par des rayons X, *CR Acad. Sci.* **177**, 169 (1923).

[32] R. Baková *et al.*, Computed lifetimes of metastable states of the NO^{2+} dication, *J. Chem. Phys.* **128**, 144301 (2008).

[33] T. A. Field and J. H. D. Eland, Lifetimes of metastable molecular doubly charged ions, *Chem. Phys. Lett.* **211**, 436 (1993).

[34] D. Mathur *et al.*, Long-lived, doubly charged diatomic and triatomic molecular ions, *J. Phys. B: At. Mol. Opt. Phys.* **28**, 3415 (1995).

[35] W. Heisenberg, Über den anschaulichen Inhalt der quantentheoretischen Kinematik und Mechanik, *Z. Phys. A* **43**, 172 (1927).

[36] see Ref. [26], p. 203.

[37] G Wentzel, Über strahlungslose Quantensprünge, *Z. Phys. A* **43**, 524 (1927).

[38] J. Franck and E. G. Dymond, Elementary processes of photochemical reactions, *Trans. Faraday Soc.* **21**, 536 (1926).

[39] E. U. Condon, A theory of intensity distribution in band systems, *Phys. Rev.* **28**, 1182 (1926).

[40] E. U. Condon, Nuclear motions associated with electron transitions in diatomic molecules, *Phys. Rev.* **32**, 858 (1928).

[41] see Ref. [26], p. 386.

[42] see Ref. [26], p. 365.

[43] N. B. Colthup *et al.*, Introduction to infrared and Raman spectroscopy, 3rd edn., *Academic Press, Boston, USA* (1990), p. 459.

[44] E. B. Wilson *et al.*, Molecular vibrations: The theory of infrared and Raman vibrational spectra, *Dover Publications Press, New York, USA* (1980).

[45] E. B. Wilson, A method of obtaining the expanded secular equation for the vibration frequencies of a molecule, *J. Chem. Phys.* **7**, 1047 (1939).

[46] E. B. Wilson, Some mathematical methods for the study of molecular vibrations, *J. Chem. Phys.* **9**, 76 (1941).

[47] see Ref. [26], p. 382.

[48] N. Correia *et al.*, Theory of band shape formation in Auger and autoionization spectra of molecules. Numerical applications and new high-resolution spectra for CO, *J. Chem. Phys.* **83**, 2035 (1985).

[49] G. J. Schulz, Resonances in electron impact on atoms, *Rev. Mod. Phys.* **45**, 378 (1973).

[50] VUV and soft X-ray photoionization, ed. by U. Becker and D. A. Shirley, *Plenum Press, New York, USA* (1996).

[51] T. D. Thomas *et al.*, Recoil excitation of vibrational structure in the carbon 1*s* photoelectron spectrum of CF_4, *J. Chem. Phys.* **128**, 144311 (2008).

[52] M. Yu. Kuchiev and S. A. Sheinermann, Resonant processes involving the production of three charged particles, *Sov. Phys. JETP* **63**, 986 (1986).

[53] G. B. Armen *et al.*, Quantum theory of post-collision interaction in inner-shell photoionization: Final-state interaction between two continuum electrons, *Phys. Rev. A* **36**, 5606 (1987).

[54] J. D. Jackson, Classical electrodynamics, 3rd edn., *Wiley Press, New York, USA* (1998), p. 661.

[55] H. Ohashi *et al.*, Outline of soft X-ray photochemistry beamline BL27SU of SPring-8, *Nucl. Instrum. Methods A* **467**, 529 (2001).

[56] T. Tanaka and H. Kitamura, Analysis of figure-8-undulator radiation, *J. Synchrotron Rad.* **3**, 47 (1996).

[57] M. Bässler *et al.*, Beam line I411 at MAX II - performance and first results, *Nucl. Instrum. Methods A* **469**, 382 (2001).

[58] G. LeBlanc *et al.*, Technical description of the MAX II undulators, The 5th European Particle Accelerator Conference, June 10 – 14, 1996, *Barcelona, Spain*.

[59] H. Ohashi *et al.*, Monochromator for a soft X-ray photochemistry beamline BL27SU of SPring-8, *Nucl. Instrum. Methods A* **467**, 533 (2001).

[60] S. Aksela *et al.*, Performance of the modified SX-700 plane grating monochromator at the Finnish beamline in MAX-lab, *Rev. Sci. Instrum.* **65**, 831 (1994).

[61] SPring-8 beamline handbook, 3rd edn., ed. by S. Goto *et al.*, *Japan Synchrotron Radiation Research Institute Press, Hyogo, Japan* (2004), p. 65.

[62] S. Svensson *et al.*, New end station for the study of gases, liquids, and solid films at the MAX laboratory, *Rev. Sci. Instrum.* **67**, 2149 (1996).

[63] N. Mårtensson *et al.*, A very high resolution electron spectrometer, *J. Electron Spectrosc. Relat. Phenom.* **70**, 117 (1994).

[64] V. L. Jacobs, Theory of atomic photoionization measurements, *J. Phys. B: At. Mol. Phys.* **5**, 2257 (1972).

[65] N. M. Kabachnik and I. P. Sazhina, Angular distribution and polarization of photoelectrons in the region of resonances, *J. Phys. B: At. Mol. Phys.* **9**, 1681 (1976).

[66] D. Cossart *et al.*, Optical emission spectrum of the NO^{2+} dication, *J. Mol. Spectrosc.* **125**, 413 (1987).

[67] D. Cossart and C. Cossart-Magos, Optical spectrum of the $^{15}NO^{2+}$ di-cation, *J. Mol. Spectrosc.* **147**, 471 (1991).

[68] L. G. M. Pettersson *et al.*, The X-ray excited Auger electron spectrum of NO and potential curves and photodissociation of the NO^{2+} ion, *J. Chem. Phys.* **96**, 4884 (1992).

[69] G. Dawber *et al.*, Threshold photoelectrons coincidence spectroscopy of doubly-charged ions of nitrogen, carbon monoxide, nitric oxide and oxygen, *J. Phys. B: At. Mol. Opt. Phys.* **27**, 2191 (1994).

[70] J. H. D. Eland *et al.*, Complete double photoionisation spectrum of NO, *Chem. Phys.* **290**, 27 (2003).

[71] D. L. Cooper, Ab initio investigation of low-lying $^2\Sigma^+$ and $^2\Pi$ states of NO^{2+}, *Chem. Phys. Lett.* **132**, 377 (1986).

[72] R. W. Wetmore and R. K. Boyd, A theoretical and experimental investigation of the dication of nitric oxide, *J. Phys. Chem.* **90**, 6091 (1986).

[73] L. G. M. Pettersson *et al.*, Theoretical potential curves for the $A^2\Pi$ and $X^2\Sigma^+$ states of NO^{2+} and an experimental search for the A–X transition, *Chem. Phys. Lett.* **191**, 279 (1992).

[74] R. Püttner *et al.*, Vibrationally resolved O 1*s* core-excitation spectra of CO and NO, *Phys. Rev. A* **59**, 3415 (1999).

[75] G. Remmers *et al.*, High-resolution inner-shell photoionization of NO, *Chem. Phys. Lett.* **214**, 241 (1993).

[76] R. Püttner *et al.*, Metastable states in NO^{2+} probed with Auger spectroscopy, *Phys. Chem. Chem. Phys.* **13**, 18436 (2011).

[77] G. Herzberg, Molecular spectra and molecular structure. I. Spectra of diatomic molecules, 2nd edn., *Van Nostrand Reinhold Press, New York, USA* (1950), p. 558.

[78] W. H. E. Schwarz and R. J. Buenker, Use of the Z+1-core analogy model: examples from the core-excitation spectra of CO_2 and N_2OS, *Chem. Phys.* **13**, 153 (1976).

[79] Gmelin handbook of inorganic chemistry. Fluorine, vol. **4**, 8th edn., ed. by D. Koschel *et al.*, *Springer-Verlag Press, Berlin, Germany* (1986), p. 297.

[80] see Ref. [77], p. 560.

[81] A. Rüdel *et al.*, Exchange interaction effects in NO core-level photoionization cross-sections, *New J. Phys.* **7**, 189 (2005).

[82] M. Hoshino *et al.*, Vibrationally resolved partial cross sections and asymmetry parameters for nitrogen K-shell photoionization of the NO molecule, *J. Phys. B: At. Mol. Opt. Phys.* **41**, 085105 (2008).

[83] H. Ågren, On the interpretation of molecular valence Auger spectra, *J. Chem. Phys.* **75**, 1267 (1981).

[84] D. W. Davis and D. A. Shirley, Splitting in nitrogen and oxygen 1*s* photoelectron peaks in two paramagnetic molecules: Spin density implications, *J. Chem. Phys.* **56**, 669 (1972).

[85] see Ref. [77], p. 106.

[86] W. E. Moddeman *et al.*, Determination of the K-LL Auger spectra of N_2, O_2, CO, NO, H_2O, and CO_2, *J. Chem. Phys.* **55**, 2317 (1971).

[87] M. Hochlaf *et al.*, Theoretical study of the electronic states of CO_2^{++}, *J. Phys. B: At. Mol. Opt. Phys.* **31**, 2163 (1998).

[88] V. Myrseth *et al.*, Adiabatic and vertical carbon 1*s* ionization energies in representative small molecules, *J. Electron Spectrosc. Relat. Phenom.* **122**, 57 (2002).

[89] G. Herzberg, Molecular spectra and molecular structure. II. Infrared and Raman spectra of polyatomic molecules, *Van Nostrand Reinhold Press, New York, USA* (1945), p. 398.

[90] see Ref. [89], p. 276.

[91] T. Hatamoto *et al.*, Vibrationally resolved C and O 1*s* photoelectron spectra of carbon dioxide, *J. Electron Spectrosc. Relat. Phenom.* **155**, 54 (2007).

[92] S. Sundin *et al.*, Influences from the C 1*s* shape resonance on the vibrational progression in the Auger decay of CO, *Phys. Rev. A* **58**, 2037 (1998).

[93] B. Bapat and V. Sharma, Bent dissociative states of CO_2^{2+}, *J. Phys. B: At. Mol. Opt. Phys.* **40**, 13 (2007).

[94] V. Feyer *et al.*, Effects of nuclear dynamics in the low-kinetic-energy Auger spectra of CO and CO_2, *J. Chem. Phys.* **123**, 224306 (2005).

[95] T. X. Carroll *et al.*, Carbon and oxygen KLL and sulfur LMM Auger spectra of OCS, *J. Electron Spectrosc. Relat. Phenom.* **51**, 471 (1990).

[96] P. Bolognesi *et al.*, The OCS S L_3MM Auger spectrum and angular distributions studied by photoelectron-Auger electron coincidence experiments, *J. Phys. Chem. A* **113**, 15136 (2009).

[97] T. Kaneyasu *et al.*, Stability and fragmentation of OCS^{2+} studied by using Auger-electron-ion coincidence measurement, *J. Korean Phys. Soc.* **54**, 371 (2009).

[98] D. Minelli *et al.*, Ab initio simulation of molecular Auger spectra: Nuclear dynamics effects in the spectra of carbonyl sulfide, *J. Chem. Phys.* **107**, 6070 (1997).

[99] S. Masuda *et al.*, Spin-forbidden shake-up states of OCS molecule studied by resonant photoelectron spectroscopy, *J. Electron Spectrosc. Relat. Phenom.* **137**, 351 (2004).

[100] I. Nenner *et al.*, Molecular spectroscopy and dynamics of core and valence excited states by electron scattering and synchrotron radiation, *J. Mol. Struct.* **173**, 269 (1988).

[101] R. F. Fink *et al.*, Specific production of very long-lived core-excited sulfur atoms by $2p^{-1}\sigma^*$ excitation of the OCS molecule followed by ultrafast dissociation, *J. Phys. B: At. Mol. Opt. Phys.* **39**, L269 (2006).

[102] M. Magnuson *et al.*, Competition between decay and dissociation of core-excited carbonyl sulfide studied by X-ray scattering, *Phys. Rev. A* **59**, 4281 (1999).

[103] T. R. Walsh *et al.*, *Ab initio* calculations of normal and resonant X-ray emission spectra for the OCS molecule, *J. Phys. B: At. Mol. Opt. Phys.* **29**, 207 (1996).

[104] M. Hochlaf, private communication (2010).

[105] M. Coville and T. D. Thomas, Sulfur 2*p* ionization energies of H_2S, OCS, SO_2, and CS_2, *J. Electron Spectrosc. Relat. Phenom.* **71**, 21 (1995).

[106] H. Siegbahn *et al.*, The Auger electron spectrum of water vapour, *Chem. Phys. Lett.* **35**, 330 (1975).

[107] H. Ågren *et al.*, SCF and limited CI calculations for assignment of the Auger spectrum and of the satellites in the soft X-ray spectrum of H_2O, *Chem. Phys. Lett.* **35**, 336 (1975).

[108] R. Fink, Theoretical autoionization spectra of $1s \rightarrow \pi^*$ excited N_2 and N_2O, *J. Electron Spectrosc. Relat. Phenom.* **76**, 295 (1995).

[109] R. F. Fink *et al.*, Spin-orbit interaction and molecular-field effects in the $L_{2,3}VV$ Auger-electron spectra of HCl, *Phys. Rev. A* **58**, 1988 (1998).

[110] V. Sekushin *et al.*, A comprehensive study of the vibrationally resolved S $2p^{-1}$ Auger electron spectrum of carbonyl sulfide, *J. Chem. Phys.* **137**, 044310 (2012).

[111] Gmelin Handbuch der anorganischen Chemie. Kohlenstoff, vol. **D5**, 8th edn., ed. by V. Haase *et al.*, *Springer-Verlag Press, Berlin, Germany* (1977), p. 32.

[112] M. R. F. Siggel *et al.*, High resolution photoelectron spectroscopy of sulfur 2*p* electrons in H_2S, SO_2, CS_2, and OCS, *J. Chem. Phys.* **105**, 9035 (1996).

[113] E. Kukk *et al.*, Angular distribution of molecular-field- and spin-orbit-split sulfur 2*p* photoemission in OCS: A sensitive probe of the molecular environment, *J. Phys. B: At. Mol. Opt. Phys.* **33**, L51 (2000).

[114] S. Svensson *et al.*, Observation of an anomalous decay ratio between the molecular field split levels in the S 2*p* core photoelectron and LVV Auger spectrum of H_2S, *Phys. Rev. Lett.* **72**, 3021 (1994).

[115] A. Machado Bueno *et al.*, Influence of chemical bonds on the lifetime of the molecular-field-split $2p$ levels in H_2S, *Phys. Rev. A* **67**, 022714 (2003).

[116] N. Kosugi and T. Ishida, Molecular field and spin-orbit splittings in the $2p$ ionization of second-row elements: A Breit-Pauli approximation applied to OCS, SO_2, and PF_3, *Chem. Phys. Lett.* **329**, 138 (2000).

[117] R. T. Birge, *Phys. Rev.* **25**, 240 (1925).

[118] R. Mecke, Zum Aufbau der Bandenspektra, *Z. Phys. A* **32**, 823 (1925).

[119] L. S. Cederbaum and W. Domcke, A many-body approach to the vibrational structure in molecular electronic spectra. I. Theory, *J. Chem. Phys.* **64**, 603 (1976).

[120] R. Püttner *et al.*, Strong nonmonopole shake transitions in the Br $3d^{-1}np\pi$ (n = 6 – 9) resonant Auger spectra of HBr, *Phys. Rev. A* **77**, 032705 (2008).

[121] V. Ulrich *et al.*, Photoelectron-Auger electron coincidence spectroscopy of free molecules: New experiments, *J. Electron Spectrosc. Relat. Phenom.* **183**, 70 (2011).

[122] M. L. Langford *et al.*, Triplet-state energy levels of CO_2^{2+}, COS^{2+} and CS_2^{2+}, *Chem. Phys.* **149**, 445 (1991).

[123] R. Püttner *et al.*, Probing dissociative molecular dications by mapping vibrational wave functions, *Phys. Rev. A* **83**, 043404 (2011).

[124] M. Halmann and I. Laulicht, Isotope effects on vibrational transition probabilities. II. Electronic transitions of isotopic nitrogen, nitric oxide, and oxygen molecules, *J. Chem. Phys.* **43**, 438 (1965).

[125] H. A. Ory *et al.*, Franck-Condon factors for the NO beta and gamma band systems, *Astrophys. J.* **139**, 346 (1964).

[126] see Ref. [111], p. 41.

[127] see Ref. [89], p. 187.

Publications

[1] R. Püttner, V. Sekushin, G. Kaindl, X.-J. Liu, H. Fukuzawa, K. Ueda, T. Tanaka, M. Hoshino, and H. Tanaka, A vibrationally resolved C $1s^{-1}$ Auger spectrum of CO_2, *J. Phys. B: At. Mol. Opt. Phys.* **41**, 045103 (2008).

[2] R. Püttner, T. Arion, M. Förstel, T. Lischke, M. Mucke, V. Sekushin, G. Kaindl, A. M. Bradshaw, and U. Hergenhahn, Probing dissociative molecular dications by mapping vibrational wave functions, *Phys. Rev. A* **83**, 043404 (2011).

[3] R. Püttner, V. Sekushin, H. Fukuzawa, T. Uhlíková, V. Špirko, T. Asahina, N. Kuze, H. Kato, M. Hoshino, H. Tanaka, T. D. Thomas, E. Kukk, Y. Tamenori, G. Kaindl, and K. Ueda, Metastable states in NO^{2+} probed with Auger spectroscopy, *Phys. Chem. Chem. Phys.* **13**, 18436 (2011).

[4] L. Argenti, T. D. Thomas, E. Plésiat, X.-J. Liu, C. Miron, T. Lischke, G. Prümper, K. Sakai, T. Ouchi, R. Püttner, V. Sekushin, T. Tanaka, M. Hoshino, H. Tanaka, P. Decleva, K. Ueda, and F Martin, Double-slit experiment with a polyatomic molecule: vibrationally resolved C 1*s* photoelectron spectra of acetylene, *New J. Phys.* **14**, 033012 (2012).

[5] V. Sekushin, R. Püttner, R. F. Fink, M. Martins, Y. H. Jiang, H. Aksela, S. Aksela, and G. Kaindl, A comprehensive study of the vibrationally resolved S $2p^{-1}$ Auger electron spectrum of carbonyl sulfide, *J. Chem. Phys.* **137**, 044310 (2012).

The present thesis is mainly based on Refs. [1], [3], and [5], to which the author contributed in particular by data analysis, curve fitting, and theoretical analysis as well as in the writing of the manuscripts. For Refs. [2] and [4], the author contributed mainly in obtaining the experimental results.

Acknowledgements

This work would not be possible without continuous and competent direction of my research supervisor Dr. R. Püttner, whose advices and remarks were very helpful in writing of this thesis. His willingness and ability to explain all questions of my interest steadily favored the growth of my knowledge during long time.

I also would like to extend my gratitude to Prof. Dr. Dr. *h.c.* G. Kaindl and Dr. N. Schwentner for the opportunity to work in their study groups; particular thanks to Mr. Kaindl for his revision of the manuscript. Special appreciation goes to Dr. V. Špirko, Dr. T. Šedivcová-Uhlíková, and Prof. Dr. R. Fink for performed calculations for our joint articles underlying this thesis.

I gratefully acknowledge Prof. Dr. A. Vinogradov and V. Bakulev from Saint Petersburg State University for their attention to my person, for the attempt to write the doctoral thesis in Germany, and for their belief in my power. In addition, I want to thank Alexander Gottberg and Alexander Helmke from AG Kaindl, who met me in Berlin and helped me to feel at home here in the beginning.

Finally, thanks to my friends: Nikita Malafeev, Natalia Horn, Anton Tikhonov, Kira Popova, Evgeny and Svetlana Pavlov, Anton and Julia Bender, and Vira Barylska, for their support and a wonderful, although rare, rest. Without you, my life and work in Germany would be tedious and perhaps impossible. Particular thanks to my father and my mother for their love: I hope, two doctors more will be soon in our family.

Curriculum vitae

For reasons of data protection, the Curriculum vitae is not published in the online version.